

Structural Analysis of Nanoparticles by Small Angle X-ray Scattering

Dissertation

Zur Erlangung des akademischen Grades eines
Doktors der Naturwissenschaften (Dr. rer. Nat.)
in Fach Chemie der Fakultät für Biologie, Chemie und Geowissenschaften
der Universität Bayreuth

vorgelegt von

Christophe N. Rochette, M. Sc.
geboren in Bordeaux, Frankreich

Bayreuth, Donnerstag den 17. November 2011

Die vorliegende Arbeit wurde in der Zeit von November 2005 bis November 2009 am Lehrstuhl für Physikalische Chemie I der Universität Bayreuth unter Betreuung von Herrn Prof. Dr. Matthias Ballauff angefertigt.

Vollständiger Abdruck der von der Fakultät für Biologie, Chemie und Geowissenschaften der Universität Bayreuth genehmigten Dissertation zur Erlangung des akademischen Grades eines Doktors der Naturwissenschaften (Dr. rer. nat.).

Dissertation eingereicht am:	17.11.2011
Zulassung durch die Prüfungskommission:	15.12.2011
Wissenschaftliches Kolloquium:	14.05.2012

Amtierender Dekan:
Prof. Dr. Beate Lohnert

Prüfungsausschuss:
Prof. Dr. M. Ballauff (Erstgutachter)
Prof. Dr. St. Förster (Zweitgutachter)
Prof. Dr. A. Müller (Vorsitz)
Prof. Dr. B. Weber

This work is dedicated to Jean de Bertier, my Grandfather.

Contents

1	Introduction	8
2	Theory of SAXS	10
2.1	Basis of SAXS theory	10
2.2	Scattering function of monodisperse particles	12
2.2.1	Spherical particles	12
2.2.2	Disk-like particles	12
2.2.3	Local fluctuations	13
2.3	Polydispersity	13
2.4	Interparticle interactions	14
2.4.1	Aggregation	14
2.4.2	Polymer Reference Interaction Site Model - PRISM	15
2.5	Contrast Variation	15
3	Generalities	17
3.1	Calcification	17
3.2	Polybutadiene	21
3.3	Polyethylene	22
4	Study of the early stage of calcification	26
4.1	Investigation of the early stage	26
4.1.1	Materials	27
4.1.2	Experimental	28
4.2	Results and discussion	29
4.2.1	Nucleation	29
4.2.2	Structural effect of Fetuin-A onto the CPPs	33
5	Polybutadiene	41
5.1	Experimental	41
5.2	Theoretical modeling	42
5.3	Results and Discussions	43
5.3.1	Cryo-TEM	43

5.3.2	SAXS	44
5.4	Conclusion	46
6	Polyethylene	48
6.1	Experimental	48
6.2	Results and discussion	49
6.2.1	Cryo-TEM	49
6.2.2	SAXS	50
6.3	Variation of annealing temperature	53
7	Experimental	58
7.1	SAXS	58
7.1.1	Kratky-Compact-Camera	58
7.1.2	ID02	58
7.2	Dynamic Light Scattering	59
7.3	Densitometry	59
8	Summary	61
8.1	Calcification	61
8.2	Polybutadiene	62
8.3	Polyethylene	63
9	Zusammenfassung	64
9.1	Calcifizierung	64
9.2	Polybutadien	65
9.3	Polyethylen	66
	Appendices	67
A	Theory of SAXS	68
A.1	Effect of polydispersity	68
A.2	C ⁺⁺ programs	69
A.2.1	form factor of homogenous spherical polydisperse particles	69
A.2.2	structure factor of the aggregation of spherical particles	71
A.3	Modified hamburger model	72
B	Additional experimental information	76
B.1	TEM pictures of calcium phosphate complexes	76
B.1.1	Without addition of Fetuin-A	77
B.1.2	With 30 μ M of Fetuin-A	78
B.2	WAXS signal of calcium phosphate complexes	79

B.3	Synthesis of the polyethylene nanoparticles	80
B.4	Influence of the annealing process on $\frac{N}{V}$	81
B.5	Contrast series of PL78	82
B.5.1	Original system - PL78	82
B.5.2	System annealed at 90°C	83
B.5.3	System annealed at 105°C	84
B.5.4	System annealed at 115°C	85
B.6	Synthesis of sPB	86
B.7	X-ray diffraction of BK280	87
B.8	DLS of BK280	88
B.9	Models investigated for the SAXS-CV of BK280	89

Chapter 1

Introduction

During the last decades, Small Angle X-ray Scattering (SAXS) became a powerful technique in colloidal science for the determination of shape, size and internal structures of nanoscale objects in the size range of few nanometers [1] up to about 300 nm [2].

Calcified particles have been extensively studied within the last decades [3–5]. Their formations are of importance for clinical reasons and are investigated from the second part of last century [6–8]. Amorphous calcium phosphate formation has been the subject of numerous investigations in the past concerning their structure [9,10], stability [9] and transformation into other crystalline phases [11]. However, the evolution of these complexes remains poorly understood.

Few years ago, the formation of calcium carbonate precursor particles have been successfully presented by Time-Resolved-SAXS (TR-SAXS) [12] and it has been shown that a double hydrophilic block-copolymer is responsible of the slow down of the aggregation of these particles [13]. The authors of reference [12,13] demonstrated that the formation of calcified objects can be monitored and investigated as well by the help of TR-SAXS experiments. Lately, the interaction between proteins and calcium phosphate particles has been discovered [14,15] but no study investigated the earliest stage of calcium-phosphate formation up to that time [16,17].

The first part of this thesis is to investigate the formation at the earliest stage of calcium phosphate particles and to study the effect of a protein called Fetuin-A onto the calcification process. TR-SAXS by using a Synchrotron source was used to explore this formation.

Polybutadiene is one of the most synthesized polymer system which is found for instances in tyres [18,19]. Since the Second World War, new syntheses in bulk of these sys-

tems appear but none of these products permit to create nanoparticles of polybutadiene. A new synthesis has recently emerged for the formation of semicrystalline nanoparticles of syndiotactic polybutadiene [20].

The second part of this thesis is to characterize the structure of these 1,2-polybutadiene nanoparticles as obtained from reference [20].

From the wide range of polymers, polyethylene (PE) is the most extensively studied system [21–24]. In the literature, experiments onto bulk PE or gels have been investigated by SAXS experiments in order to study the crystallization, melting, annealing or the local deformation under stress [25–28]. However, the annealing process of semicrystalline PE is still badly understood [29]. In the last few years, a new synthesis of PE has been introduced leading to free PE nanoparticles dispersed in aqueous solution [30–32]. In 2007, Weber and coworkers studied such a system by combining SAXS measurement and cryogenic transmission electron microscopy [33]. They demonstrated that these particles are composed of a remarkably thin layer of crystalline PE sandwiched between two amorphous layer of this polymer.

The last part of this thesis is to study the effect of the annealing process onto these well-defined PE nanoparticles. The aim is to find a relationship between the annealing temperature and the reciprocal of the crystalline thickness as predicted in literature [29, 34]. These experiments will be realized by the help of Contrast Variation (CV) technique.

Chapter 2

Theory of SAXS

Small-Angle X-ray Scattering (SAXS) is a suitable tool to investigate the morphology including the inner structure and interactions of nanoscale objects [12,13]. In the following, the theory part will be restricted to basics needed during this thesis.

2.1 Basis of SAXS theory

The diffraction phenomena occur when, by illuminating an object with coherent radiation, each point of this object may be regarded as a second source of a spherical wave. These secondary waves have the same frequency as the original coherent radiation, but due to their different path lengths, they differ by their phases.

A schematic description of the scattering principle is shown in figure 2.1. X-rays from the source X, ideally monochromatic, strike the sample S. Most of the radiation is going straight through the sample while a small fraction of the beam is deviated of an angle θ with the direction of the incoming beam. The deviated scattering intensities, defined by the square of the scattering amplitude, are recorded by the help of a detector D depending on the scattering angle θ . An analysis of the data collected at all studied angles permits to get information of the structure of the sample.

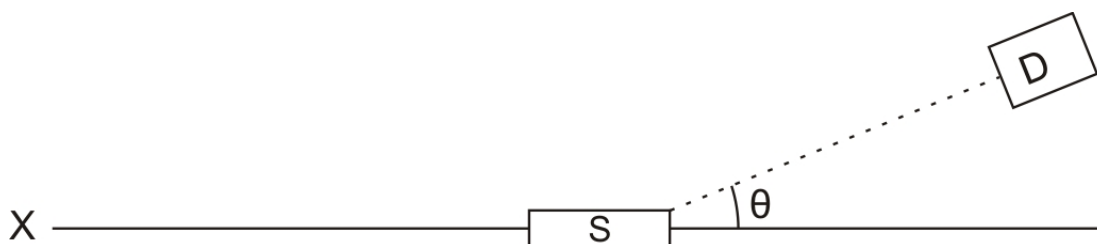


Figure 2.1: Basic principle of the diffraction phenomenon. An incident ray, produced by an X-ray source X, strikes a sample S. A detector D records an ensemble of intensities scattered at different angles θ .

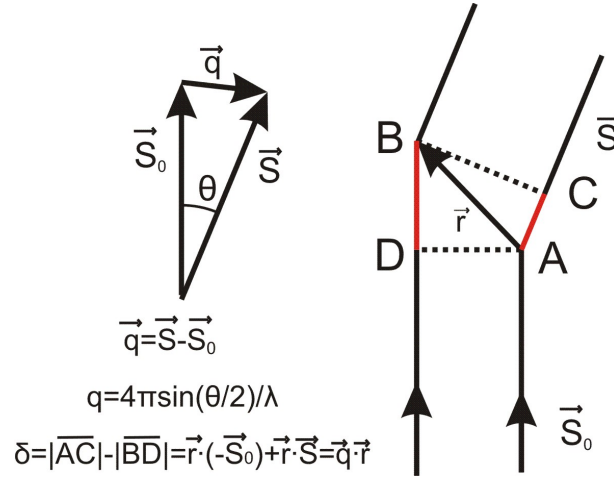


Figure 2.2: Determination of the phase difference between two scattering centers A and B in a particle. \vec{S} and \vec{S}_0 represent the unit vectors in the direction of scattered and incident beam respectively. θ is the scattering angle and \vec{q} the scattering vector.

The determination of the phase difference δ between two scattering centers A and B with a distance of \vec{r} is presented in figure 2.2. For a scattering angle θ , the scattering vector q is defined by [35]:

$$q = |\vec{q}| = \frac{4\pi}{\lambda} \sin(\theta/2) \quad (2.1)$$

where λ is the wavelength of the incident beam. The scattering amplitude observed at q depends on the electron density distribution $\rho(r)$ of the scattered particle and is defined by a Fourier transform. The scattering amplitude of an irradiated volume V is given by [35]

$$A(q) = \int_V \rho(r) e^{-iqr} dr \quad (2.2)$$

The scattering intensity of one single particle $I_0(\vec{q})$ is given by the product of the amplitude and its complex conjugate $A^*(q)$

$$I_0(q) = A(q) \cdot A^*(q) \quad (2.3)$$

In the present study, only symmetric particles will be studied. It results:

$$I_0(q) = [A(q)]^2 = (\Delta\rho)^2 V_p^2 P(q) \quad (2.4)$$

with $\Delta\rho = \rho_s - \rho_m$ the electron contrast of the system s (with electron density ρ_s) in the medium m (with electron density ρ_m) and V_p is the volume of the particle. $P(q)$ is the form factor of a single particle.

2.2 Scattering function of monodisperse particles

2.2.1 Spherical particles

The scattering amplitude $A(q)$ of a spherical homogeneous particle of radial density $\rho(r)$ and radius R_0 is determined by:

$$A(q) = 4\pi \int_0^{R_0} \rho(r) \frac{\sin(qr)}{qr} r^2 dr \quad (2.5)$$

The scattering intensity $I_{0,sp}(q)$ of a single spherical particle, equals to the square of its amplitude, can be analytically solved and we obtain:

$$I_0(q) = (\Delta\rho)^2 V_p^2 \left\{ \frac{3(\sin(qr) - (qr) \cos(qr))}{(qr)^3} \right\}^2 = (\Delta\rho)^2 V_p^2 P(q) \quad (2.6)$$

$P(q)$ is the form factor of a spherical particle. At high q -values, the form factor $P(q)$ is proportionnal to:

$$\lim_{q \rightarrow \infty} \left\{ \frac{3(\sin(qr) - (qr) \cos(qr))}{(qr)^3} \right\}^2 \propto \frac{1}{q^4} \quad (2.7)$$

2.2.2 Disk-like particles

In case of cylindrical and disk-like particles, one can consider a particle of length L (along a z -axis \vec{r}_z) and a radius R_0 (along a radial component \vec{r}_c). The internal coordinate \vec{r} could then be written as $\vec{r} = \vec{r}_z + \vec{r}_c$. By assuming that the scattering density does not depend on z , the scattering amplitude $A_{sp}(q)$ could be split into two factors leading to:

$$A(\vec{q}) = \int_{-L/2}^{+L/2} \exp(i\vec{q}\vec{r}_z) dz \cdot \int_0^{R_0} \rho(r_c) \exp(i\vec{q}\vec{r}_c) dr_c = L(\vec{q}) \cdot R(\vec{q}) \quad (2.8)$$

According to Guinier [36], the first factor $L(\vec{q})$ could be written as

$$L(\vec{q}) = L \frac{\sin(Lq\alpha/2)}{Lq\alpha/2} \quad (2.9)$$

where α is the cosine of the angle between \vec{q} and the z -axis. Fournet [37] demonstrated that the second factor could be written as:

$$R(\vec{q}) = \pi R_0^2 \rho \frac{J_1(qR_0\sqrt{1-\alpha^2})}{qR_0\sqrt{1-\alpha^2}} \quad (2.10)$$

where $J_1(x)$ denotes the Bessel function of the first order. The scattering intensity $I_0(q)$ of a single disk-like particle of thickness L and radius R_0 is then given by

$$I_0(q) = (\Delta\rho)^2(\pi R_0^2 L)^2 \left\{ \int_0^1 \frac{\sin(Lq\alpha/2)}{Lq\alpha/2} \frac{2J_1(qR_0\sqrt{1-\alpha^2})}{qR_0\sqrt{1-\alpha^2}} \sin(\alpha) d\alpha \right\}^2 = (\Delta\rho)^2(\pi R_0^2 L)^2 P(q) \quad (2.11)$$

$P(q)$ is the form factor of a disk-like particle.

2.2.3 Local fluctuations

At high q -values, in the special case of low density systems, there exists an additional term. This scattering contribution in high- q regions is due to the density fluctuations within the particles and is described by an Ornstein-Zernike term [38]:

$$I_{fluc}(q) = \frac{I_{fluc}(0)}{1 + q^2\xi^2} \quad (2.12)$$

where ξ is the average correlation length and $I_{fluc}(0)$ is an adjustable parameter.

2.3 Polydispersity

The special case of scattering of one single particle has been discussed so far. In SAXS experiments, it is evident that the different systems studied contain more than one particle in solution. For example, a system of spherical homogeneous nanoparticles with radius $R_0=100$ nm, weight density $\rho_w=1\text{g/cm}^3$ and a weight fraction of 1 wt% contains ca. 2.4×10^{11} particles per cubic centimeter. Despite of the big progress in producing systems as monodisperse as possible, all systems studied remain polydisperse. In the absence of interparticle interactions, the total scattered intensity $I(q)$ of particles is then the sum of the intensities scattered by each particle (see reference [36] for instance) and is given by:

$$I(q) = \sum_i I_0(q) = \sum_i V_{p,i}^2 (\Delta\rho)^2 P(q) \quad (2.13)$$

where $P(q)$ is the form factor, V_p the volume of the particle i and $\Delta\rho$ is the electron contrast. For the simulation of SAXS experiments of polydisperse systems, the following equation is used:

$$I(q) = \frac{N}{V} \sum_{i=1}^n d(r_i) V_{p,i}^2 (\Delta\rho)^2 P(q) \quad (2.14)$$

where N is the number of nanoparticles in the volume V and $d(r_i)$ is a normalized distribution function. For all simulations realized in this work, a normalized Gaussian

distribution has been used thus $d(r)$ is defined by:

$$d(r) = \frac{1}{\sigma\sqrt{2\pi}} \exp\left\{-\frac{(r - R_0)^2}{2\sigma^2}\right\} \quad (2.15)$$

where R_0 is the mean size of the particle and σ is the standard deviation. An example of the effect of polydispersity is presented in the appendix page 68 in figure A.1 for the special case of polydisperse spherical particles.

2.4 Interparticle interactions

The theory discussed so far remains true for the ideal case of single particles non-interacting with each other, which is the case for diluted samples. However, it is evident that interparticle interactions must exist especially for concentrated solutions.

2.4.1 Aggregation

The process of aggregation of small particles to form larger clusters is technologically and scientifically of great importance. Two ways of aggregation exist: one from single particles and one from already aggregated systems. In this section, only the aggregation issued from single particles will be discussed.

An important parameter in the description of the formation of aggregates of particles is the fractal dimension d_f [39], previously called the Hausdorff-Besikowitch dimension, which describes how the total mass M of the cluster increases with the distance r to its center:

$$M(r) \propto r^{d_f} \quad d_f < d \quad (2.16)$$

d_f can take a non-integer value between 1 and the dimension of the single particle d . According to reference [36], the scattering intensity $I(q)$ of aggregating homogenous spherical systems of radius R_0 and electron contrast $\Delta\rho_0$ could be written:

$$I(q) = \left\{ \Delta\rho_0 \int_0^\infty e^{-iqr} dr \right\}^2 = V_p^2 (\Delta\rho_0)^2 P(q)^2 S(q) \quad (2.17)$$

where $S(q)$ is the structure factor of the particles, describing the interparticle interactions, and takes into account the scattered intensity corresponding to distances higher than R_0 . Thus:

$$S(q) = \mathcal{N} \int_{R_0}^\infty g(r) e^{-iqr} dr \quad (2.18)$$

\mathcal{N} denotes here the total number of particles. $g(r)$ is the particle pair-correlation function and describes the probability of having two particles separated by a distance $2r$ from each other. By taking into account the size ξ of the cluster, the pair-correlation function is rendered as:

$$g(r) = \frac{A}{r^{d-d_f}} e^{-r/\xi} \quad (2.19)$$

where A is a constant. Using the relation in equation 2.18 and performing a Fourier transform result to:

$$S(q) = 1 + \frac{S_0}{[1 + q^2 \xi^2]^{(d_f-1)/2}} \frac{\sin[(d_f - 1) \tan^{-1}(q\xi)]}{(d_f - 1)q\xi} \quad (2.20)$$

with S_0 defines as:

$$S_0 = C(d_f - 1)\Gamma(d_f - 1)\xi^{d_f} \quad (2.21)$$

where

$$\Gamma(x) = \int_0^{\infty} t^{x-1} e^{-t} dt \quad (2.22)$$

and C is a constant. Since

$$\lim_{x \rightarrow 0} \frac{\sin(\tan^{-1}(x))}{x} = 1 \quad (2.23)$$

$S(0)=1+S_0$ defines the number of particles per aggregate.

2.4.2 Polymer Reference Interaction Site Model - PRISM

The PRISM theory is derived from the Reference Interaction Site Model (RISM) developed by Chandler and co-workers [40–44]. In this part, only the general aspect behind the RISM will be describe.

The PRISM bases on liquid state integral equation theory which was originally developed for atomic and small molecule fluids [45]. Given an interparticle potential, the theory provides an interparticle pair correlation function. This pair correlation function is connected with the structure factor $S(q)$ measured in SAXS by Fourier transform. In the particular case of this study, the PRISM describes the equilibrium structure and properties of polymers in bulk solution. The main approximation thereby is that all sides of a particle are equivalent. Thus the particle interaction problem is reduce to a simple problem. More information about the PRISM theory and application could be found in references [45, 46].

2.5 Contrast Variation

The scattered intensity $I(q)$ of an ensemble of N particles of volume V_P in a volume V is given by:

$$I(q) = \frac{N}{V} (\Delta\rho)^2 V_P^2 P(q) S(q) \quad (2.24)$$

with $\Delta\rho = \rho_s - \rho_m$ where ρ_s and ρ_m define the mean electron density of the system and the medium. According to equation 2.24, varying the electron density of the medium ρ_m lead to different resulting intensities. Figure 2.3 displays a schematic view of the contrast variation technique: changing the electron density of the solvent corresponds to a change of the color of the background. There are two extreme cases: infinite contrast and zero contrast. At a contrast of $\pm\infty$ (case a and e in figure 2.3), only information about the overall size and shape could be obtained. When the electron density of the solvent is equal to one the mean electron density of the particle, then only the derivations, due to different internal contrast, are visible. Measuring the same system with different contrast lead to a complete investigation of the structure of heterogenous systems. In praxis, contrast variation is not often used in conventional SAXS due to the difficulty to change only the electron contrast ρ_m of the medium without modifying the structure of the investigated system in the same time.

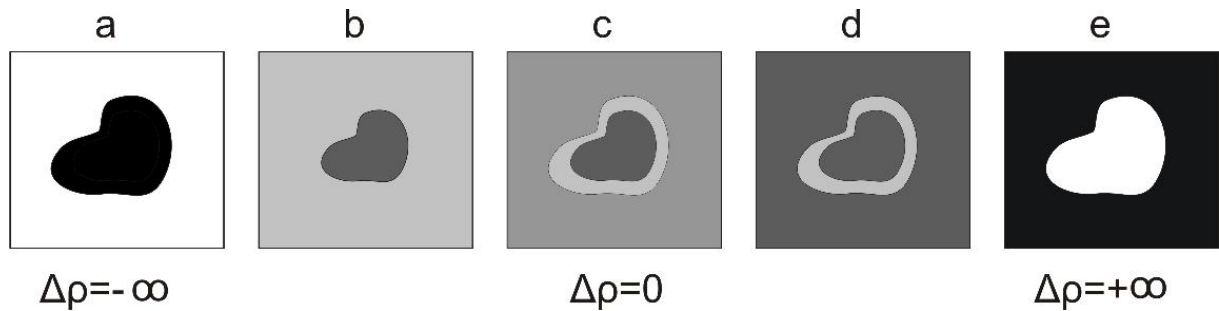


Figure 2.3: Schematic representation of the contrast variation. Different electron densities of the solvent help to detect substructures of the system. This method permits then to study the total structure and the different phases present in the analyzed particles in detail. $\Delta\rho$ defines the electron contrast of the studied system relative to the medium.

Chapter 3

Generalities

3.1 Calcification

Calcification is the process in which the mineral calcium builds up in soft tissue, causing it to harden. The first appearance of biomineralization in History is documented in the Precambrian invertebrate *Cloudina* [47], a shelly tube-like fossil. In order to control this mineralization, potent inhibitors of spontaneous calcification must exist. The multiplicity of the existing phases of calcium phosphate complexes (see table 3.1) is as well an important parameter in the complexity of the chemical equilibrium engaged. Vertebrates, including Human, contain these phases which are found mostly everywhere in the body (bones, ligaments and even muscles) but at different concentrations. The mechanism of regulation of calcium and phosphate concentration in the Vertebrates is really far from being completely understood.

Phase	Acronym	Empirical formula	K_{sp}
Amorphous calcium phosphate	ACP	$\text{Ca}_3(\text{PO}_4)_2 \cdot x\text{H}_2\text{O}$	-
Dicalcium phosphate dihydrate	DCPD	$\text{CaHPO}_4 \cdot 2\text{H}_2\text{O}$	$1.87 \times 10^{-7} \text{ M}^2$
Dicalcium phosphate anhydrous	DCPA	CaHPO_4	$9.2 \times 10^{-7} \text{ M}^2$
β -tricalcium phosphate	TCP	$\text{Ca}_3(\text{PO}_4)_2$	$9.2 \times 10^{-29} \text{ M}^5$
Octacalcium phosphate	OCP	$\text{Ca}_8\text{H}_2(\text{PO}_4)_6 \cdot 5\text{H}_2\text{O}$	$2.5 \times 10^{-99} \text{ M}^8$
Hydroxyapatite	HAP	$\text{Ca}_{10}(\text{PO}_4)_6(\text{OH})_2$	$5.5 \times 10^{-118} \text{ M}^9$

Table 3.1: Different phases of calcium phosphate complexes and their respective solubility products K_{sp} . M unit is mol/L. Data obtained from reference [48].

The understanding of the formation of calcium phosphate complexes is hardly investigated especially since the middle of last century. In 1967, Walton and co-authors demonstrated that Hydroxyapatite and Octacalcium phosphate may not be the initial phase of calcium phosphate complexes [49]. There is no doubt about the nature of precipitation of these ions at early stage of calcification but this initial product is still not precisely known and depends mainly on parameters such as temperature, pH or solvent. It is now generally

recognized that the first compound formed from soluble salts is a metastable precursor phase [48]. This precursor phase, also called Amorphous Calcium Phosphate (ACP), has been widely studied by changing the calcium to phosphate ratio [50], their initial molar product [6] or the experimental temperature [51]. Kinetic studies of the structuration of calcium phosphate complexes has been performed recently [52]. These authors mixed Dicalcium Phosphate Dihydrate (DCPD) with Calcium Oxide (CaO) and detected the formation of nanoHydroxyApatite (nano-HA) particles within few hours by the combination of X-Ray Diffraction (XRD) and Differential Scanning Calorimetry (DSC) measurements. The structuration of the initial calcium phosphate complexes (DCPD) is very similar to ACP according to the present study (see page 29 in chapter Calcification at early stage). Vascular calcification (VC), that is deposition of calcium phosphate mineral in cardiovascular tissues including arteries, heart valves and cardiac muscles, is often encountered in the development of atherosclerotic intimal lesions and is a common consequence of aging [53]. VC is positively correlated with increased risk of myocardial infarction and of dissection after angioplasty [54]. In 2000, Jono and coworkers demonstrated that different levels of phosphate regulates human smooth muscle cell calcification through a sodium-dependent phosphate transporter-sensitive mechanism and implicate this mechanism in the development of ectopic calcification in vivo [55].

Kinetically and structurally speaking, the formation of the precursor particles of calcium phosphates complexes leading to the precipitation of the ions is unclear. A huge number of scientific articles are proposing Monte-Carlo simulations in order to better interpret such a behaviour (see for instance references [56, 57]). Authors of reference [57] demonstrated that the solution may be divided into three regimes: the first one presents individual monomers in solution, in the second regime, small clusters of monomers are forming and in the last case, large particles are formed.

However, the calcification process is far much more complicated and it is evident that additional molecules play a significant role in the formation of teeth or bones [58]. The formation of calcium phosphate complexes has been investigated by using functionalized macromolecules as templates. For instance, Holt and coworkers [59] used β -casein phosphopeptides as stabilising agent and demonstrated that the peptide covered nanoparticles of calcium phosphate. Enlow et al. [60] created an organized network of 20 nm diameter calcium phosphate nanospheres by the help of copolymers, Li [61] showed that β -cyclodextrin is the only macromolecule of this family which is able to stabilize the amorphous phase of ACP. In 2002, Combes and Rey studied the growth of calcium phosphate complexes in presence of BSA proteins and proposed a schematical representation of crystalline OCP covered by an adsorbed layer of BSA to prevent further growth of the nanoparticles [62]. The long way to understand the complexity of calcification is far from being achieved.

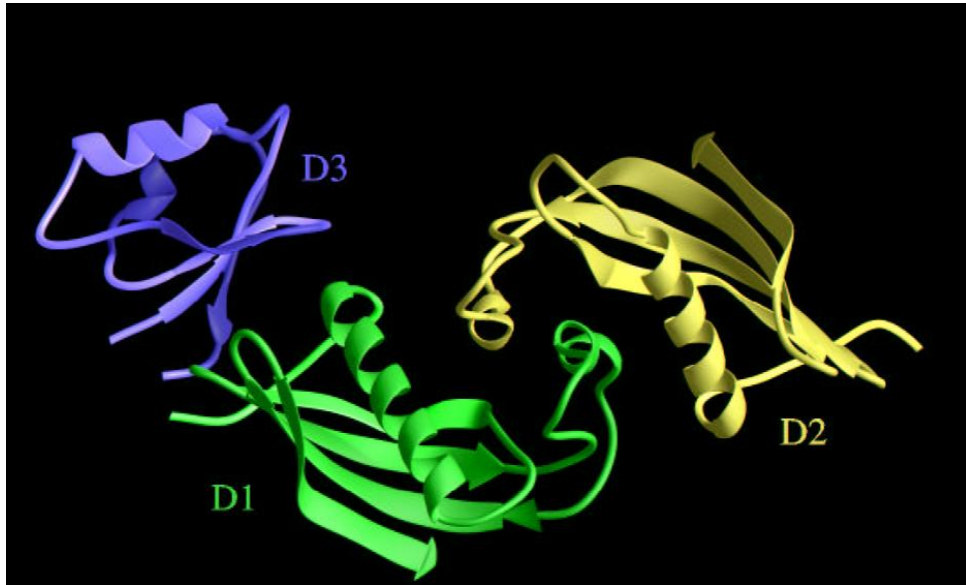


Figure 3.1: Model of the three domains of Fetuin-A. D1 and D2 remain of the Cystatin Superfamily while D3 has a structural homology with an insertion domain. Picture taken from reference [63].

Since some years, the properties of a particular protein are of remarkable interest in the field of mineralization: α_2 -HS-glycoprotein (ahsg) also called Fetuin-A (see structural model of the protein in figure 3.1). The name α_2 -HS-glycoprotein refers to the fact that this protein migrates with the α_2 fraction of serum proteins upon traditional cellulose acetate paper based electrophoresis. H and S reminds of Heremans [65] and Schmid [66],

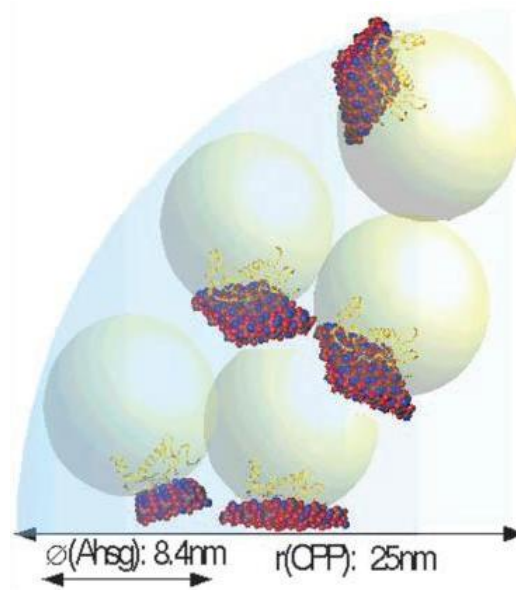


Figure 3.2: Hypothetical model of a calciprotein particle (CPP) consisting of aggregated calcium-phosphate-Fetuin complexes. Figure taken from reference [64].

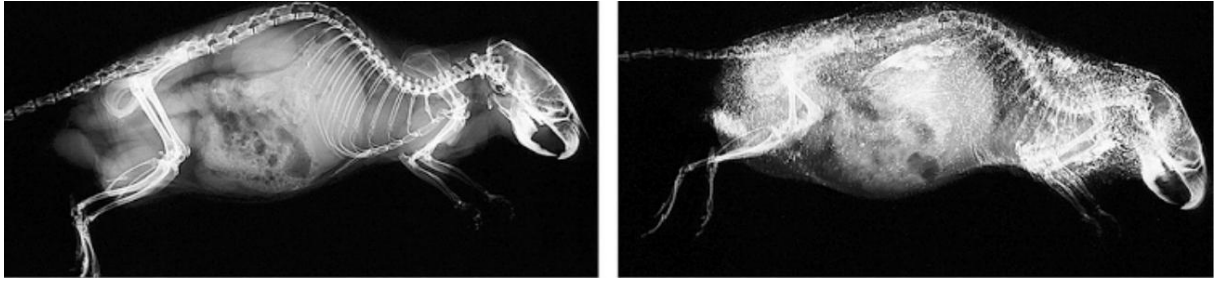


Figure 3.3: Radiological analysis of 9-months-old mice. The mouse in the right is genetically deficient in Fetuin-A production while the one on the left is a wild type mouse. The lack of Fetuin-A is characterized by a strong calcification in extracellular space. Picture taken from reference [72].

the co-discoverers of this protein in humans [67]. The name Fetuin is coming from the latin word *fetus* and has been given to this protein for its abundance in fetal calf serum [68]. Finally, this glycoprotein is called Fetuin-A after the recent discovery of a second Fetuin, Fetuin-B [69]. The abundance of Fetuin-A in bone suggests that the glycoprotein may have a role in bone formation or remodeling. In 1996, Schinke and coworkers [70] were the first to suggest a possible role of inhibitor in mineralization for this protein. In the following years, it has been shown that Fetuin-A acts as a systemic inhibitor of calcification [15,71] and that Fetuin-A is responsible of the formation of a Fetuin-mineral complex called calciprotein particle (CPP [64]). An hypothetical model of CPP is displayed in figure 3.2. A recent work [72] showed that mice genetically modified not to synthesize Fetuin-A displayed after 4 months a severe systemic calcification phenotype (see figure 3.3).

The first part of this thesis will present a study of the influence of Fetuin-A onto the earliest stage of calcification by the combination of time-resolved SAXS measurements, dynamic light scattering and transmission electron microscopy.

3.2 Polybutadiene

Depending on the structural variations of the components in the polymeric materials, the chemical structures of polymers is subject to change. Polybutadiene (PB) consists of three isomeric units: cis-1,4, trans-1,4 and 1,2-vinyl. Furthermore, the 1,2-vinyl structure has three possible sequence arrangements along the backbone chain: isotactic-, syndiotactic and atactic-1,2 units [73,74]. Other catalyst systems that can produce syndiotactic polymers with controllable constitution and configuration have been used and some works on synthesis, thermal behavior, crystallization, structure and morphology of syndiotactic polybutadiene (sPB) have been published [75–79].

sPB is a thermoplastic elastomer of industrial interest due to its properties of both plastics and rubbers. This polymer may be found in “packaging breathing” items for fruits, vegetables and seafood because of its higher carbon oxide gases and oxygen permeability and better resistance against wetting and slippage, in molding application such as molded bottles, adhesive, oil paint, photosensitive resin, plastic materials, tire treadings in adhesives or in footwears for instance [80,80,81]. The adjective syndiotactic means that crystalline sPB has a stereoregular structure in which the side-chain vinyl groups are located alternatively on the opposite sides in relation to the polymeric main chain. Figure 3.4 presents a schematical representation of sPBD.

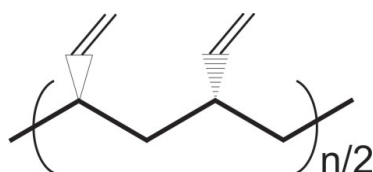


Figure 3.4: Schematical representation of syndiotactic 1,2-poly(1,3-butadiene). We note a regular alternation of the CH-CH₂ bond behind and before the plane of the acyl chain.

sPB was first synthesized by Natta [82] in 1955 and its structure was determined one year after by the help of X-ray diffraction [83]: orthorhombic packing (P_{acm} , $a=10.98 \text{ \AA}$, $b=6.60 \text{ \AA}$ and $c=5.14 \text{ \AA}$). Such polymers samples are now synthesized with a purity of 1,2 content of 97% (see e. g. reference [84]). Up to now, little attention has been paid to the structuration of nanoparticles of sPB [74,85,86].

Using an in-situ cobalt catalyst [87], very small semicrystalline nanoparticles of sPB could be synthesized (see synthesis of these nanoparticles in appendix page 86). These particles have a diameter of the order of 14 nm and do present a crystallisation percentage around 50% [20]. The second part of this thesis is to present the structural analysis of these sPB nanoparticles by using the combination of SAXS and cryo-TEM experiments.

3.3 Polyethylene

Crystallization of polyethylene (PE) is among the classical subjects of polymer science. In 1957, Till [88], Fisher [89] and Keller [90] independently demonstrated that PE crystallizes by chain folding leading to a lamellar structure. In order to initiate the spontaneous formation of chain-folded lamellae, the crystallization temperature needs to be high enough to permit the requisite molecular motions.

In the special case of surface nucleation, the lateral surface free energy σ could be written as [91,92]:

$$\sigma = T \frac{\Delta h_f a_0 l_b}{T_m} \frac{1}{2 l_u C_\infty} \quad (3.1)$$

where Δh_f is the heat of fusion, T_m the melting point, a_0 the width of the chain, l_b the bond length, l_u the C-C distance and C_∞ is an empirical parameter determined to 6.7 for the special case of polyethylene [93]. Two different types of folds are described in the literature [93]: sharp-fold and tight-fold. The sharp-fold is defined as an emergent chain that executes a transit to an adjacent where it re-enters the lamella of origin. The tight-fold is described as one emergent chain that re-enters within the lamella of origin with a minimal traverse length with little amorphous contribution (See the schematical representations in figure 3.5).

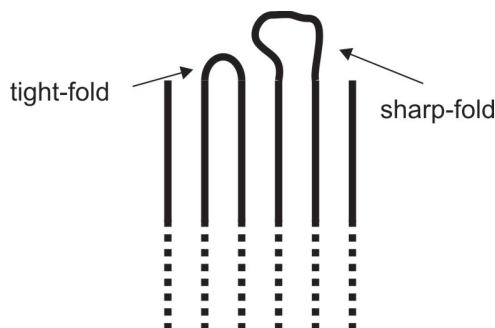


Figure 3.5: Schematical representation of sharp- and tight-folded chains of crystalline polymers.

The kinetic of the growth of the crystallites along the lateral axis depends mainly of the reptation in the melt. The reptation refers to the deformation of the chains so as to create the fold itself. This reptation highly depends on the viscosity η within the amorphous phase of the polymer and thus on the molecular weight of the polymer. For the case of polymers with high molecular weight, the reptation may occur on different parts of one chain and, after a critical period of time, the resulted structures may be removed leading to a decrease of the kinetic of the growth of the crystallites. The reader may refer to part II of reference [93] for more details about the reptation.

Solution-grown crystals of PE usually have lateral dimensions of the order of some micrometers and are difficult to handle. At low temperature, PE crystals precipitate on cooling to form platelets which have the appearance of a lozenge [94]. Such a morphology could be explained as shown in figure 3.6 [95–99]: The faces 100 disappear as they grow faster than the 110 resulting to a lozenge shape. In the literature, the crystalline thickness of PE varies between 10 and 20 nm and a correlation between the inverse of this thickness and the temperature of the synthesis has been found [100].

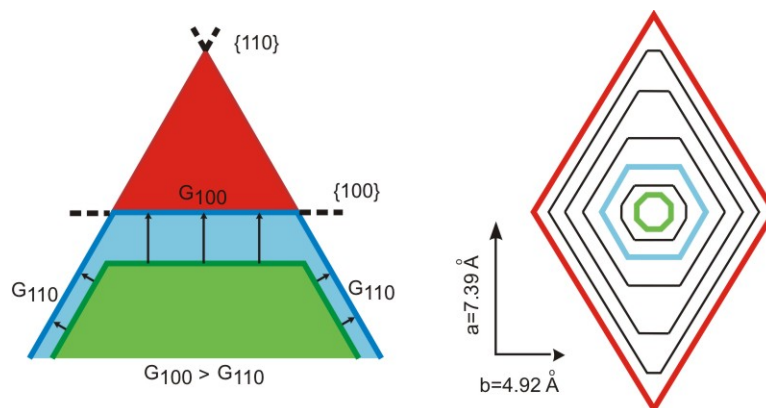


Figure 3.6: Schematic growth of a nascent PE nanocrystal. The faces 100 disappear as they grow faster than the 110 (left), resulting to a lozenge shape (right). The letter G refers to the growth along the face.

During the last decades, the mechanism of recrystallization of lamellar PE crystals after melting has been extensively studied [101, 102]. However, the process in which recrystallization occurs is not yet fully understood. In 1975, Windle analyzed the annealing of multi-lamellar PE crystallized in solution by an X-ray diffraction study and suggested an asymmetric step-like thickening of the crystalline phase [103]. Twenty years ago, Sadler and Spells demonstrated by the combination of neutron scattering and infrared spectroscopy that a localized solid-state transformation is involved during heating close to the melting temperature [104, 105]. In 1997, Rastogi and coworkers showed that PE crystalline lamellae are doubling in size during annealing and explained it by stacking of crystalline adjacent lamellae [106]. In 2001, microscopic studies [107] show that the annealing process may occur at temperature slightly above the crystallization temperatures and far below the melting temperatures of the crystals. However, none of these studies explain the morphology of swiss-cheese-like shapes observed after the annealing of lozenge-like crystalline PE particles [101]. Most of the previous studies so far have been performed on PE bulk or by means of macroscopic PE crystals.

Up to the end of last century, polymer latexes were polymerized exclusively by free-radical processes [108, 109]. Since the beginning of the 21st century, a new route of polymer-

ization of PE particles emerged: catalytic polymerization in aqueous dispersion [30–32]. Stable aqueous dispersions of surfactant-stabilized polymer nanoparticles in the range of 50 to 500 nm diameter are obtained. In 2007, Weber and coworkers [33] presented a complete analysis of these PE nanoparticles by using a combination of cryo-TEM and SAXS experiments. These particles consist of a remarkably thin crystalline single layer of PE (6.5 nm) sandwiched between two amorphous polymer sheets (“nano-hamburgers”).

Thermodynamically, the formation of the polymer crystallites had become of a strong interest in the last few years [110,111]. In 2009, Strobl proposed an hypothetical scheme (see figure 3.7), depending exclusively on the temperature T and on the number of structure unit per crystalline chain n , that might explain the formation and recrystallization of polymer crystalline particles [34]: A precursor formation of a mesomorphic inner structure (point (1) in figure 3.7) occurs and polymer chains rearrange themselves to quasi-stretched conformations but not close enough to each other to form a density equivalent to the crystal itself (between points (1) and (2)). Once the stretched chains reach a certain limit, the layers thicken to form the native crystalline phase (point (2)). The passage from the crystallization line up to the recrystallization one is still matter of debate. In 2005, Strobl assumed that no elongation of the crystalline thickness occurs during the annealing while,

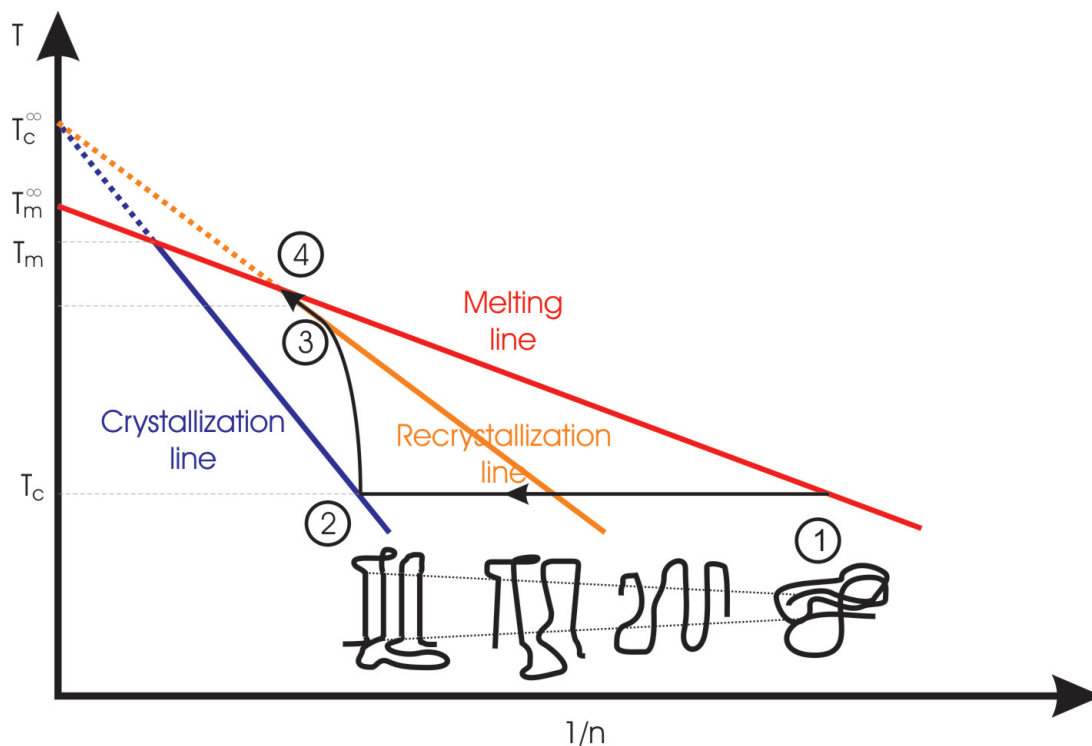


Figure 3.7: Thermodynamic scheme of polymer crystals proposed in literature [34]. n defines the number of structure unit per crystalline chain, see text for further explanations. This scheme is still under debate especially the pathway from point 2 to 3.

in 2009, Heck and coworkers detected a growth of the thickness of crystals of high density polyethylene (HDPE) by the help of TEM micrographs during annealing [29,112]. Further increases of the temperature lead to the formation of thicker crystallites, molten polymers (point (4) in figure 3.7) and finally the existence of entanglement rearrangements.

According to the theory of crystallization, the crystallization line could be written in terms of thermodynamic parameters [34]:

$$T_c^\infty - T = \frac{2\sigma_{mc}T_c^\infty}{\Delta h_c} \frac{1}{n} \quad (3.2)$$

T_c^∞ denotes the melting temperature of an infinite crystal, Δh_c defines the heat of fusion of a crystalline PE and σ is the surface free energy of an original crystal (mc). Proceeding in analogous manner, one obtain for the recrystallization line

$$T_c^\infty - T = \frac{2\sigma_{ma}T_c^\infty}{\Delta h_c} \frac{1}{n} \quad (3.3)$$

and for the melting line:

$$T_m^\infty - T = \frac{2\sigma_a T_m^\infty}{\Delta h_a} \frac{1}{n} \quad (3.4)$$

T_m^∞ is the melting temperature of an infinite crystal. σ_{ma} and σ_a are the surface free energy of an annealed crystal (ma) and an amorphous system (a). It is worth to note that the precise location of these lines in the thermodynamic scheme is still under debate: The thermodynamic parameters that govern equations 3.2 to 3.4 depends on the system studied. They have been drawn based on experimental data for systems such as for instance HDPE, PE with octene or s-polypropylene [29,112]. Quantitative information about the annealing and recrystallization of single-lamellae of pure polyethylene is missing in literature.

The last aim of this thesis is to push forward the work previously realized by Weber et al. [33] by studying the controlled variation of these nanoparticles by thermic treatment. This study will be realized by the combination of SAXS and cryogenic transmission electron microscopy.

Chapter 4

Study of the early stage of calcification

Previous works [16,17,64,113] showed that calciprotein particles (CPP) underwent a two-step ripening process as presented in figure 4.1: A minimum concentration of $7 \mu\text{M}$ of Fetuin-A is necessary in order to stabilize efficiently the CPPs. These primary CPPs are doubling in size after three to six hours. Solutions containing less than $7 \mu\text{M}$ Fetuin-A are stable during the first stage of calcification but paradoxically it is followed by immediate sedimentation, *id est* the secondary CPPs are not stable. Authors of reference [16] have shown by the help of small angle neutron scattering (SANS) that, during this second stage of calcification, CPPs are formed by a spherical core of octacalcium phosphate covered by a layer of Fetuin-A. However, one SANS measurement of a sample requires at least 30 minutes by sample and is not suitable to study the early stage of calcification. Additional experiments have been realized by the help of the transmission electron microscopy technique [64]. This analysis permits to detect that independantly of the temperature, the structure of the CPPs after ca. 2 hours old is a spherical shape.

4.1 Investigation of the early stage

As expected by the work of Heiss and coworkers [17], Fetuin-A has an influence on the calcification process. In the following, the initial stages of the calcification will be investigated. It seems evident that the sizes of the particles detected in the previous studies is coming from a step-by-step process including nucleation and growth of the particles. The goal of this study is to better understand how those particles are created and to get an idea on how the process of the early stage of calcium phosphate mineralization occurs. The chronology of the different calcification stages involved during the formation of the CPPs will be studied by the help of three methods: small angle x-ray scattering, dynamic light scattering and transmission electron microscopy. It has been shown recently that the

SAXS technique is suitable to follow the formation of nanoparticles from supersaturated salt solutions [2,12,13,114]. In a first step, the nucleation process will be presented. Then the first equilibrium state of CPPs particles will be discussed and finally the influence and the effect of the glycoprotein onto the formation of this first state will be demonstrated. This work was realized in deep collaboration with the group of Prof. W. Jahnen-Dechent, especially with Dr. A. Heiss who provided the glycoprotein.

4.1.1 Materials

Ionic solutions of calcium chloride ($\text{CaCl}_2 \cdot 2\text{H}_2\text{O}$, Roth GmbH, Karlsruhe) and sodium phosphate ($\text{Na}_3\text{PO}_4 \cdot 12\text{H}_2\text{O}$, Fluka) were prepared separately in a buffer solution. The buffer is created by adding 8 g of NaCl (Merck), 0.2 g of KCl (Grüssing) and 3 g of tris/HCl (Merck) in one liter of millipore water. The buffer was then adjusted to a pH of 7.4 by the help of a NaOH solution (Merck) and was finally filtered at $0.45 \mu\text{m}$ (VWR). Lyophilized Fetuin from calf serum was obtained from Sigma and used as received. Its molecular weight and density were determined by analytical ultracentrifugation to 50.09 kDa and 1.32 g/cm^3 respectively.

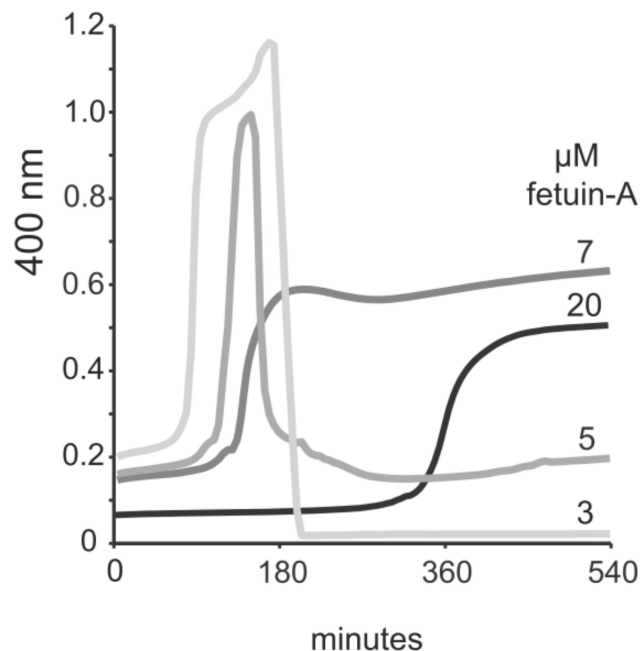


Figure 4.1: Time-resolved turbidimetry measurements indicating that the inhibition mixes were stable down to a concentration of $7 \mu\text{M}$ Fetuin-A. The stability of primary CPPs correlated with the Fetuin-A concentration. Figure taken from reference [17].

4.1.2 Experimental

Samples for TEM were prepared at room temperature by placing a drop of the solution on a carbon-coated copper grid. After one minute, excess solution was removed by blotting with a filter paper.

The DLS setup (ALV-5000/LSE-5004) was thermostated at 37°C and 1.8 mL of calcium solution of concentration 11.1 mM (with the appropriate concentration of Fetuin-A) was inserted in a glass capillary. A solution of phosphate ions (60 mM) was as well thermostated at 37°C and 0.2 mL of this solution were inserted in the capillary. The solution was then mixed by hand and the DLS measurements started ca. 30 seconds after the mixing process. The resulting radial distribution functions were extracted by the help of the ALV software and were plotted so that the highest radial density equals to unity.

SAXS experiments were performed at the Synchrotron ID02 beamline, in Grenoble, France. The sample-to-detector distance was set to 2 meters and the wavelength of radiation was chosen to 1 Å. Two ionic solutions of calcium and phosphate (20 mM and 12 mM, respectively) were prepared in the buffer and the mixing process was achieved at 37°C by a stopped-flow device (BioLogic SFM-3) with a 1:1 mixing ratio. Fetuin-A was adjusted in each ionic solution at the studied concentration: 1 μ M, 5 μ M and 15 μ M. In order to interpret in a quantitative and qualitative manner the aggregation process and the effect of the protein, time-resolved measurements have been performed. The mixing volumes and the mixer flow were controlled with the instrument software. The total mixer flow rate during the final mixing phase was set to an optimum value of 6.67 mLs⁻¹. After 30 ms of continuous mixing and flowing through the capillary, the flow of the reagent mixture through the capillary was stopped and the sample were left unperturbed. The kinetic time evolved above the dead time of the device (ca. 4 ms, that is the time needed to transfer the mixture to the point of measurement in the capillary) after the cessation of the flow. Thus for time $t \leq 35$ ms there are quasi steady-state conditions due to the continuous flow of the reaction mixture. The stopped-flow cell filled with the buffer was taken as the background.

The SAXS experiments at a Synchrotron source are adequate to eventually detect the nucleation of a system during the first seconds [12, 13]. In order to extract the SAXS data, it is necessary to determine the volume fraction of the particles: The densities of the calcein particles were determined through densitometry (DMA 60/602, Paar, Graz, Austria) to be 1.67 g/cm³. The chemical composition of amorphous calcium phosphate (ACP) is not known precisely [6–8, 48, 51, 115, 116]. As expected from the literature [117, 118], the chemical formula of ACP could be written Ca₃(PO₄)₂·xH₂O. By taking

into account the density of tricalcium phosphate (2.89 g/cm^3) and the one of water (1.0 g/cm^3), the number of molecules of water was determined to $x \approx 2$. This approximation leads to the volume fraction ϕ of the calciprotein particles in solution: 0.06 vol%. This value appears very small for a study by SAXS experiments, but it is compensated by the excess electron density which was determined to 536 e/nm^3 for the calcium phosphate phase alone.

SAXS intensities of the empty capillary $I_{ec}(q)$, the buffer solution $I_{bu}(q)$ and of each sample in the buffer $I_{sa}(q)$ were measured separately and the intensity scattered by the sample $I(q)$ alone was determined by the equation:

$$I(q) = I_{sa}(q) - (1 - \phi)I_{bu}(q) - \phi I_{ec}(q) \quad (4.1)$$

The extraction of the data is illustrated on figure 4.2 for a solution containing $15 \mu\text{M}$ of Fetuin-A, 145 seconds after the mixing process.

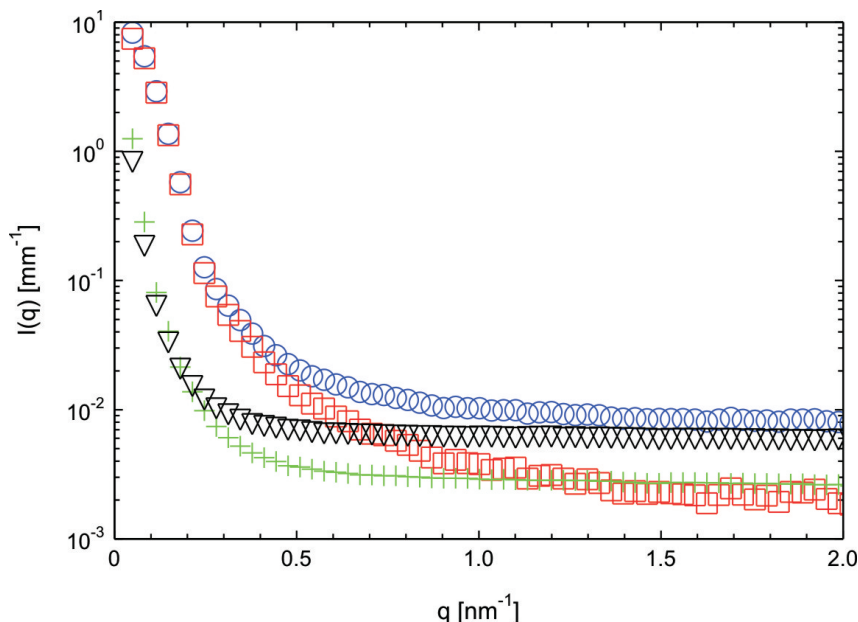


Figure 4.2: Extraction of the data from the measured SAXS scattering intensities according to equation 4.1: After subtraction of the signal due to the capillary (green plus), the intensity of the buffer (black triangle) is subtracted depending on the volume fraction of the sample (blue circle). This results to the red squares.

4.2 Results and discussion

4.2.1 Nucleation

The formation of particles in aqueous solutions from ions depends mainly on the concentration of the compounds that are present in the solution. Minimum concentrations are

needed and should match at least the solubility product K_{sp} of the precursor phase of calcium phosphate complexes [48]. The expected precursor phase of calcium phosphate in aqueous solution is dicalciumphosphate dihydrate, DCPD, $\text{CaHPO}_4 \cdot 2\text{H}_2\text{O}$. According to literature [48], the solubility product of the studied phase with concentrations of 10 mM of calcium ions and 6 mM of phosphate ions leads to:

$$K_S = [\text{Ca}^{2+}][\text{HPO}_4^{2-}] = 6.0 \times 10^{-5} \text{ M}^2 \quad (4.2)$$

which is ca. 5 times higher than the solubility product of DCPD (see table 3.1). Thus, instantaneous calcification is expected.

The total weight fraction of Ca^{2+} and HPO_4^{2-} ions has been investigated by DLS by keeping the same ratio Ca/P (10/6). Figure 4.3 presents the results of these measurements. The final molar concentration of the calcium ions is reported (in mM) in the legend. By using the weight percentage of calcium and phosphate ions (0.04% and 0.1% respectively, id est, 10 mM and 6 mM) like in the work of Heiss [17], particles of the order of 1 μm were detected. The evolution of the radial distribution is interesting here. The use of half of this weight percentage leads to the presence of two different particle sizes: one around 1 μm and one at ca. 100 nm. Another decrease of the concentration of calcium and phosphate, still by keeping the same ratio Ca/P=10/6, leads to only one peak at about 100 nm. The peak at 1 μm is attributed to the aggregation of particles of

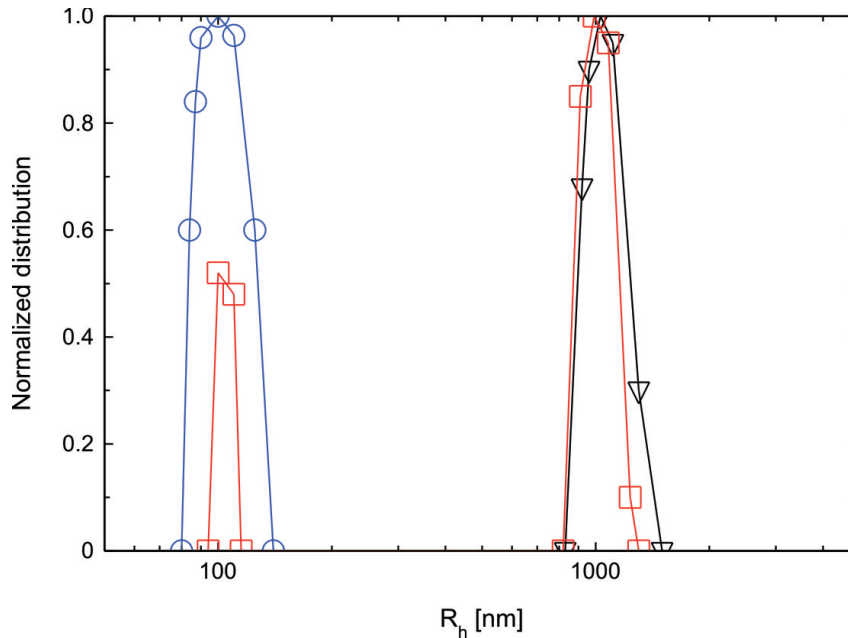


Figure 4.3: Influence of the weight fraction of calcium and phosphate ions onto the size of the primary CPPs. The ration of Ca/P is constant and equals to 10/6. The concentration of calcium ions in the mix are 3.6 μM (black triangles), 5.0 μM (red squares) and 10 μM (blue circles).

size around 100 nm. Due to the experimental procedure, the earliest DLS measurements were achieved ca. 30 seconds after the mixing process. No change in the size of the formed particles were visible during the first four hours after the mixing process. Thus, DLS measurements do not permit to detect the nucleation of the primary particles.

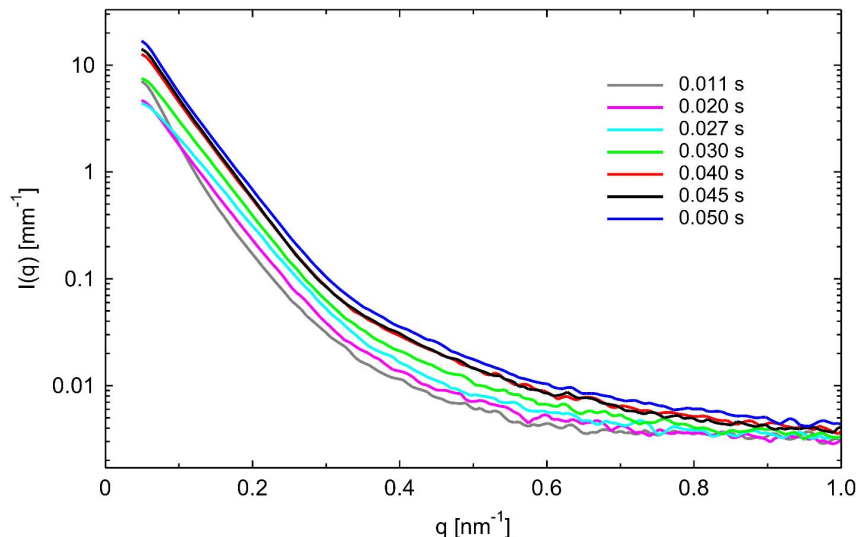


Figure 4.4: Evolution of the SAXS intensities with time in the absence of Fetuin-A at the very early stage. The growth in intensity is characteristic of the nucleation phase, *id est*, the formation of the first precursor particles. The time point of measurement is reported in the legend.

Time-resolved SAXS experiments by using a synchrotron source have been used in order to detect the formation of calcium-phosphate complexes. Figure 4.4 presents the scattered intensities recorded for the sample containing no Fetuin-A at the very early calcification stage, during the first 0.05 second. There are two main points: a growth in intensity at all q -values which is characteristic of a growth of the number of particles. And there is absolutely no change in the shape of the scattered intensities, which means that the morphology and the size of the particles do not evolve. At q -values below 0.15 nm^{-1} , the three earliest scattered intensities overlap themselves. This is attributed to the remaining flow in the capillary (quasi steady state not reached). This creates artefacts in the signal. No further change in intensity were seen for longer times meaning that the number of particles per volume stays constant. This shows the very fast kinetic of the nucleation of calcium phosphate particles. As well, no oscillation of the scattered intensities could be seen which is typical for a very high polydispersity in size of the system. The scattered intensities in figure 4.4 were obtained by changing the initial so-called dead-time, that is the time between the end of the mixing process and the time corresponding to the first measurement. The intensity $I(q)$ is proportional to the number of particles per volume $\frac{N}{V}$, to the square of the electron contrast of the system $\Delta\rho$ and to the square of the volume of the particle V_P (see equation 2.24 page 16). In the special case of nucleation, the

size of the system and its density are constant and the structure factor $S(q)$ is equal to unity. The scattered intensity is then directly proportionnal to the number of particles per volume $\frac{N}{V}$. The time-evolution of the scattered intensity at a certain q -value permits then to qualitatively study the nucleation process. At q -values below 0.15 nm^{-1} , artefacts appear and they are attributed to the remaining flow in the capillary (figure 4.4). Data at q -values higher than ca. 0.45 nm^{-1} are more subject to noise and these intensities will be later on attributed mainly to the density fluctuation of the amorphous system. It results that the nucleation of this system could be studied by following the scattered intensities recorded between 0.15 and 0.45 nm^{-1} .

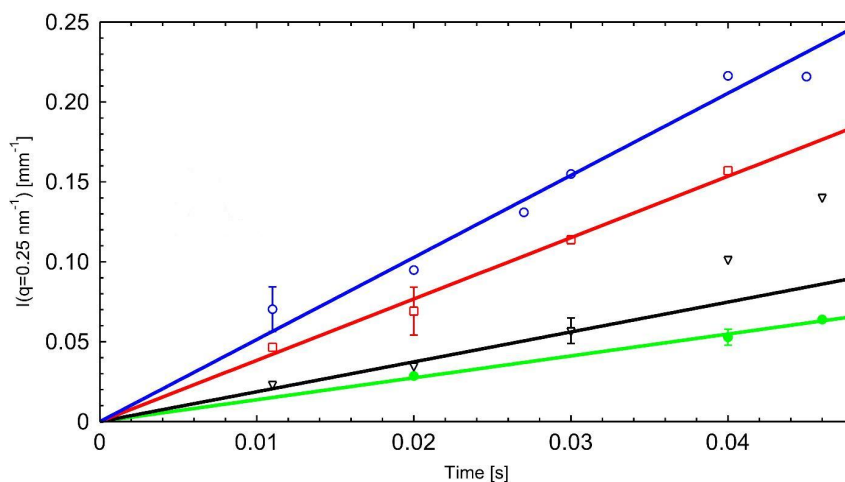


Figure 4.5: Time-evolution of the intensities collected at $q=0.25 \text{ nm}^{-1}$ for the earliest SAXS intensities collected. The formation of the primary particles follows a kinetic of first order. The kinetic constant k is directly proportionnal to the slope and is decreasing with the amount of Fetuin-A. Data collected for the system without added protein (blue) is compared to the systems including $1 \mu\text{M}$ (red), $5 \mu\text{M}$ (black) and $15 \mu\text{M}$ (green) of Fetuin-A.

Considering as first step the formation of dicalcium phosphate dihydrate (DCPD), and since the molar ratio used implies more calcium ions, the limiting ion during the formation of the precursor phase is HPO_4^{2-} . Thus, the nucleation is directly proportional to the initial phosphate concentration and to the kinetic constant k of the first order. SAXS intensities at $q=0.25 \text{ nm}^{-1}$ have been followed for each sample at the very early stage of calcification during the first 0.05 second and are displayed in figure 4.5. The constant k is directly proportionnal to the slope of these sets of data. Within the limit of error, it seems evident that Fetuin-A has an influence from the very beginning of the nucleation process: The lower the kinetic constant, the higher amount of the glycoprotein (see figure 4.5).

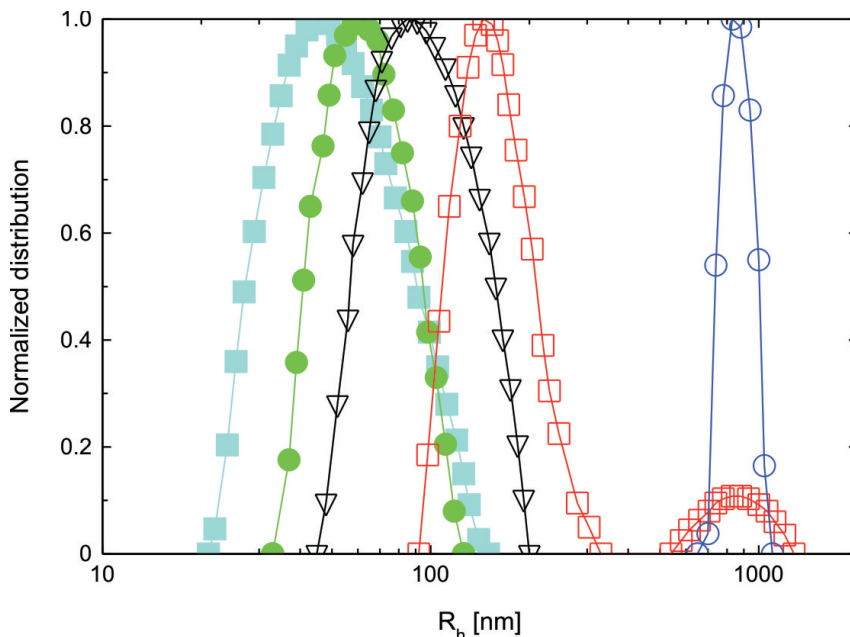


Figure 4.6: Influence of Fetuin-A onto the size of the CPPs. The DLS setup was thermostated at 37°C and 1.8 mL of calcium solution (with the appropriate concentration of Fetuin-A) was inserted in a glass cell. A solution of phosphate ions was as well thermostated at 37°C and 0.2 mL of this solution were inserted in the cell. The solution was then mixed by hand and the DLS measurements started ca. 30 seconds after the mixing process. The final concentration of calcium and phosphate ions was respectively 10 mM and 6 mM. The system without added protein (dark blue) is compared to the ones with $1\ \mu\text{M}$ (red), $5\ \mu\text{M}$ (black), $15\ \mu\text{M}$ (green) and $30\ \mu\text{M}$ (light blue) of Fetuin-A.

4.2.2 Structural effect of Fetuin-A onto the CPPs

In this part, a comparison between the results obtained in reference [17] and the data recorded in presence of different amounts of Fetuin-A from $1\ \mu\text{M}$ up to $15\ \mu\text{M}$, the latter corresponding to a physiological concentration of the protein, will be realized.

Size of CPPs in presence of Fetuin-A

In this paragraph, the ionic concentration of calcium and phosphate are the same than in the work of Heiss [17]. The effect of the overall size of the CPPs have been investigated by using DLS measurements and is presented in figure 4.6 page 33. A drastical change in the size of the particles is observed. None of the experiments involving 10 mM of Ca^{2+} and 6 mM of PO_4^{3-} led to a mean hydrodynamic radius of less than 20 nm.

Table 4.1 presents the different mean value of the hydrodynamic radii obtained when 11.1 mM of calcium and 60 mM of phosphate ions are mixed (volume ratio 9:1 to get a calcium-to-phosphate ratio of 10/6) in presence of different concentrations of the glycoprotein. The sizes reported in this table correspond to the ones once the first equilibrium state is reached, ca. 60 seconds after the mixing process. As expected by the work of Heiss and coworkers [17], there is a decrease of the sizes of the formed particles with the

increase of the concentration of Fetuin-A. Studies about the size of the primary particles is missing in literature. Additional experiments by DLS have been investigated in order to estimate this size.

Single particles

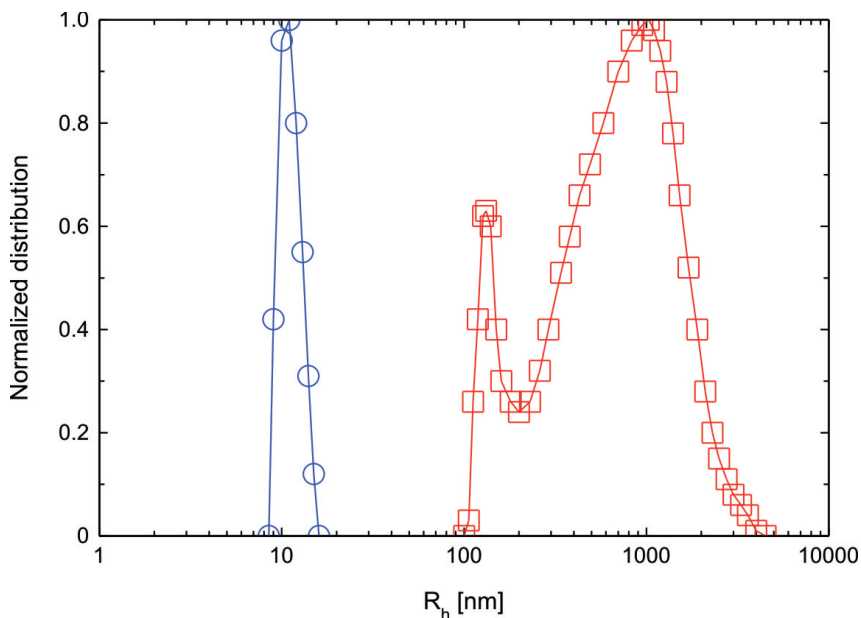


Figure 4.7: DLS measurements of CPPs obtained by mixing 10 mM of Ca^{2+} with 6 mM of PO_4^{3-} . The influence of the addition of 4 μM of Fetuin-A (red) is well highlighted compared to the system without added protein (blue).

In this paragraph, lower concentrations of calcium and phosphate ions have been used but the calcium-to-phosphate-ratio is kept at 10/6.

As previously shown in figure 4.3 page 30, the weight fraction of calcium and phosphate ions have a strong importance onto the aggregation process. Several attempts of DLS measurements were realized by using different amounts of Fetuin-A. As an example, figure 4.7 presents the results of DLS measurements performed by mixing 10 mM of calcium ions with 6 mM of phosphate ions without any glycoprotein and with 4 μM of Fetuin-A.

[Fetuin-A] (μM)	R_H (nm)
0	> 1000
1	150
5	90
15	70
30	45

Table 4.1: Hydrodynamic radius of the particles formed depending on the concentration of the glycoprotein. The mix was realized at 37°C by using solutions of 11.1 mM of calcium (1.8 mL) and 60 mM of phosphate (0.2 mL).

At the exception of the system without any addition of protein, all measurements including 1 μM of FetuinA lead to a mean hydrodynamic radius of ca. 10 nm at room temperature and at 37°C. These results are in agreement with TEM micrographs which were taken at room temperature for the systems without and with 30 μM of Fetuin-A (figure 4.8).

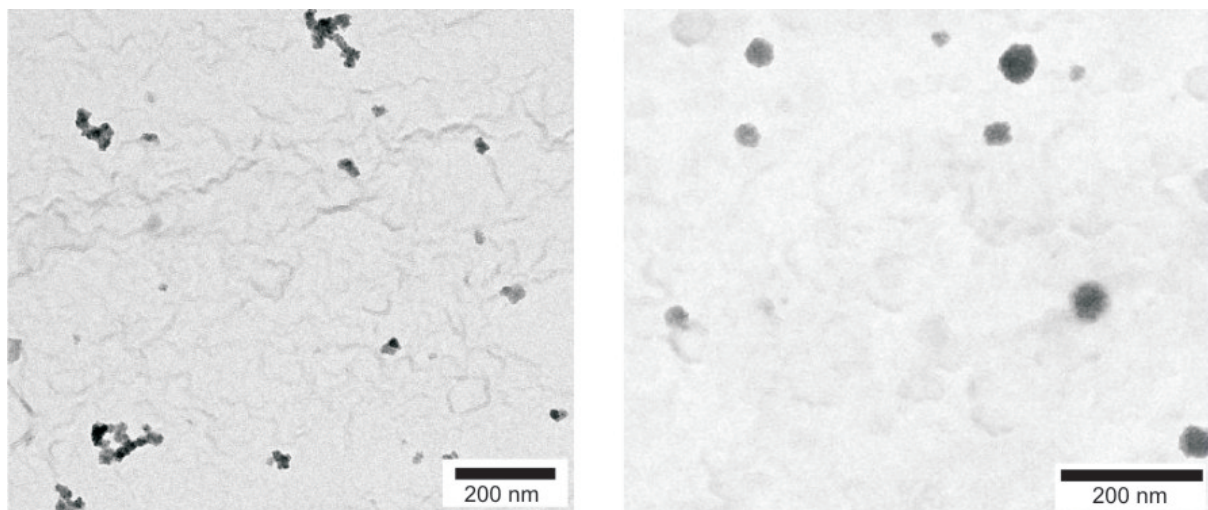


Figure 4.8: TEM micrograph of a sample obtained by mixing 20 mM of Ca^{2+} with 12 mM of HPO_4^{2-} without addition of Fetuin-A (left) and in presence of 15 μM of the glycoprotein (right).

The left part of figure 4.8 presents a TEM micrograph of the system without any addition of Fetuin-A. Aggregates of spherical-like particles are observed. The spherical subparticles have a size of the order of ca. 10 nm and the size of the aggregate is of the order of ca. 50 nanometers. Some aggregates of more than one micrometer were as well observed on other areas of the grid (see in the appendix page 77). The right part of figure 4.8 presents a TEM micrograph of a sample obtained by mixing 20 mM of Ca^{2+} and 12 mM of HPO_4^{2-} in presence of 15 μM of the glycoprotein. The general observation was the presence of single spherical-like particles with a mean size of the order of 10 to 20 nm. A very low number of aggregates of 2 or 3 spherical particles was found. They were suspected to be formed during the blotting of the excess solution by the help of a filter paper.

Quantitative analysis

SAXS experiments have been performed in order to quantitatively study the aggregation process highlighted by the help of DLS and TEM measurements. The top part of figure 4.9 presents the evolution of the scattered intensities of the sample containing no addition of Fetuin-A. A weak minimum around 0.3 nm^{-1} and the absence of oscillation in these intensities are characteristic of the high polydispersity of the system. This is in agreement with both DLS and TEM experiments. Scattering patterns older than 0.26

s did not present any change in the shape or in intensity (measurements realized up to 145 seconds). This demonstrates the very fast kinetic of mineralization of calcium and phosphate ions.

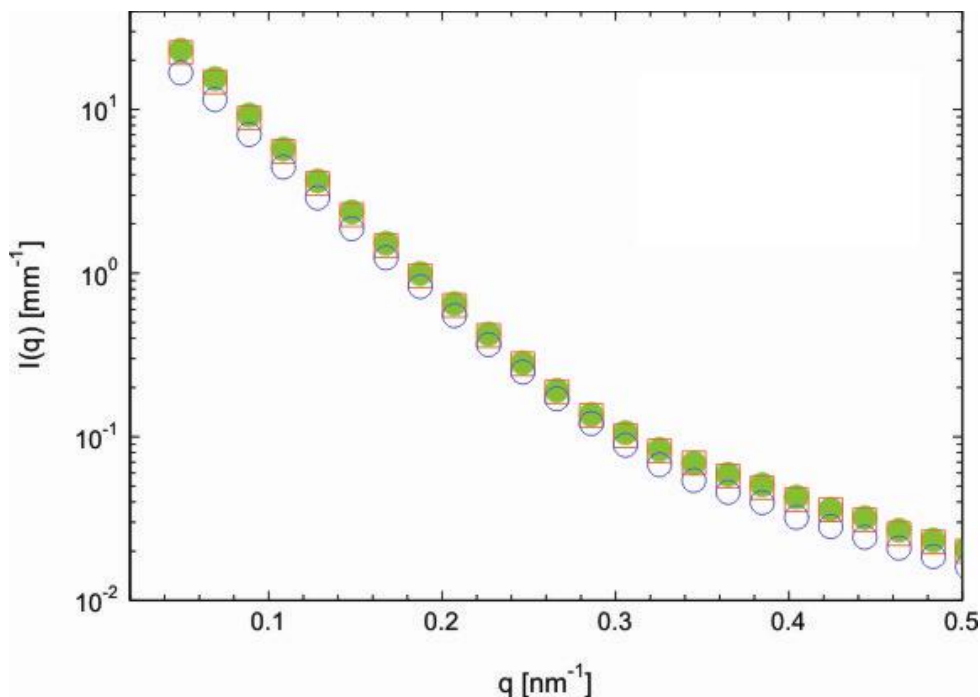


Figure 4.9: Evolution of the SAXS intensities with time in the absence of Fetuin-A. Later SAXS intensities did not show any evolution of the shape or the intensity. This underlines the very fast kinetic of early calcification leading to the first equilibrium phase of calcium phosphate particles. Time point of measurements are: 0.035 s (blue), 0.255 s (red) and 1.355 s (green) after the mixing process.

Measurements realized by adding the glycoprotein gave similar data at q -values bigger than 0.3 nm^{-1} . As an example, the figure 4.10 presents the evolution of the SAXS intensities recorded for the sample containing $15 \mu\text{M}$ of the glycoprotein, that is at physiological concentration. The main difference as compared to figure 4.9 in the trend of the scattered intensities is situated at small q -values. However, it is of course necessary to fit the SAXS intensities in order to get quantitative piece of information for the role of Fetuin-A onto the early stage of calcification.

The fitting procedure was realized by assuming the primary particles as homogenous spheres by using equation 2.6 page 12 as expected from the work of A. Heiss using TEM experiments [64]. The polydispersity in size of the primary particles was taken into account by assuming a normalized Gaussian distribution. Due to the presence of an amorphous system (WAXS measurements in solution were realized and did not show any Bragg peak, see figure B.2 page 79 in appendix), it is necessary to add an additional term to simulate the thermal fluctuations according to the theory of Ornstein-Zernike (see reference [38]). This has been taken into account by the use of the equation 2.12 page 13. The up-turn at small q -values was quantified by the help of the structure factor (equation 2.23 page

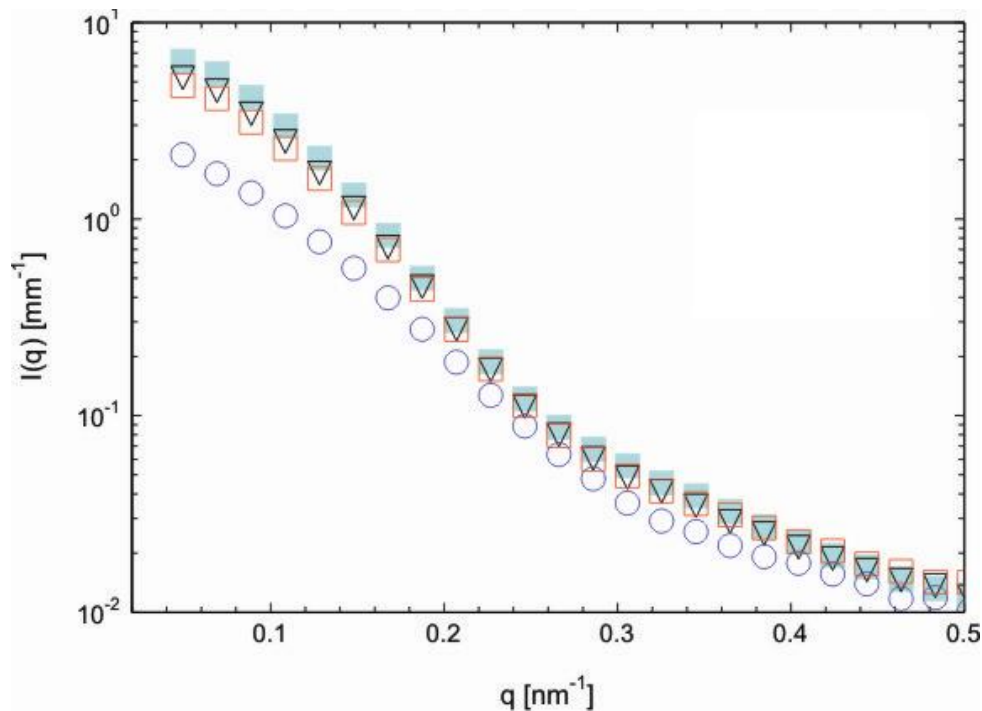


Figure 4.10: Evolution of the SAXS intensities with time in the absence (top) and in presence of $15 \mu\text{M}$ (bottom) of Fetuin-A. Later SAXS intensities did not show any evolution of the shape or the intensity. This demonstrates the very fast kinetic of early calcification leading to the first equilibrium phase of calcium phosphate particles. Time point of measurements are: 0.035 s (blue circles), 0.255 s (red squares), 0.695 s (black triangles) and 6.415 s (blue squares) after the mixing process.

15). The electron contrast of the calcium phosphate complex and of the Fetuin-A are determined respectively to 536 and ca. $50 \text{ e}/\text{nm}^3$. Thus, it is assumed that the scattered intensities is only due to the calcium-phosphate complex. The resulting theoretical equation that has been used in order to fit the experimental scattered intensities $I(q)$ is then:

$$I(q) = \frac{N}{V} (\Delta\rho)^2 V_p^2 S(q) [I_0(q) + I_{fuc}(q)] \quad (4.3)$$

Figure 4.11 presents the scattered intensities collected 0.89 s after the mixing process for all samples studied. No additional structure factor was needed in order to fit the data of the sample involving $15 \mu\text{M}$ of Fetuin-A. Figure 4.12 present the structure factors $S(q)$ resulting from the modelling of the SAXS data recorded 0.89 s after the mixing process. The figure 4.13 presents the evolution of the radius of the primary spherical particles R_{psp} for all studied samples. A very fast kinetic is detected for all studied samples since within one second, the primary particles do not grow anymore. However, this kinetic is too fast to get a quantitative analysis of the growth of the primary particles.

Quantitatively, the different radii of the primary particles are interesting: the higher the concentration of Fetuin-A, the bigger the primary particles. Such a result could not be determined just by the help of DLS or microscopic measurements. The figure

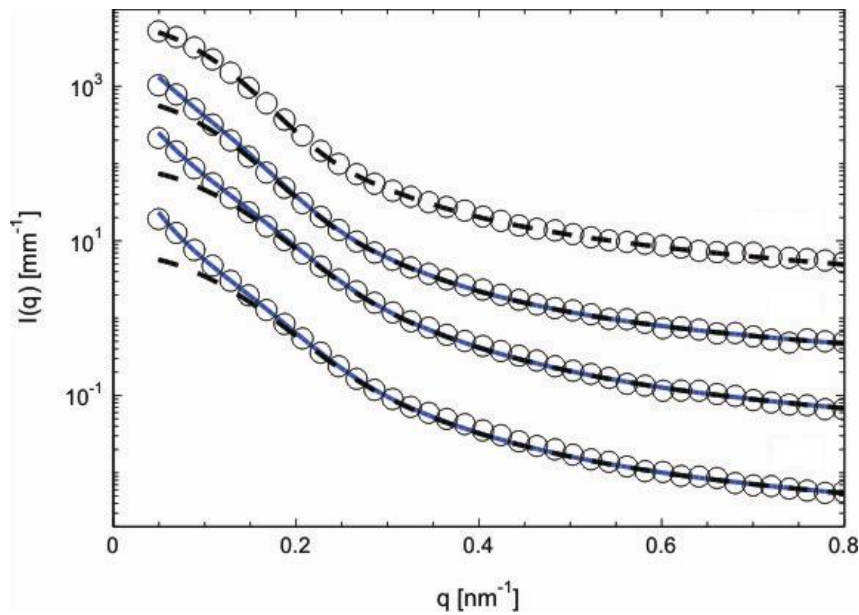


Figure 4.11: Experimental data of measured samples and their respective fits 0.89 second after the mixing process. The points represent the experimental data. For the sake of clarity, only one out of two points is reproduced. The dashed lines exhibit the theoretical fits of polydisperse homogenous non interacting spheres, including the thermal fluctuations and the full lines reflect the complete fit when the structure factor is needed. The graphic shows the different concentrations studied: $0 \mu\text{M}$, $1 \mu\text{M}$, $5 \mu\text{M}$ and $15 \mu\text{M}$ of Fetuin-A from bottom to top.

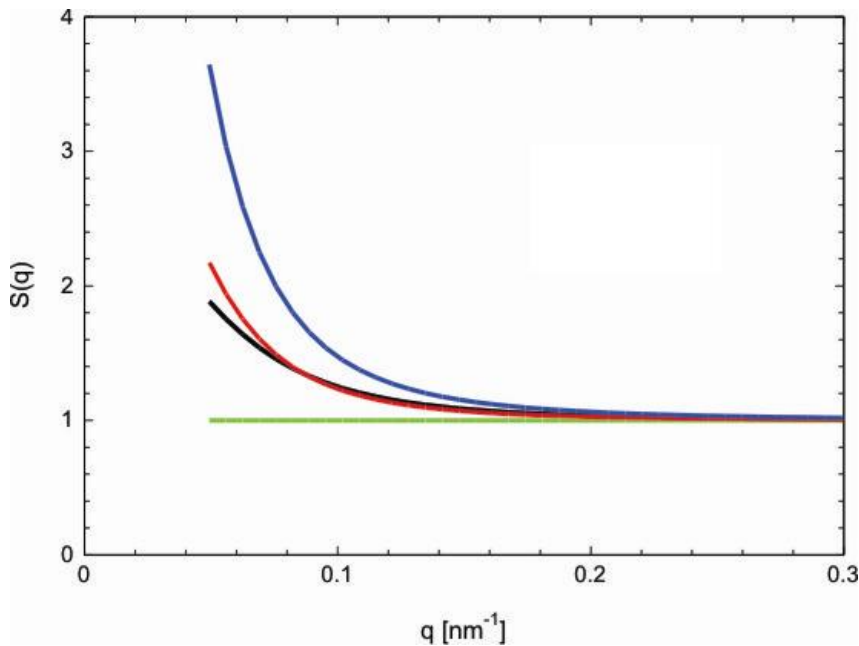


Figure 4.12: Evolution of the structure factor $S(q)$ obtained from the modelling of the SAXS data recorded 0.89 s after the mixing process. The up-turn at small q -values characterizes the aggregation of the nanoparticles. Mixes contain $0 \mu\text{M}$ (blue), $1 \mu\text{M}$ (red), $5 \mu\text{M}$ (black) and $15 \mu\text{M}$ (green) of Fetuin-A.

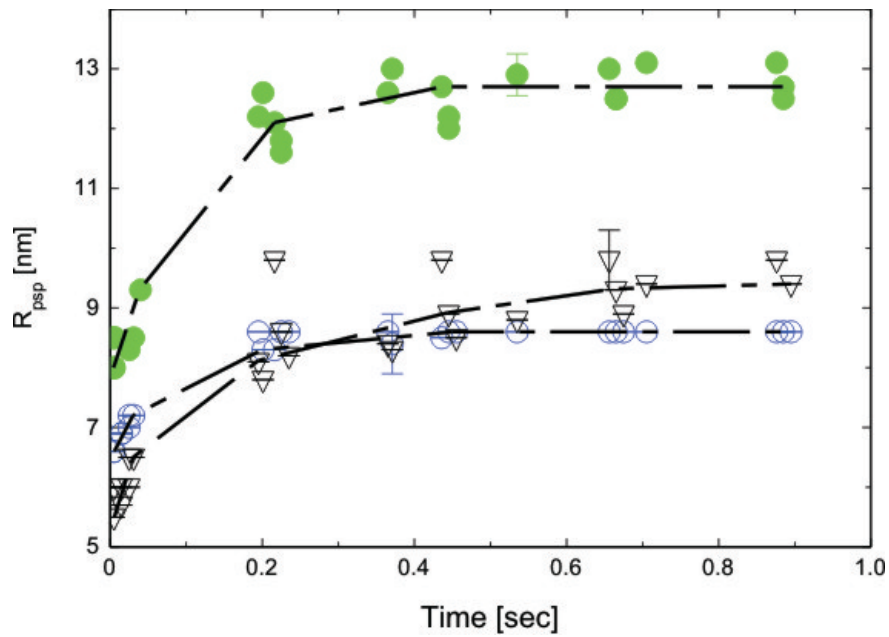


Figure 4.13: Time-evolution of the radius of the primary spherical particles of calcium phosphate as a function of the concentration of the protein. The primary spherical particles grow with a very fast kinetic within 1 s for all samples studied. The dashed lines are guide lines for the evolution of the radius of the primary spherical particles. Data involving a concentration of $1 \mu\text{M}$ of Fetuin-A are not reproduced for the sake of clarity and is intermediate to the one of 0 and $5 \mu\text{M}$.

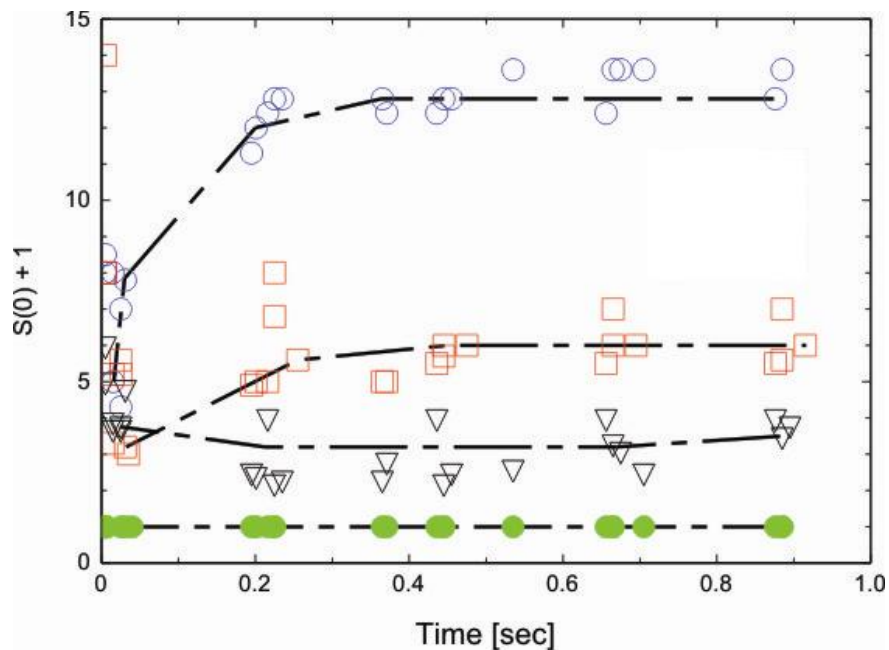


Figure 4.14: Time-evolution of the number of primary spherical particles per aggregate ($S(0)+1$). The main effect of Fetuin-A is seen here: inhibition of the aggregation. The dashed lines are guide lines for the evolution of the parameters. Mixes contain $0 \mu\text{M}$ (blue), $1 \mu\text{M}$ (red), $5 \mu\text{M}$ (black) and $15 \mu\text{M}$ (green) of Fetuin-A.

4.14 presents the time-evolution of the number of primary particles per aggregate. This plot permits to better understand the role of Fetuin-A onto the calcification at early stage. As demonstrated by figures 4.11 and 4.12, there were no need to simulate any interparticle interactions in order to fit the system involving a physiological concentration of the protein (15 μM). The results obtained from the other studied concentrations of the glycoprotein show that the lower the amount of Fetuin-A, the bigger the number of particles per aggregate. This is the proof that α_2 -HS-glycoprotein/Fetuin-A is inhibiting the aggregation of the primary spherical particles of calcium phosphate and is stabilising these particles from the earliest stage of mineralization.

According to the results found in this study and to previous work in literature [17], an hypothetical model of the formation of calcium phosphate particles induced by the presence of Fetuin-A could be described as follow: During the nucleation process, Fetuin-A has a weak effect until the primary particles grow to ca. 10 nm in radius. Once the nucleation process is ended, Fetuin-A may cover the calcium-phosphate particles and act as a shield to prevent aggregation. According to Heiss [64], the glycoprotein interacts with 6 different calcium ions (see figure 4.15), which is probably the way for the protein to create a layer of itself onto the calcified particles.

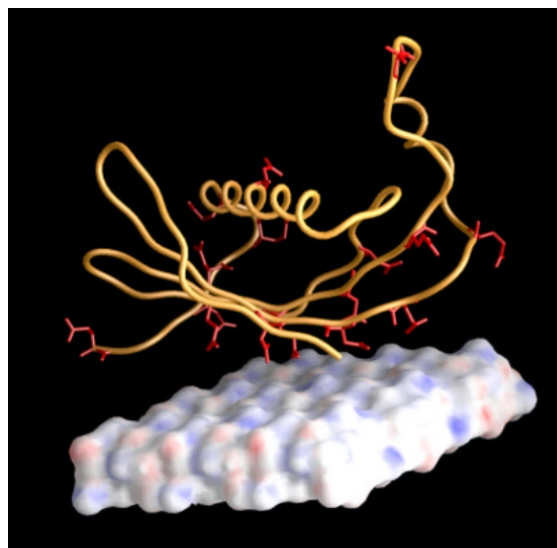


Figure 4.15: Binding of the D1 domain of Fetuin-A onto the surface of hydroxyapatite. The positive charges of Ca^{2+} are marked in blue and the negative phosphate charges are represented in red. Figure taken from reference [63].

Chapter 5

Polybutadiene

5.1 Experimental

The syndiotactic 1,2-poly(1,3-butadiene) sample was synthesized and provided by Dr. Brigitte Korthals from the group of Proff Mecking, Konstanz. The synthesis of these nanoparticles (named BK280) could be found in the appendix page 86. The received system contained 5.05 wt% of SPBD and 6.99 wt% of SDS to avoid further aggregation. The molecular weight was determined in Konstanz to 1.4×10^5 g/mol. Before the addition of the surfactant, X-ray diffraction has been realized and showed peaks of crystalline sPB as presented in the appendix page 87.

Dynamic Light Scattering measurements were performed at 25°C as explained page 59. Diluted samples (0.00013 wt%) were analyzed from 30 to 150°. Figure B.1 page 88 in the appendix presents the decay rate Γ as a function of the square of the scattering vector q . The diffusion coefficient is determined by the slope of these data and then the hydrodynamic radius of these nanoparticles was determined by the help of the Stoke-Einstein equation (see page 59). A value of 6.4 nm was obtained which is in agreement with the value determined by our collaborators in Konstanz ($R_h = 7$ nm).

Specimens for cryo-TEM experiments were prepared by vitrification of a thin liquid film of the diluted dispersion (0.03 wt%) supported by a copper grid in liquid ethane. Each sample was inserted into a cryo-transfer holder (CT 3500, Gatan, Munich, Germany) and transferred to a Zeiss EM 922 EFTEM (Zeiss NTS GmbH, Oberkochen, Germany). Examination was carried at -183°C at a pressure of 10^{-7} - 10^{-8} hPa. No staining agent was used to enhance the contrast between the particle and the surrounding medium. Hence, the particles were analyzed in situ.

5.2 Theoretical modeling

SAXS experiments were performed in Bayreuth by using a Kratky Compact Camera at room temperature. For each sample, the signal of the empty capillary and of the solvent alone was subtracted to the one of the system dispersed in the solvent according to the volume fraction of the nanoparticles. For a system consisting of monodisperse PE nanoparticles, the scattering intensity $I_0(q)$ of a particle could be written as:

$$I_0(q) = S(q)[I_{sPB}(q) + I_{fluc}(q)] \quad (5.1)$$

where $S(q)$ is the structure factor describing the interparticle interaction, I_{sPB} is the form factor of the polybutadiene particles alone (see below) and $I_{fluc}(q)$ arises from density fluctuations inside the particle (see equation 2.12 page 13). $I_{fluc}(q)$ contribute mainly at high magnitude of the scattering vector.

Different models have been investigated so as to fit the experimental data (see schematic models and their respective corresponding theoretical SAXS intensities in appendix page 89). The presence of a higher amount of SDS as compared to the one studied in reference [33] implies the presence of two additional layers of SDS. The best results were obtained by using the following model: a crystalline layer of sPB sandwiched between two layers of amorphous polymers sheets and finally two additional layers of SDS as presented in figure 5.1. The scattered intensity $I_{sPB}(q)$ of the sPB nanoparticle was calculated (see program in the appendix) according to the following equations:

$$I_{sPB}(q) = \frac{N}{V} \int_0^{\pi/2} [F_{disk}(q, \alpha)]^2 \sin(\alpha) d\alpha \quad (5.2)$$

$$F_{sPB}(q, \alpha) = 2\pi R^2 \frac{2J_1(qR \sin(\alpha))}{qR \sin(\alpha)} \left\{ \begin{array}{l} \frac{\sin(qL_t \cos(\alpha)/2)}{q \cos(\alpha)/2} (\rho_{sds} - \rho_{sol}) + \\ \frac{\sin(qL \cos(\alpha)/2)}{q \cos(\alpha)/2} (\rho_{amo} - \rho_{sds}) + \\ \frac{\sin(qL_c \cos(\alpha)/2)}{q \cos(\alpha)/2} (\rho_{cry} - \rho_{amo}) \end{array} \right\} \quad (5.3)$$

where ρ describes the electron density distribution, and the indexes sol, sds, amo and cry represent the solvent, the SDS surfactant, the amorphous and the crystalline phase of the polymer. L_t , L and L_c represent the overall thickness of the particle, of the polymer and of the crystalline phase and R is the radius of the disc. $J_1(x)$ is the cylindrical Bessel function of first order. A sketch of the model is represented in figure 5.1. $\frac{N}{V}$ is the number of particles per volume. The size polydispersity was taken into account by using Gaus-

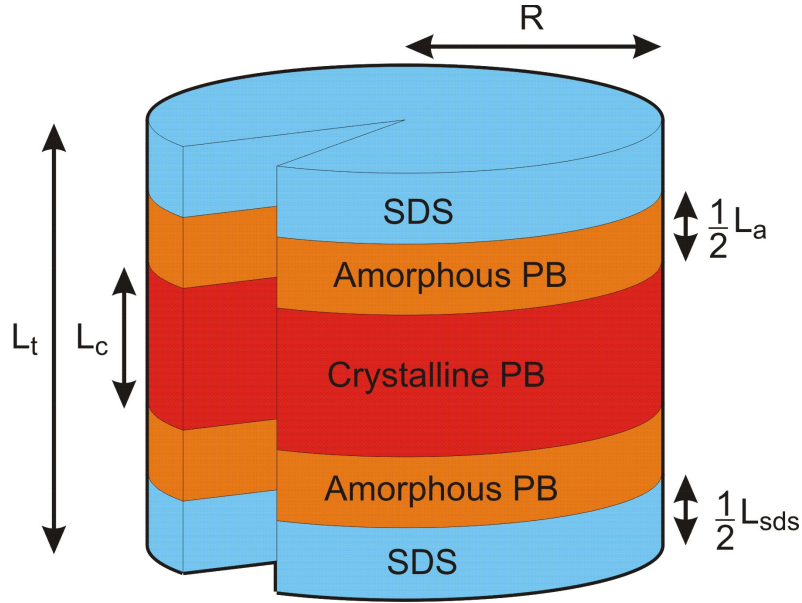


Figure 5.1: Hamburger model used in this study. Two additional sheets of SDS have to be taken into account to model the structure. L_t , $L=L_c+L_a$ and L_c represent the thicknesses of the whole particle, of the polymer and of the crystalline phase respectively, while R is the radius of the disk.

sian distributions for the radius R , the crystalline thickness L_c and the amorphous layer L_a .

From the model parameters and by taking into account the electron contrasts (ρ_{cry} and ρ_{amo}) and the molecular weight M_W of the polymer chains ($M_W=1.4 \times 10^5$ g/mol), the number of polymer chains n_{chains} per particle could be determined:

$$n_{chains} = \pi R^2 \frac{\rho_{amo} L_a + \rho_{cry} L_c}{n_e(C_4H_6)} \times M_W(C_4H_6) \quad (5.4)$$

where $n_e(C_4H_6)$ and $M_W(C_4H_6)$ are respectively the number of electrons and the molecular weight of C_4H_6 (monomer of sPB).

5.3 Results and Discussions

5.3.1 Cryo-TEM

Figure 5.2 presents the typical morphologies observed for these nanoparticles of polybutadiene. The darker small regions exhibit well-defined single nanoparticles while the lighter background is the solvent. A comparison with the morphology of the PE nanoparticles observed by the help of cryo-TEM experiments in the literature [33] could be realized: The morphology exhibited by these nanoparticles is typical of disks. When the main axis of the platelet is perpendicular to the electron beam, the particle appears as light hexagon (see inset in the top-right of figure 5.2). At the opposite, when the main

axis of the platelet is parallel to the electron beam, the particle appears as dark rod (see inset bottom-left in figure 5.2) in which the thickness measures ca. 5 nm. However, and as expected by the DLS experiments ($R_h = 6.4$ nm), the overall size of the polybutadiene nanoparticles is slightly smaller than in the work of Weber [33].

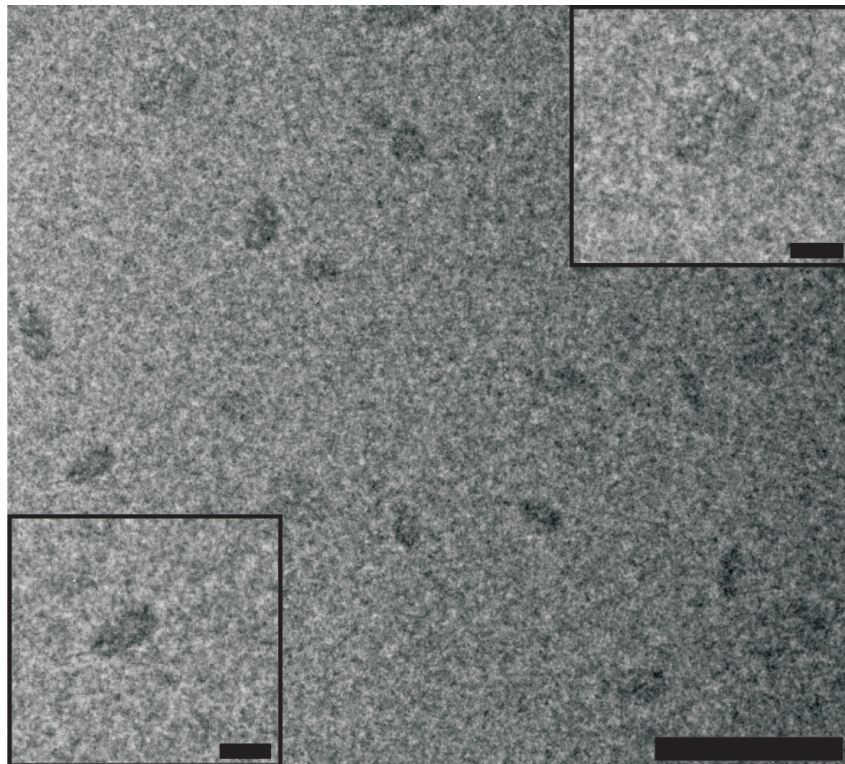


Figure 5.2: Cryo-TEM image of the nanoparticle of polybutadiene. The concentration was 0.03 wt%. The scale bar of the main micrograph represents 50 nm while the ones in the insets represent 10 nm.

5.3.2 SAXS

The inner structure of these particles has been evaluated by a SAXS contrast variation study. Different amounts of D⁺-glucose were added in the aqueous solution. The blue circles data points in figure 5.3 presents the SAXS intensities of the polybutadiene system in water. We note a pronounced minimum around 0.8 nm^{-1} and a maximum at ca. 1.1 nm^{-1} . These oscillations are characteristic of a structurally ordered system. The nanoparticles in the cryo-TEM picture in figure 5.2 may then be interpreted as thin disks such as the ones in reference [33]. In order to better interpret the inner structure of this PB system, SAXS experiments have been performed by using the contrast variation method. For the purpose, equations 5.1 to 5.3 page 42 were used to model the SAXS experimental intensities.

System	BK280
R [nm]	4.5 ± 1.5
L_c [nm]	4.8 ± 1.6
L_a [nm]	2.8 ± 1.1

Table 5.1: Parameters obtained from the fits of the SAXS-CV data. Indexes c and a define the crystalline and the amorphous phases. L denotes one layer.

Figure 5.3 presents the scattering intensities of the syndiotactic polybutadiene system measured in solvents of different contrasts. We note a small shift of the oscillation to smaller q -values as well as an increase of the overall slope of the scattering intensity with the increase of the D^+ -glucose. From bottom to top, the concentration of glucose (and of the sample) in solution was 0.0 (1.2), 3.2 (1.2), 6.5 (1.2), 9.8 (1.2) and 17.3 (1.3) vol%. The solid lines represent the result of the non-interacting polydisperse disks. The parameters used are reported in table 5.1. The electron densities of the crystalline, amorphous and SDS parts were respectively 322 e.u./nm^3 , 280 e.u./nm^3 and 376 e.u./nm^3 . The theoretical intensities involving the interparticles interactions have not been calculated since this study focused on the intraparticle interactions. However, we note that the down-turn at low q -values is far less pronounced as compared to the PE system studied in literature [33]. This could be explained by the dimensions of the overall mean particle: the diameter (9 nm) is of the order of the overall thickness of the mean nanoparticle (10.2 nm).

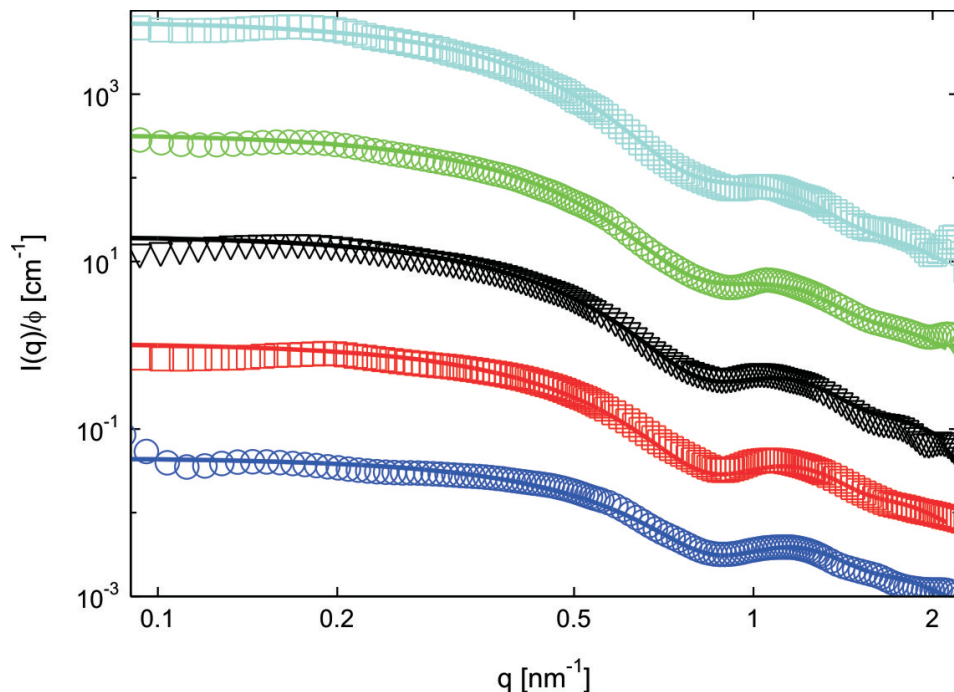


Figure 5.3: Normalized scattering intensities of the polybutadiene nanoparticles. For the sake of clarity, the four lowermost scattered intensities were divided by factor of 10^1 , 10^2 , 10^3 and 10^4 . From bottom to top, the concentration of glucose (and of the sample) in solution was 0.0 (1.19), 3.2 (1.23), 6.5 (1.24), 9.8 (1.24) and 17.3 (1.32) vol%.

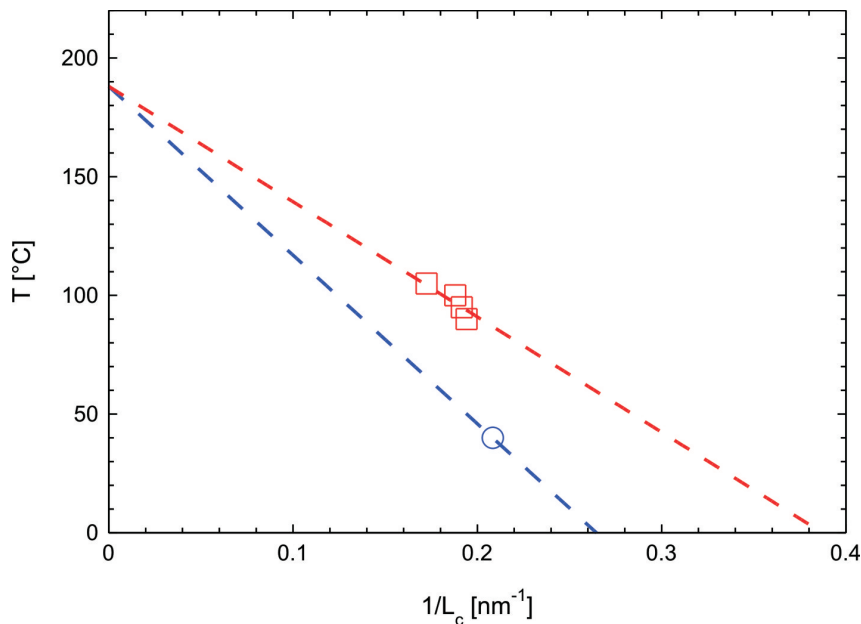


Figure 5.4: Plot of the temperature as a function of the reciprocal of the crystalline thickness of syndiotactic polybutadiene systems. The red squares are obtained from reference [119] and the blue circle represents this study. The bold red and blue lines are guide-lines for the recrystallization and crystallization lines respectively.

5.4 Conclusion

The structural morphology of syndiotactic polybutadiene nanoparticles has been studied. The combination of cryo-TEM together with SAXS experiments permit to determine the hamburger model of these nanoparticles. They exhibit a mean crystalline thickness of ca. 5 nm. Zhang and coworkers [119] analyzed the structure of semi-crystalline syndiotactic polybutadiene bulk obtained from melt by the combination of Synchrotron SAXS and WAXS. They especially determined the crystalline thickness of annealed samples and plotted the reciprocal of the crystalline thickness as a function of the annealing temperature as reproduced in figure 5.4. The coordinates of the blue circle ($1/L_c, T_{syn}$) where T_{syn} is the temperature of the synthesis of the system, is determined with the parameters obtained from the fitting procedure of the SAXS studies in this report. This point is below the red bold line representing the recrystallization line according to the data points measured in reference [119]. Both bold lines (the blue representing the crystallization line) cross each other at an infinite crystalline thickness as proposed by Strobl [29]. According to Zhang et al. (reference [119]), the crystallization temperature of an infinitively big syndiotactic polybutadiene is around 188°C (temperature reported in figure 5.4). Evidently, additional experimental points of coordinates ($1/L_c, T_{syn}$) are needed in order to better estimate the crystallization and recrystallization lines of polybutadiene.

During the fitting procedure of the experimental SAXS data, the electron contrast

of the different phases (crystalline, amorphous sPB and SDS) were let free. The best theoretical intensities were achieved with an electron density of the crystalline layer corresponding to a weight density of 0.962 g/cm^3 . This value is, according to Natta [83], the weight density of crystalline sPB. The electron density of the surfactant's phase (SDS) was of the same order as the one determined for the polyethylene study (see next chapter). This underlines and confirms the veracity of the results obtained. The number of polymer chain per particle has been as well determined by the help of equation 5.4 page 43 and it resulted to only two polymer chains which is drastically lower than for the PE system studied in reference [33] where an average of 14 polymer chains were constituting each nanoparticle.

Chapter 6

Polyethylene

6.1 Experimental

For this study (collaboration with Dr. Qiong Tong from the group of Proff Mecking, Konstanz), two different PE systems PL39 and PL78 were investigated due to the limited amount of each sample. The samples PL39 and PL78 contain 1.7 wt% and 1.6 wt% PE, respectively. The surfactant sodium dodecyl sulfate (SDS) is needed to stabilize the PE particles against coagulation. The weight fractions of SDS are 0.87 wt% for PL39 and 0.36 wt% for PL78. Hence, the amount of SDS in PL39 has been increased as compared to the previous study [33]. The PE systems differ in the labile ligand of the catalyst used during the synthesis (TPPTS for PL39, NH₂-PEG for PL78, see additional piece of information in the appendix page 80). The longer lifetime of the catalyst with the NH₂-PEG ligand results in the different amount of SDS during synthesis. This does not have a significant influence on either the molecular weight or in molecular structure of the obtained PE chains.

Annealed samples were produced by placing a 5 mL glass bottle containing the original system onto a metal box heated at the annealed temperature for 20 minutes. PE nanoparticles annealed for longer time (up to 60 minutes) did not reveal any further increase of the thickness of the crystal. The annealed systems were slightly more concentrated since evaporation could not be completely avoided.

Dynamic Light Scattering measurements were performed with an ALV/DLS/SLS-5000 compact goniometer system (ALV Langer) equipped with a He-Ne laser (632.8 nm) and a thermostat (Rotilabo, $\pm 0.1^\circ\text{C}$) at 25°C . Diluted samples (0.0013 wt%) were analyzed from 30 to 80° . According to the Stoke-Einstein equation, the hydrodynamic radius of each sample was determined respectively to 11.2 ± 0.2 nm and 11.4 ± 0.2 nm for the original and annealed sample. These light scattering experiments did not permit to detect any

difference before and after the annealing process. In order to have a better understanding of the morphology of the particles studied, cryogenic transmission electron microscopy experiments have been performed.

6.2 Results and discussion

6.2.1 Cryo-TEM

Specimens for cryo-TEM experiments were prepared at room temperature as explained on page 42. The concentration used here was higher by a factor of 10 leading to 0.3 wt%. Figure 6.1 presents typical overviews of the cryo-TEM micrographs recorded of the

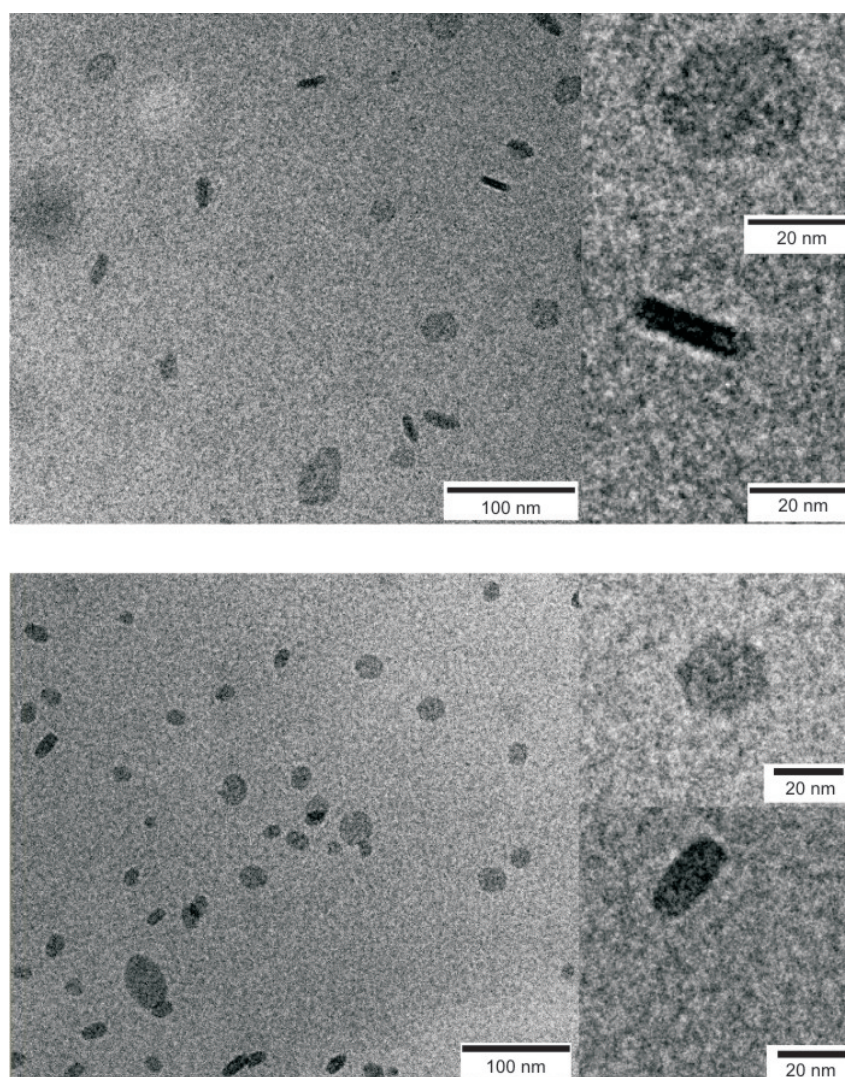


Figure 6.1: Typical cryo-TEM micrographs of the original PL39 system (top) and of the annealed PL39 sample (bottom). Insets in each micrograph presents a single particle in which the direction of the main axis is orthogonal and parallel to the direction of the electron beam. The annealing process was carried at 125°C for 20 minutes. For both micrographs, the weight percentage studied is 0.3 wt%.

original system (top) and of the annealed one (bottom). These particles are well dispersed in the solution. Different morphologies could be remarked and this comes from the angle between the main axis of the particle and the one of the electron beam. The difference of contrast between one particle and another is related to different angles between the normal of the platelets and the direction of the electron beam. This is more pronounced in the top-inset where the main axis of a single particle is parallel to the electron beam. Such particles appear as dark rods. At the opposite, the bottom-inset present a single particle in which the main axis is orthogonal to the direction of the beam. These particles appear as lighter hexagons. This hexagonal shape agrees well with the theoretical growth of PE nanoparticles (figure 3.6). The annealed nanoparticles (bottom micrograph in figure 6.1) present the same morphology as shown in the inset. However, a change appeared in the dimensions (radius and thickness) of the system. Derived from the image analysis of 20 particles with their normal oriented perpendicular to the electron beam, the height of the platelets was determined to 7 ± 1 nm before and 13 ± 2 nm after annealing and the platelet radii decreased from 14 ± 4 nm to 9 ± 2 nm respectively. One has to take into account that it is not possible to detect the amorphous layer of these PE nanoparticles because its electron density is very similar to the one of the surrounding medium (low density amorphous ice, [33]; light gray in the background represents the low density amorphous ice). In order to elucidate the shape and structure of the PE particles in more details, the systems have been investigated using SAXS and contrast variation technique.

6.2.2 SAXS

SAXS experiments were performed at the ID02 beamline at ESRF, Grenoble, France and in Bayreuth by using a Kratky Compact Camera. Figure 6.2 presents the scattered intensities of the PL39 PE nanoparticles before (top) and after (bottom) the annealing process. The volume fraction of the contrast agent varies from 0% (blue points), 4% (red points), 10% (black points) up to 14% (green points), while the volume fraction of the nanoparticles decrease: 2.5, 2.4, 2.3, 2.2 vol% for the original system (top) and 2.6, 2.5, 2.3 and 2.2 vol% for the annealed sample (bottom) respectively. The three lowermost intensities are divided by factors of 10, 10^2 and 10^3 for sake of clarity. The theoretical SAXS intensities have been modelled by using equations 5.1 to 5.3 and are presented in figure 6.2. The solid lines represent the result of the non-interacting polydisperse disks. The short dashed lines ($q < 0.14 \text{ nm}^{-1}$) are obtained using the PRISM integral theory. PRISM theory is well known to account for interactions of anisotropic particles and surface charges. The difference between the dashed and the solid lines reflect the intermolecular interactions between the nanoparticles. The modelling including the interparticle interaction was realized by Priv.-Doz. Dr. Ludger Harnau.

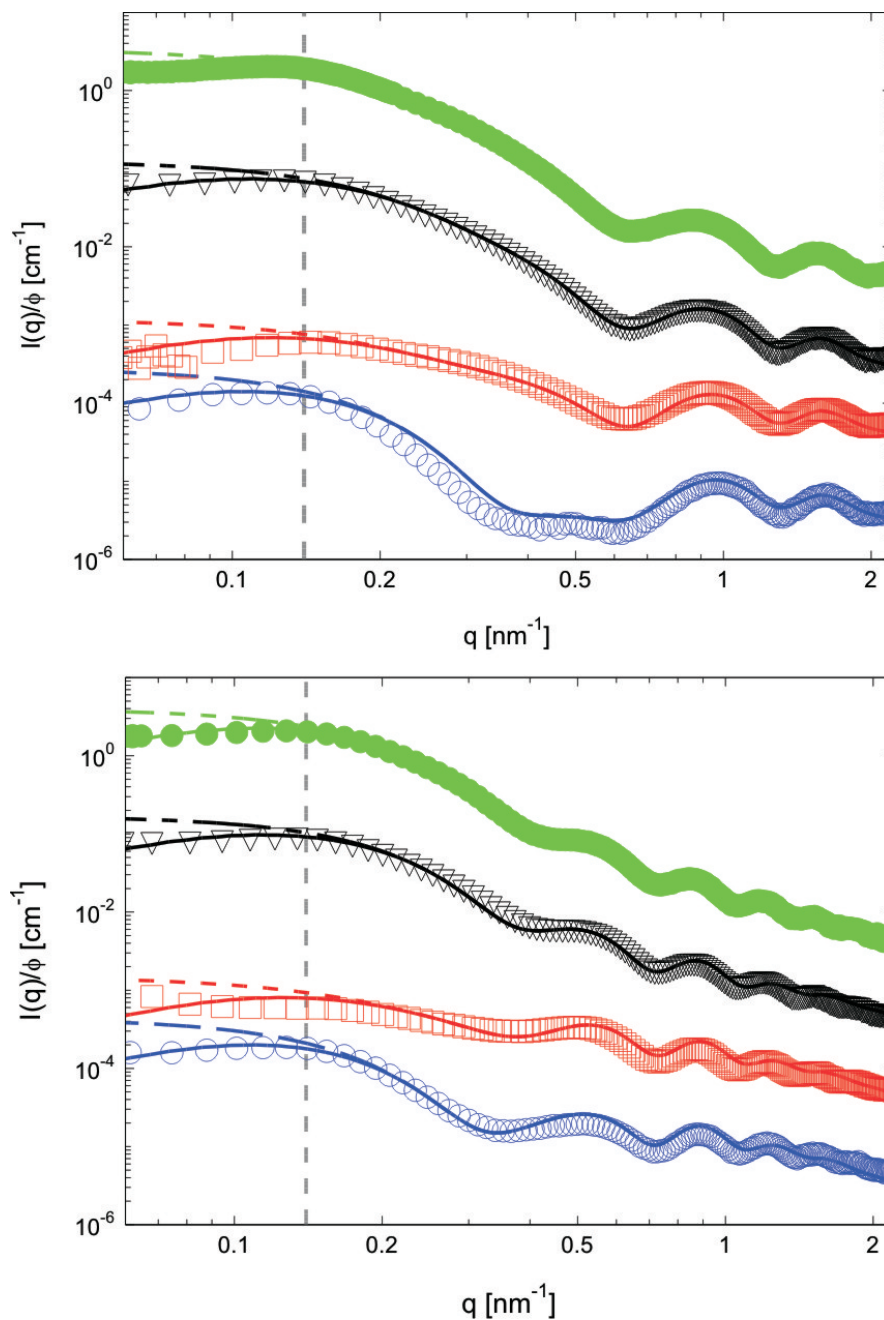


Figure 6.2: Normalized scattered intensities of the PL39 PE system before (top) and after (bottom) the annealing procedure. All intensities are normalized by the volume fraction of the sample. The volume fraction of the contrast agent varies from 0 (blue points), 0.04 (red points), 0.10 (black points) up to 0.14 (green points), while the volume fraction of the nanoparticles decrease: 2.5, 2.4, 2.3, 2.2 vol% for the original system (top) and 2.6, 2.5, 2.3 and 2.2 vol% for the annealed sample (bottom) respectively. The three lowermost intensities are divided by factors of 10, 10^2 and 10^3 for sake of clarity. The vertical gray dashed lines show the q -value below which the structure factor is needed. For the sake of clarity, only one out of 5 points is shown. The dashed lines represents the result of the modeling of the SAXS data assuming a dispersion of non-interacting polydisperse platelets. The solid lines represent the scattering intensity calculated for a dispersion of interacting polydisperse platelets.

Evidently, and as expected by the cryo-TEM micrographs (figure 6.1), the annealing process changed the structure of the original system. There are more oscillations in the scattered intensities of the annealed system than in the one of the original PE nanoplatelets (see figure 6.2). One can note that the structure factor $S(q)$ intervene only at long distances, i.e. small magnitudes of the scattering vector q , below 0.14 nm^{-1} . This defines the average distance d between two particles with the equation $d = 2\pi/q = 45 \text{ nm}$. This value remains constant before and after the annealing process. This demonstrates that the number of particles per volume is constant, thus no fusion of the particles occur during the annealing process. This is further confirmed by the fact that $I(q=0)/[\phi(\Delta\rho)^2]$ is constant for the original and annealed system (see figure B.4 in the appendix page 81).

The change of the morphology of the nanoplatelets can directly be seen by the SAXS data: the location of the side maxima and minima shift to lower q values after annealing.

System	Original	Annealed
R [nm]	10.0 ± 3.0	7.5 ± 3.0
L_c [nm]	6.5 ± 1.0	13.0 ± 1.0
L_a [nm]	3.1 ± 0.8	3.8 ± 1.0

Table 6.1: Parameters obtained from adapting equations 5.1 to 5.3 to the experimental data. L_c and L_a define the overall crystalline and amorphous thickness of the particle.

Table 6.1 resumes the parameters obtained by adjusting equations 5.1 to 5.3 to the experimental data of the original and annealed system (see figure 6.2). The thickness of the crystalline layer increases by a factor of 2 (from 6.5 to 13 nm respectively for the original and annealed system). The thickness of the amorphous layer remains nearly constant (respectively 3.1 nm and 3.8 nm). Within the limit of error, the radius decreases from 10 nm to 7.5 nm. By using a Gaussian polydispersity during the fitting of the SAXS data, the average number of polymer chain n_{chains} has been determined according to equation 5.4 ($\rho_{cri}=339 \text{ e.u./nm}^3$ and $\rho_{amo}=302 \text{ e.u./nm}^3$). This average number of polymer chains was determined to $n_{chains}=8$ before and after the annealing process.

The combination of the cryo-TEM experiments and of the SAXS contrast variation data permit to demonstrate that annealing the sample PL39 at 125°C for 20 minutes leads to a doubling of the crystalline thickness (6.5 nm to 13 nm). In the literature, two scenarios of the thickening process are proposed. The first one is an unlooping of the polymer chains within one crystalline platelet (figure 6.3 (a), references [120,121]). Increasing the temperature leads to an increase of the chain mobility and to cooperative motion of the monomer units. This hypothesis leads to a surface of the crystalline phase divided by two as compared to the original system and to the same number of particles. The second model

explains the thickening by the stacking of two adjacent crystalline layers into one of the same surface and double thickness (figure 6.3 (b) and references [106,122]). Such a model is valid for systems in which the crystalline phases are connected by amorphous regions and lead to a number of particles divided by two. From the fitting parameters, there is a doubling of the thickness of the crystalline phase. Moreover, the number of particles per volume remains constant before and after the annealing process. This behaviour is characteristic of the unlooping model proposed by references [120,121]. Thus model (b) in figure 6.3 is ruled out.

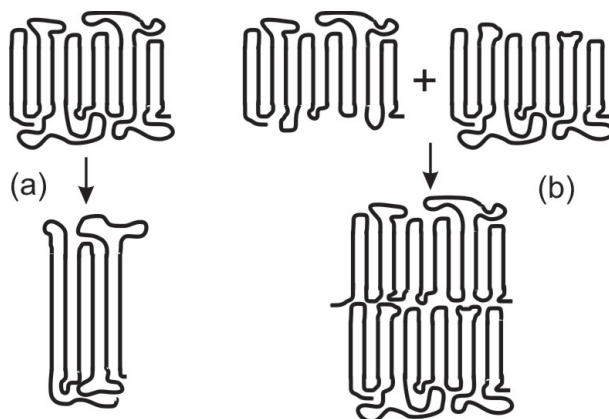


Figure 6.3: 2D-model of the unlooping process expected by some authors [106,120–122]. (a): The full unlooping process of one single crystalline nanoparticle lead to a doubling of the crystalline thickness of the same particle. (b): The stack of two crystalline particles lead to one particle with a doubled crystalline thickness.

6.3 Variation of annealing temperature

The study of the effect of the annealing process has been presented in the previous section. Well-defined nanoparticles of polyethylene have been subject to a thermic treatment for 20 minutes at 125°C, that is just below the melting temperature $T_m=128^\circ\text{C}$ according to DSC measurements. The last section demonstrated that, during the annealing process, no fusion occurs and a simple unfolding of the crystalline chains is responsible of the doubling of the crystalline thickness. The PE nanoparticles are then particularly interesting to better understand the annealing process of PE crystalline phase. These experiments have been pushed forward by varying the annealing temperature to lower temperatures. The annealing process was carried at 90°C, 105°C and 115°C for 20 minutes by using the sample PL78 due to the lack of sample PL39. Cryo-TEM experiments have been performed onto these samples by using the same setup as the system PL39 and the growth of the overall thickness is highlighted (see figure 6.4). A very broad polydispersity over the radius of the particles is observed as expected by the synthesis (use of a catalyst leading to a longer lifetime and stronger polydispersity, see appendix). Thus, cryo-TEM

micrographs only permit to insure that the nanoparticles are well-defined.

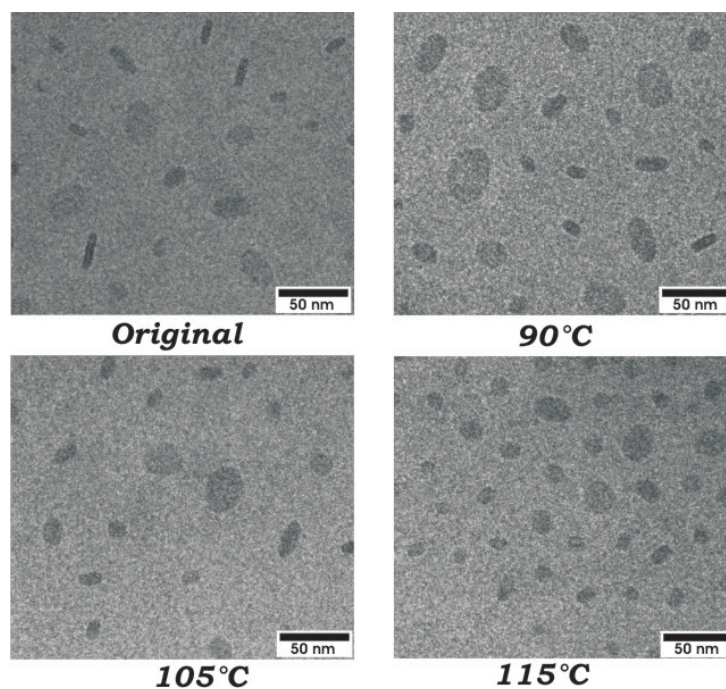


Figure 6.4: Cryo-TEM micrographs of PL78 sample (original and different annealed temperatures). The black bar represents 50 nm.

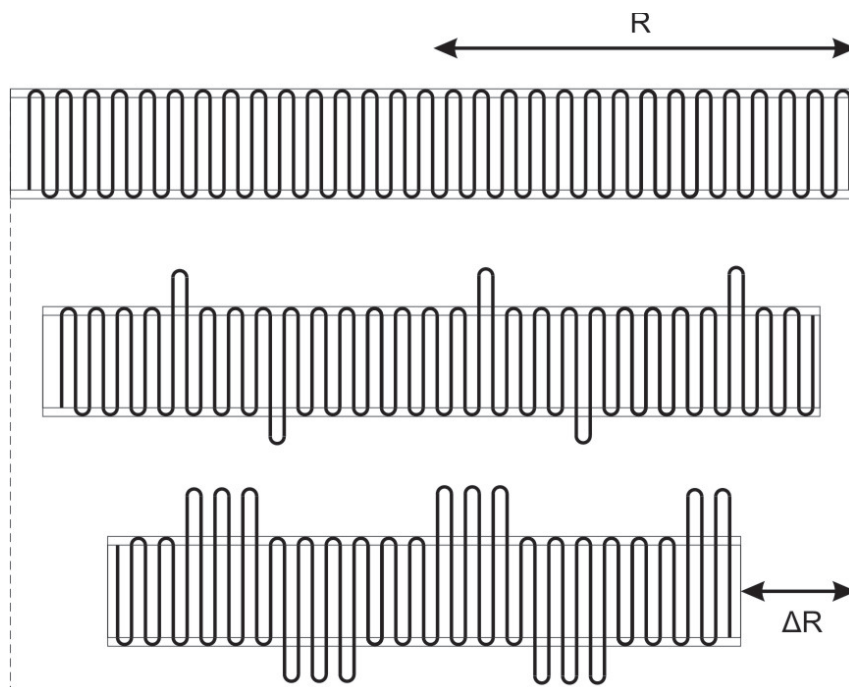


Figure 6.5: Two-dimensional schematical representation of partial unlooping of PE chains within a nanoparticle. A partial unlooping leads to a very small decrease of the radius R of the platelet, probably a decrease too small to be detected by SAXS experiments.

However, it seems evident that the thickness of the crystalline phase increases with

the annealing temperature as expected. Because of these very small dimensions and this high polydispersity, the resolution of the SAXS experiments do not allow to determine precisely these radii. In the previous section, for the system PL39, the nanoparticles were fully annealed (the thickness of the crystalline phase fully doubled). Due to partial annealing, it is impossible to determine the precise location and amount of unlooped PE chains (figure 6.5). In combination with the given polydispersity of radius R and the limited resolution of SAXS, the exact determination of the radius is impossible. Thus, for this system, a radius of 6 nm was kept constant during fitting routine. Nevertheless, it is still kept in mind that the number of particles per volume is constant and that the radius of each particle must slightly decrease with the annealing temperature.

SAXS measurements have been performed by the same approach than for the PL39 system. Figure 6.6 presents the experimental data of the samples PL78 in water and their corresponding fits according to equations 5.1, 5.2 and 5.3 including the interparticular interactions given by $S(q)$. The differences between the measured scattering intensities of the original sample PL39 (lower symbol in the top graphic of figure 6.2) and the original sample PL78 (lower symbols in figure 6.6) is due to the different amount of SDS added. Crystalline thicknesses of 6.5 ± 1 nm, 8.5 ± 1.4 nm, 10.2 ± 1.4 nm and 11.8 ± 1.4 nm resulted for the original system and the ones annealed at 90°C , 105°C and 115°C respectively. The data of the whole contrast series are displayed in the appendix page 82 to 85.

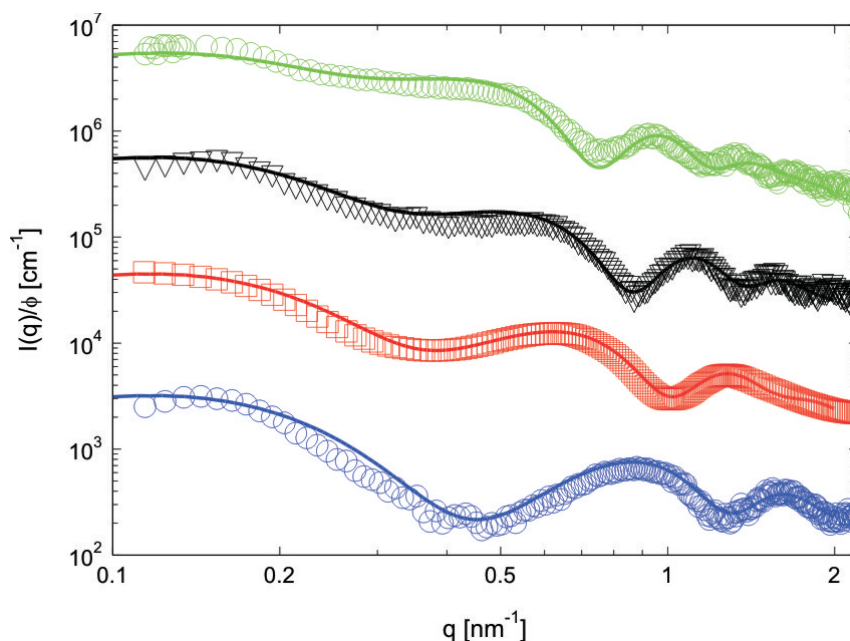


Figure 6.6: Experimental data and corresponding fits of the original sample PL78 dispersed in pure water (blue circles). The volume fractions of the systems are: 2.1 vol%, 1.6 vol%, 2.4 vol% and 2.6 vol% respectively for the original system (bottom) and the ones annealed at 90°C (red squares), 105°C (black triangles) and 115°C (green circles).

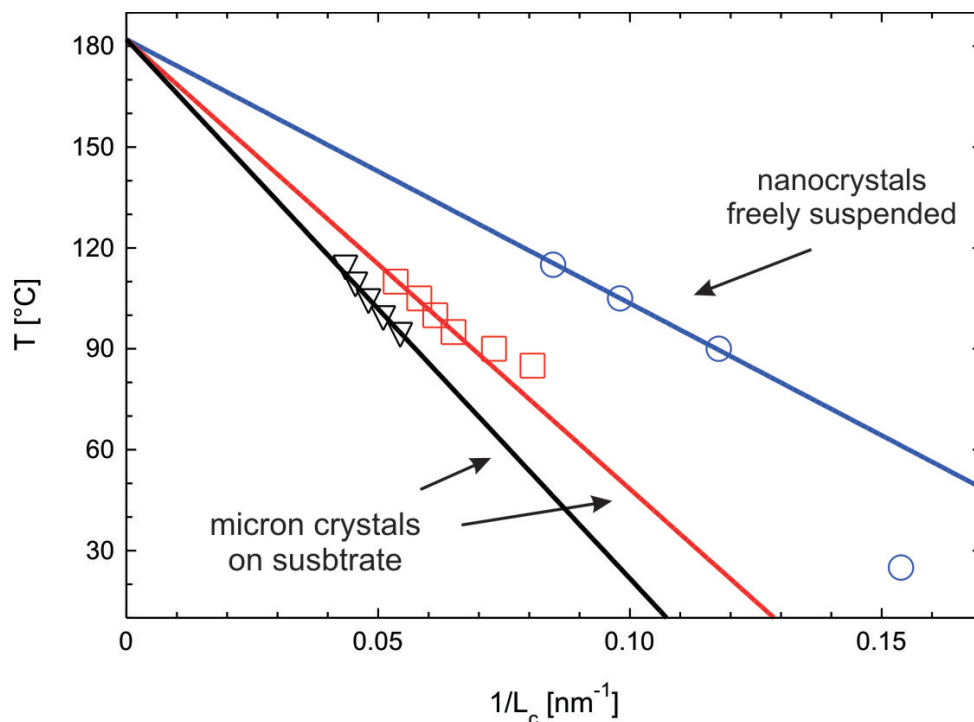


Figure 6.7: Experimental data of the reciprocal of the crystalline thickness depending on the annealing temperature. The data with triangular and square symbols have been obtained from micron crystals originally crystallized at $T=85^{\circ}\text{C}$ and $T=95^{\circ}\text{C}$ respectively [123]. The blue circles represent the data of this study (nanocrystals freely suspended).

Figure 6.7 displays a plot of the annealing temperature against the reciprocal of the crystalline thickness L_c resulted from the fits of the SAXS data. As suggested by the thermodynamic equation 3.3 page 25, these data (blue circles) describe a linear dependency against the reciprocal of the crystalline thickness. As a comparison, experimental data of micron crystals on substrate are plotted [123]. By extrapolation, all data lead to a crystallization temperature of an infinite crystal of the order of $T_c^{\infty}=182^{\circ}\text{C}$. This behaviour may seem intriguing for the case of two different systems, but by extrapolating at an infinite crystal, the substrate effect and the SDS molecules can be neglected.

It is also interesting to compare the results to the thermodynamic scheme of polymers proposed in literature (see figure 3.7 page 24). This leads to figure 6.8 which presents the recrystallization line obtained from this study (red square), the thicknesses of crystalline lamella of PE collected from melt (blue circle [94]) and post-thickened crystalline PE lamella as determined by electron microscopy (green filled circles [123]). The resulting recrystallization line defines a linear relationship between the annealing temperature and the reciprocal of the crystalline lamellar layer. As expected by the corresponding thermodynamic equations 3.2 and 3.3 page 25, the extrapolation of the crystallization and recrystallization lines at an infinite crystalline thickness lead to the same temperature $T_c^{\infty} \approx 182^{\circ}\text{C}$. According to figure 6.7, this T_c^{∞} correspond to the melting temperature of

a fully crystalline PE sample. However, for bulk sample, the crystallization ends up at the intersection with the melting line (black line in figure 6.8) given by $T=141.1-259.7/L_c$ according to reference [125].

For comparison, additional experimental data corresponding to post-thickened PE particles are reproduced in figure 6.8. The post-thickening correspond to a reorganization of the PE chains toward the equilibrium state. This process lead to an increase of the crystalline layer. The original systems of this study (PL78 and PL39) do not belong to the crystallization line as expected but to the post-thickening line (green bold line in figure 6.8). This post-tickening may be explained by the fact that the samples were kept at room temperature [33].

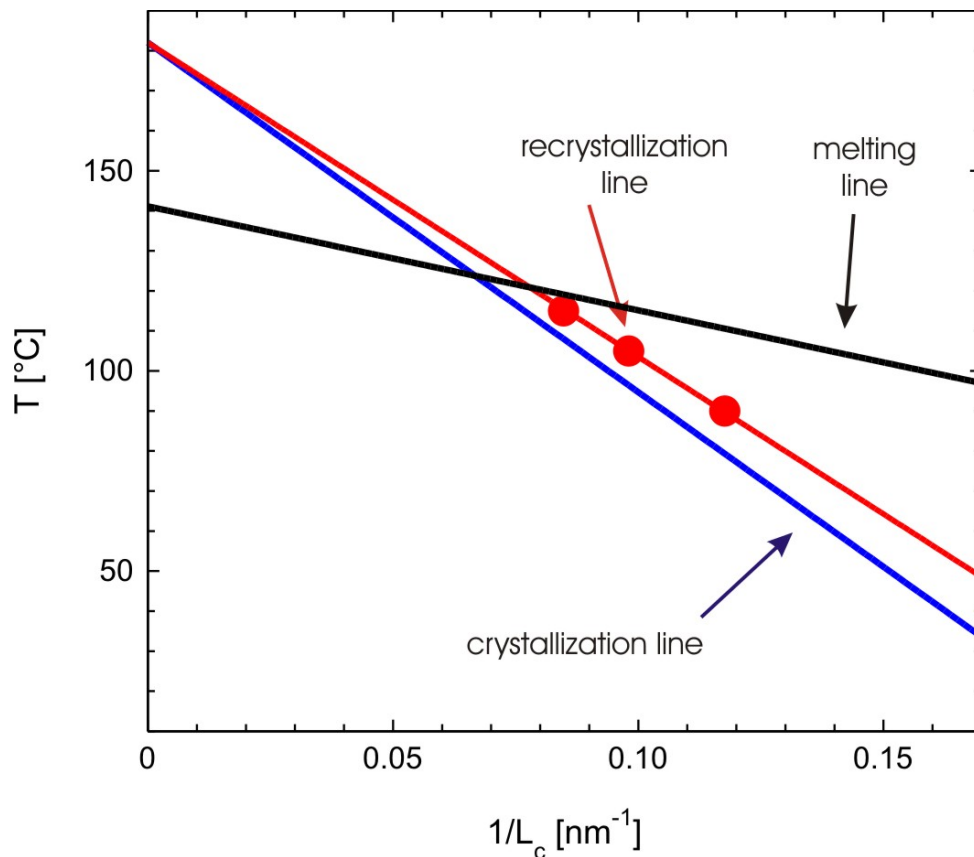


Figure 6.8: Experimental thermodynamic scheme obtained by the help of data in reference [124] (blue circles) and from the present study (red squares). The blue, red and black lines represent respectively the crystallization, recrystallization and melting lines of the thermodynamic scheme proposed in litterature [29,94]. The bold green line is a guide line for the post-thickened experimental data points [123].

Chapter 7

Experimental

7.1 SAXS

7.1.1 Kratky-Compact-Camera

The set-up of the Kratky-Compact-Camera is as follows: The X-ray generator (Siemens, Kristalloflex 710H) contains a sealed X-ray tube (Siemens, KFL-CU-4-K) with copper anode. The operating voltage is 35 kV with a current of 30 mA. A nickel filter is used in order to mask the Cu-K $_{\beta}$ line. The resulting X-ray source is monochromatic with a wavelength of 0.154 nm (Cu-K $_{\alpha}$). Samples are placed in a quartz capillary (diameter 1 mm and thickness of the wall ca. 10 μ m). The primary beam intensity is determined by a moving slit device [126] while scattered intensities and positions are recorded by a linear position-sensitive detector (Braun OED-50m). The scattered intensities in absolute scale were obtained as describe in reference [127].

7.1.2 ID02

The synchrotron experiments were performed at the ESRF (European Synchrotron Radiation Facility) in Grenoble, France, on the high brilliance ID 02 beam line. Figure 7.1 presents a schematic overview of the instrument [128]. The incident wavelength is 1 \AA and the sample-to-detector distance 2 m and 10 m were used. A two-dimensional CCD (charge-coupled device) detector is used to collect the data and allows the study of both isotropic and anisotropic systems. The very high energy used for these experiments (12460 eV) limits the exposure time to few milliseconds and allowed time-resolved investigations. The standard software of the beamline was used to obtain SAXS intensities in absolute scale [129].

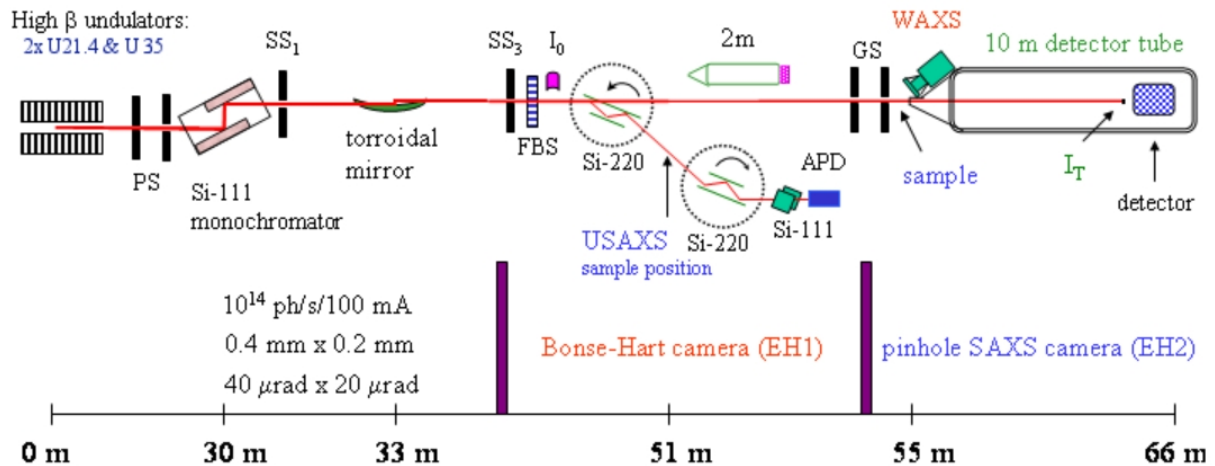


Figure 7.1: Schematic representation of the USAXS/SAXS/WAXS equipment at the ERSF in Grenoble, France. Picture taken from <http://www.esrf.eu/UsersAndScience/Experiments/SoftMatter/ID02/BeamlineLayout> on July, the 1st 2009.

7.2 Dynamic Light Scattering

Dynamic light scattering experiments were carried out by using an ALV/DLS/SLS-5000 compact goniometer system with a multiple tau digital correlator system, equipped with a He-Ne laser ($\lambda=632.8$ nm). The temperature of the sample cell was maintained exactly by using a program-controlled thermostat (Rotilabo) within the error of 0.1°C . For each measurements (30 seconds per angle), the angle between the source, the cell and the detector varies from 30° to 80° with steps of 5° . The measured concentrations varies from 0.0001 wt% up to 0.1 wt%. Measurements were repeated at least three times. In the case of homogeneous spherical particles, the Stoke-Einstein relation applies and the diffusion coefficient D could be written as:

$$D = \frac{k_B T}{6\pi\eta R_h} \quad (7.1)$$

where R_h is the hydrodynamic radius, k_B is the Boltzman's constant, T the absolute temperature and η the viscosity of the solvent. Thus, R_h could be extracted by the help of the software ALV-Correlator version 3.0.

7.3 Densitometry

In order to get quantitative and qualitative piece of information about the different systems studied in this work, the mass density ρ of each studied sample in their respective solvents is necessary. These densities were determined by the help of a densitometer (DMA 60/602, Paar, Graz, Austria) at 25°C . In diluted regime, the density ρ of a solution is proportional to the concentration c of the system. A linear regression permits to

obtain the density of the system ρ_m according to:

$$\rho_m = \frac{\rho_0}{1 - \frac{d\rho}{dc}} \quad (7.2)$$

where ρ_0 is the density of the medium. Figure 7.2 presents the experimental data obtained in order to determine the density of a calcium-phosphate solution.

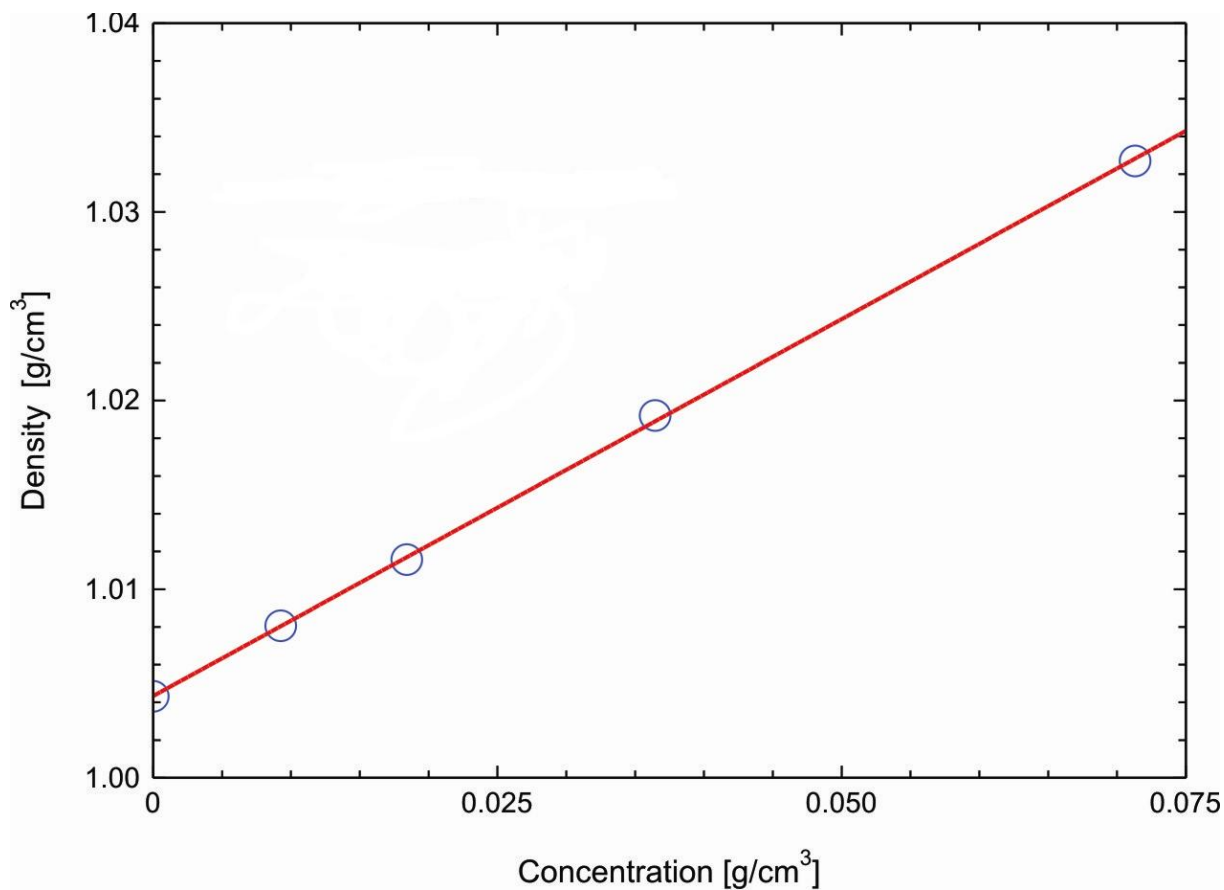


Figure 7.2: Determination of the density of a calcium phosphate system in buffer solution. From the slope, ρ is determined to $1.67 \pm 0.05 \text{ g/cm}^3$.

Chapter 8

Summary

The objective of this work was to analyze nano-scaled particles by the combination of small angle x-ray scattering (SAXS), electron microscopy (TEM and cryo-TEM) and dynamic light scattering (DLS). Two systems with totally different morphologies and compositions have been investigated: spherical particles of calcium-phosphate-protein complexes and hamburgers of semi-crystalline polybutadiene/polyethylene nanoparticles.

8.1 Calcification

The study of the calcium-phosphate-protein complexes consisted in looking for the influence of a protein, Fetuin-A, also called ahsg, onto the calcification at early stage. For the purpose, calcium and phosphate ions were mixed with or without the presence of Fetuin-A in a buffer solution of pH=7.4. In a first step, DLS measurements were realized to better appreciate the effect of the total weight percentage of Ca^{2+} and PO_4^{3-} ions. These experiments, without addition of ahsg, demonstrated that for a lower weight fraction, the particles formed are smaller.

Studies with addition of Fetuin-A affected the calcification during the first minute of this process. The early formation of calcium phosphate complexes has been successfully followed by TR-SAXS. A very fast nucleation of nanoparticles within 1 second has been detected. For the first time, the role of the glycoprotein Fetuin-A at the very early stage of calcification has been qualitatively highlighted: ahsg inhibits the aggregation of calcium phosphate particles. Thus, Fetuin-A plays an important role in the fetal serum in the pre-formation of the skeleton of Vertebrates. This study demonstrated that a physiological concentration of this glycoprotein ($15 \mu\text{M}$) is sufficient to completely inhibit the aggregation of calcium phosphate particles.

Figure 8.1 resumes the results obtained. The TEM micrographs on the right present TEM of the system without added protein (bottom) and with the presence of $15 \mu\text{M}$ of ahsg, that is a physiological concentration. At the early stage of calcification, the nucleation

of calcium-phosphate particles appear. Once a certain size of these particles is achieved, Fetuin-A, if present, acts as a shield and cover the calcified particles in order to prevent further aggregation. The systems without added protein or with low concentration of Fetuin-A aggregate.

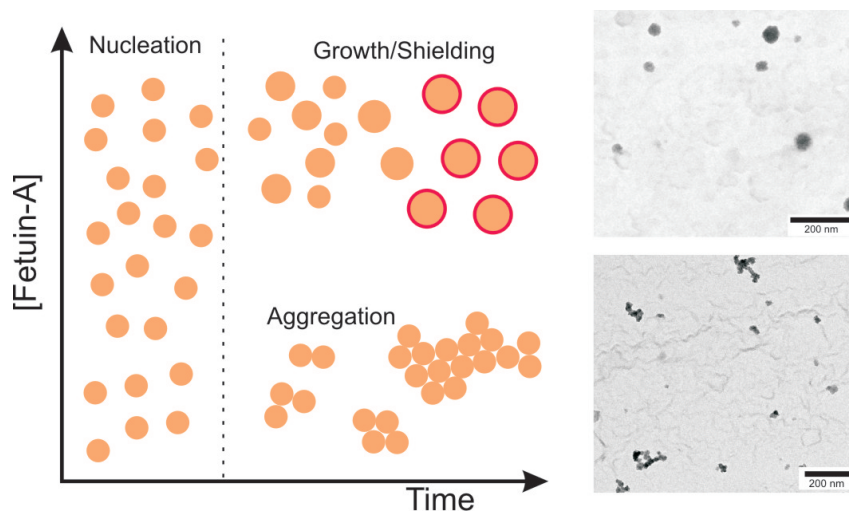


Figure 8.1: Hypothetical model of the influence of Fetuin-A (red) onto the formation of calcium phosphate complexes (orange). Black and white images on the right present TEM micrographs of calcium-phosphate particles formed without (bottom) and in presence of $15 \mu\text{M}$ of Fetuin-A (top).

8.2 Polybutadiene

Freely suspended nanoparticles of syndiotactic polybutadiene have been studied. By using the combination of cryo-TEM and SAXS, it has been shown that they consist of remarkably thin polymer crystalline lamella. Different models have been compared in order to theoretically fit the experimental SAXS data: homogeneous and heterogeneous (two and three different electron densities within one particle) nanoparticles. The presence of amorphous and crystalline polybutadiene has been demonstrated by the X-ray diffraction. The necessity of using an additional layer of SDS for the modeling is explained by the abundance of SDS added after the synthesis of the polybutadiene particles (weight ratio ca. 1:1) and by the modeling of the SAXS theoretical intensities which were not sufficient without taking into account the presence of SDS.

After the formation of semi-crystalline nanoparticles of PE, these new nanoparticles open a new route to the synthesis of nanopolymers of interesting physico-chemical properties such as semi-conductors or photovoltaic compounds.

8.3 Polyethylene

Finally, in contrast to recent literature on bulk polyethylene (PE), this thesis investigated freely suspended nanoparticles of PE. As suggested by Weber and coworkers [33], the combination of SAXS and cryo-TEM has been used for this study. The structure of individual PE nanocrystals has been determined in detail and an improved model of the form factor (SAXS) has been developed in close collaboration with Priv.-Doz. Dr. Ludger Harnau. The second part of this thesis mainly deals with the annealing of these PE particles. For the first time, it is shown that the effect of the annealing process results in a doubling of the crystalline layer of the PE nanoparticles. This behaviour could be traced back to the unlooping of the PE chains. In addition, a linear relationship between the reciprocal of the crystalline layer and the annealing temperature has been experimentally drawn. This line was predicted by the Gibbs-Thomson equation according to the literature [34]. This result is important because it allows to control the crystalline thickness and physical properties of the system, by the temperature.

Figure 8.2 is a sketch of the obtained results on the PE nanocrystals: The original semicrystalline PE nanoparticles have a very thin crystalline lamella. By annealing at a temperature far below the melt, a thickening of the lamella occurs. This behaviour ends up at the melting line.

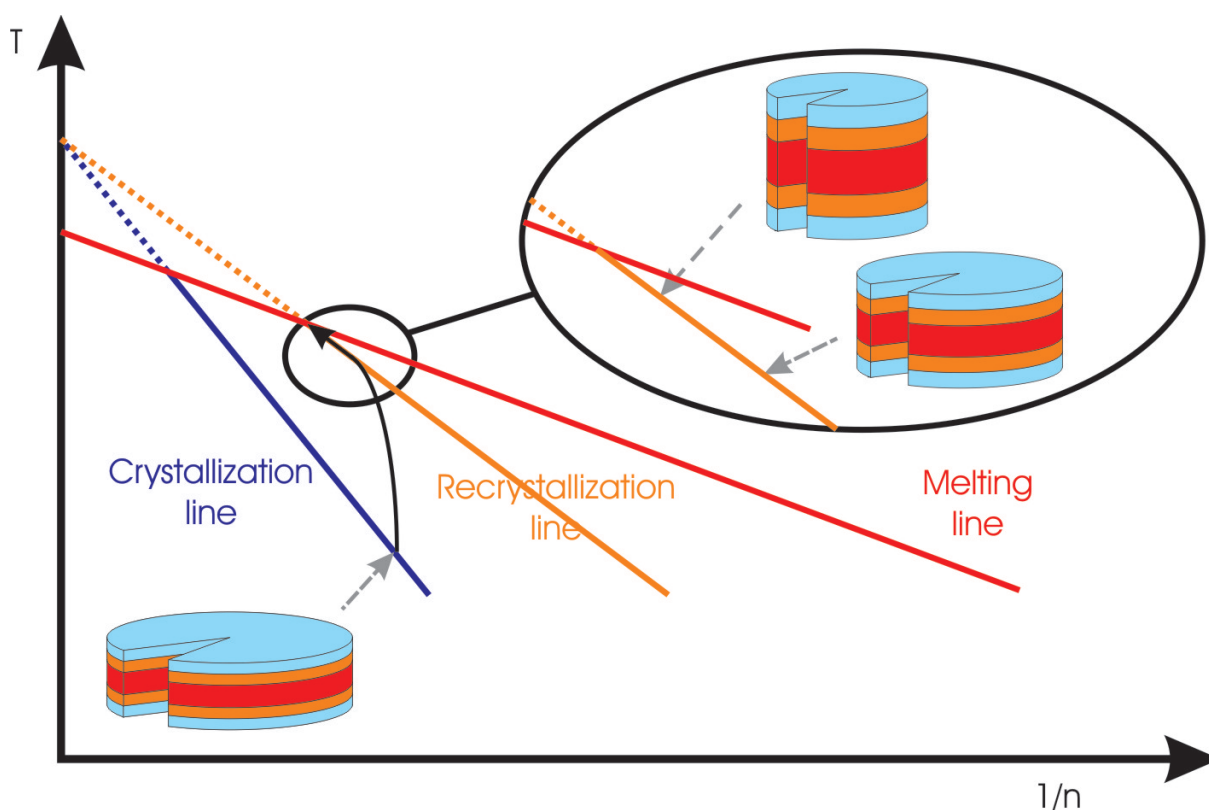


Figure 8.2: Schematical resume of the experiments realized onto the PE nanoparticles annealed at different temperatures. T is the temperature and n is the number of monomer units in the crystalline thickness.

Chapter 9

Zusammenfassung

Das Ziel dieser Arbeit war, durch eine Kombination von Kleinwinkelröntgenstreuung (SAXS), Elektronenmikroskopie (TEM und Kryo-TEM) und dynamischer Lichtstreuung (DLS) Teilchen mit Größen im Nanometerbereich im Detail zu analysieren. Dazu wurden zwei Systeme mit sehr unterschiedlicher Morphologie und Zusammensetzung untersucht: Kugelförmige Teilchen von Calciumphosphat-Protein-Komplexen und heterogene Scheibchen von Polyethylen/Polybutadien.

9.1 Calcifizierung

Die Arbeiten über Calciumphosphat-Protein-Komplexen befassten sich mit dem Einfluss des Proteins Fetuin-A, auch AHSG genannt, auf die Calcifizierung zu frühen Zeitpunkten. Dazu wurden Calcium- und Phosphationen mit und ohne Fetuin-A in einer Pufferlösung mit $\text{pH} = 7,4$ gemischt. In einem ersten Schritt wurden DLS-Messungen durchgeführt, um den Einfluss der absoluten Gewichtsanteile der Ca^{2+} und PO_4^{3-} -Ionen besser zu verstehen. Durch diese Experimente wurde herausgefunden, dass ohne Zugabe von AHSG die gebildeten Teilchen mit kleinerem Gewichtsanteil dieser Ionen kleiner sind.

In weiteren Experimenten wurde der Einfluss von Fetuin-A auf den Prozess der Calcifizierung während der ersten Minute untersucht. Die frühe Bildung von Calciumphosphat-Komplexen konnte erfolgreich mit TR-SAXS verfolgt werden. Dabei wurde eine schnelle Nukleierung von Nanopartikeln innerhalb einer Sekunde beobachtet. Zum ersten Mal konnte die Rolle des Glycoproteins Fetuin-A in der sehr frühen Phase der Calcifizierung qualitativ beschrieben werden: AHSG verhindert die Aggregation der Calciumphosphat-Teilchen. Fetuin-A spielt demnach eine wichtige Rolle im fötalen Serum in der Vorbildung des Skelets von Wirbeltieren. Die Untersuchung hat ferner gezeigt, dass eine physiologische Konzentration von $15 \mu\text{M}$ dieses Glycoproteins ausreicht, um die Aggregation der Calciumphosphat-Teilchen vollständig zu verhindern.

In Abbildung 9.1 sind die Ergebnisse zusammengefasst. Die TEM-Aufnahmen auf der rechten Seite zeigen das System ohne Protein (unten) und mit $15 \mu\text{M}$ AHSG (oben),

der physiologischen Konzentration. Im frühen Stadium der Calcifizierung zeigt sich die Nukleierung der Calciumphosphat-Teilchen. Wenn diese Teilchen eine bestimmte Größe erreicht haben, wirkt Fetuin-A, wenn es in der Lösung vorhanden ist, als Abschirmung und umhüllt die calcifizierten Teilchen, um so eine weitere Aggregation zu verhindern. Systeme ohne Protein oder mit einer geringen Konzentration von Fetuin-A weisen Aggregation auf.

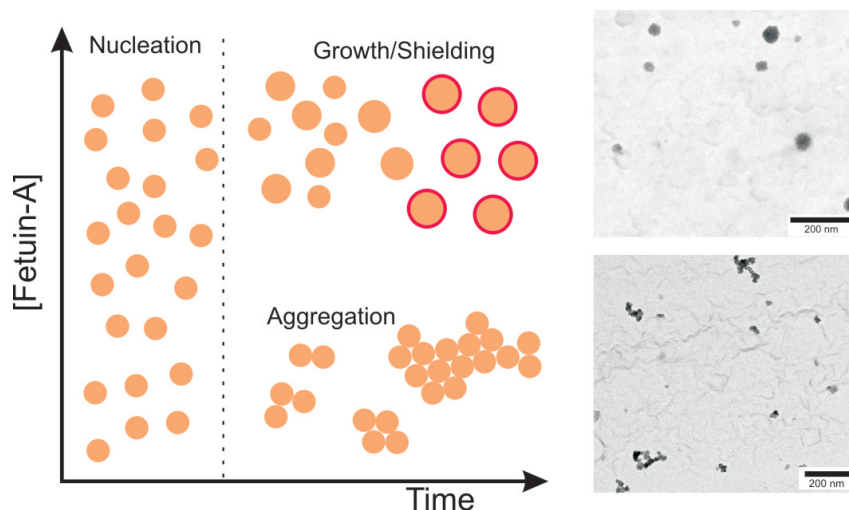


Figure 9.1: Vorgeschlagenes Modell des Einflusses von Fetuin-A (rot) auf die Bildung von Calciumphosphat-Teilchen (orange). Die Bilder auf der rechten Seite zeigen TEM-Aufnahmen der Calciumphosphat-Komplexen, die ohne (unten) und mit $15 \mu\text{M}$ Fetuin-A (oben) gebildet wurden.

9.2 Polybutadien

Es wurden frei suspendierte Nanopartikel aus syndiotaktischem Polybutadien untersucht. Mittels einer Kombination aus cryo-TEM und SAXS wurde gezeigt, daß die Partikel eine bemerkenswert dünne kristalline Polymerlamelle besitzen. Verschiedene Modelle für homogene und heterogene Nanopartikel (mit zwei oder drei verschiedenen Streulängendichten innerhalb eines Teilchens) wurden miteinander verglichen um eine optimale theoretische Beschreibung der experimentellen Röntgenkleinwinkelstreudaten zu erhalten. Das Vorliegen von amorphem und kristallinem Polybutadienbereichen wurde mittels Röntgendiffraktion gezeigt. Die Notwendigkeit einer zusätzlichen SDS-Schicht bei der Modellierung ist auf den SDS-Überschuß während der Synthese der Polybutadienpartikel (Gewichtanteil ca. 1:1) zu erklären. Eine Beschreibung der theoretischen Röntgenkleinwinkelstreuintensitäten ist ungenügend wenn die Anwesenheit von SDS nicht berücksichtigt wird. Die Bildung von semikristallinen PE-Nanopartikeln ermöglicht eine neue Syntheseroute zu Nanopolymeren mit interessanten physikalisch-chemischen Eigenschaften wie sie in Halbleitern oder photovoltaische Komponenten gefunden werden.

9.3 Polyethylen

Im Gegensatz zur neueren Literatur über Polyethylen (PE) im Bulk wurden in dieser Arbeit frei suspendierte PE-Nanopartikel untersucht. Wie von Weber et al. [33] vorgeschlagen, wurde dazu eine Kombination aus SAXS und Kryo-TEM verwendet. Die Struktur von einzelnen kristallinen PE-Nanoteilchen wurde im Detail beschrieben und ein verbessertes Modell für den Formfaktor für SAXS in enger Zusammenarbeit mit Priv.-Doz. Dr. Ludger Harnau entwickelt. Der zweite Teil der Arbeit beschäftigt sich mit dem Tempern dieser PE-Teilchen. Zum ersten Mal wurde gezeigt, dass der Temperungsprozess eine Verdopplung der kristallinen Schichtdicken der PE-Nanopartikel bewirkt. Dieses Verhalten kann auf ein Entfalten der PE-Polymerketten zurückgeführt werden. Zusätzlich wurde experimentell eine lineare Beziehung zwischen der Reziproken der kristallinen Schichtdicke und der Temperatempertemperatur hergestellt. Diese Linie wurde auf Basis der Gibbs-Thomson-Gleichung in der Literatur [34] vorausgesagt. Dieses wichtige Ergebnis zeigt, dass die kristalline Dicke und physikalischen Eigenschaften des Systems durch die Temperatur kontrolliert werden kann.

Abbildung 9.2 zeigt schematisch die Ergebnisse über die PE-Nanokristalle: Die kristalline Lamelle der ursprünglich semikristallinen PE-Nanopartikel ist sehr dünn. Durch Tempern bei Temperaturen weit unterhalb der Schmelze findet eine Verdickung der Lamelle statt. Dieses Verhalten endet an der Schmelzkurve.

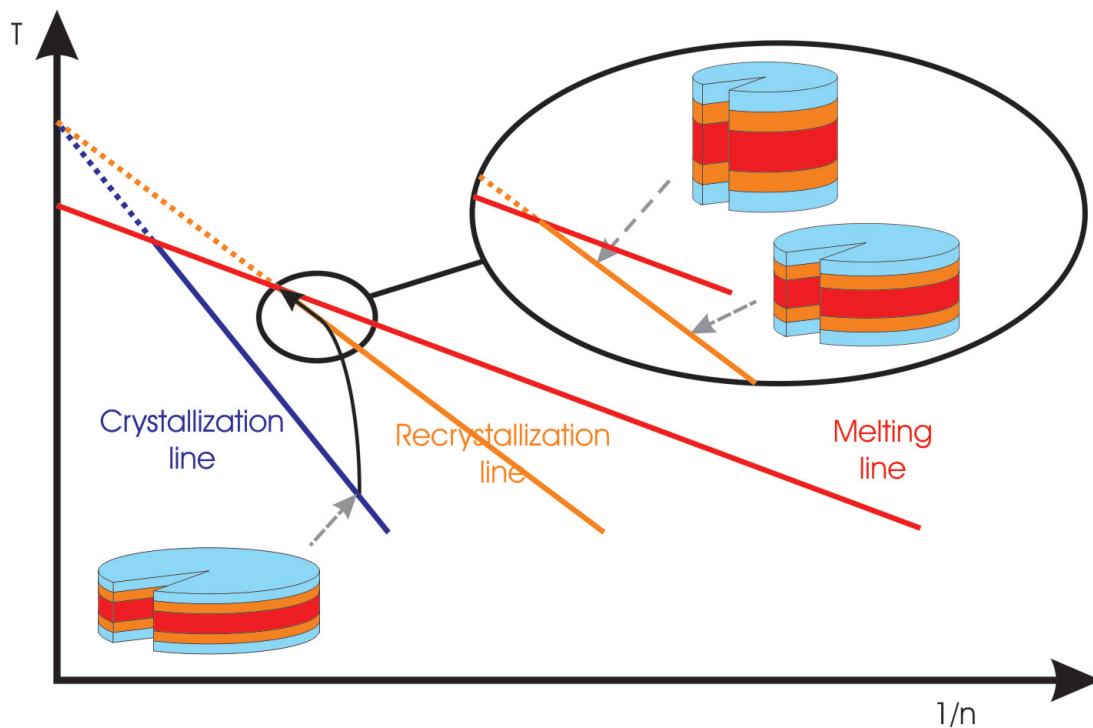


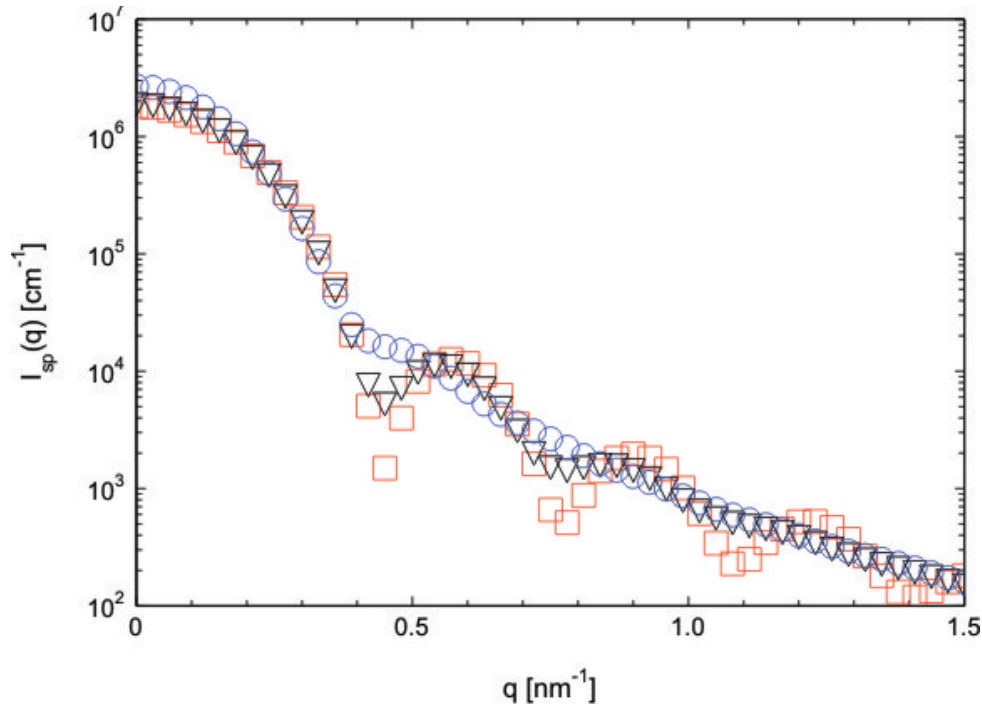
Figure 9.2: Schematische Zusammenfassung der Experimente mit PE-Nanopartikeln und verschiedenen Temperatempertemperaturen.

Appendices

Appendix A

Theory of SAXS

A.1 Effect of polydispersity



Effect of the polydispersity onto the scattering intensity of an ensemble of non-interacting spherical particles of mean radius $R_0=10$ nm. Polydispersities used here are 5%, 10% and 20% in gaussian distribution (corresponding respectively to 0.5 (red square), 1.0 (black triangle) and 2.0 nm (blue circles) for their standard deviations σ). $\Delta\rho$ is here equals to 1 e.u. nm^{-3} and $\frac{N}{V}$ is equal to unity. The intensity at $q=0$ grow with the polydispersity. At high polydispersity, the first peak is hardly visible and thus piece of information are lost.

A.2 C++ programs

A.2.1 form factor of homogenous spherical polydisperse particles

```

#include <iostream>
#include <stdio.h>
#include <stdlib.h>
#include <math.h>
#include <time.h>

int main (void)
{
    int i,j,k,l,m,n, reff, rmoy;
    float
r1, rho1, r2, rho2, proba, y, vp, pi, q, nsurv, y1, y2, vp1, vp2, probabilite, gammaz, Z, rg, t,
tinc, nsurvi, sumproba, intproba, probaavant;
    FILE *fa, *fb, *fc, *fe;
    char file[200], col1[500], col2[500], col3[500], col4[500];

    nsurv=3.40E-12;
    nsurvi=nsurv*1.0E12;
    rg=12.0;
    Z=rg*0.35;
    pi=3.141592654;
    fb=fopen("gauss.txt", "w");
    r1=0.0;
    tinc=0.0002;
    gammaz=0.5*pow(tinc, Z)*exp(-tinc)*tinc;
    t=tinc;

    intproba=0.0;
    rho2=128.0*128.0;

    r1=r1+0.10;
    probabilite=1.0/(Z*pow(2.0*pi, 0.5))*exp(-0.5*pow((r1-rg)/Z, 2.0));
    intproba=0.1*0.5*probabilite;
    fprintf(fb, "%f %f\n", r1, probabilite);
    sumproba=probabilite;
    for(i=0; i<200; i++){
        r1=r1+0.10;
        probaavant=probabilite;
        probabilite=1.0/(Z*pow(2.0*pi, 0.5))*exp(-0.5*pow((r1-
rg)/Z, 2.0));

        sumproba=sumproba+probabilite;
        intproba=intproba+0.1*0.5*(probabilite+probaavant);
        fprintf(fb, "%f %f\n", r1, probabilite);
        if(r1>=40.0){break;}
    }
    fprintf(fb, "%s %f\n", "Somme proba=", sumproba);
    fprintf(fb, "%s %f", "Integralle proba dr=", intproba);
    fclose(fb);

    fe=fopen("serie01-4498.txt", "r");
    fc=fopen("output.txt", "w");
    fprintf(fc, "%s%f\n", "# sigma= ", Z);

```

```

fprintf(fc,"%s%f\n", "# %= ", Z*100.0/rg);
fprintf(fc,"%s%f\n", "# R= ", rg);
fprintf(fc,"%s%f%s\n", "# N/V= ", nsurvi/10.0, "E-12");

for(k=0;k=200;k++){
    fscanf(fe,"%s%s", col1,col2);
    sscanf(col1,"%f",&q);
    fa=freopen("gauss.txt", "r", stderr);
    printf("%f\n",q);
    y=0.0;

    for(l=0;l=200;l++){
        fscanf(fa,"%s%s", col1,col2);
        sscanf(col2,"%f",&proba);
        sscanf(col1,"%f",&r1);

        vp2=pow((4.0/3.0)*pi*pow(r1,3.0),2.0);
        y=y+proba*vp2*pow(3.0*(sin(q*r1)-
q*r1*cos(q*r1))/pow(q*r1,3.0),2.0);
        if(r1>=39.0){
            fprintf(fc,"%f
%f\n",q,y*rho2*nsurv/sumproba+1.0E-2/(1.0+q*q*2.5*2.5));
            fclose(fa);
            break;}}
        if(q>=0.52){break;}}
    }
}

```

A.2.2 structure factor of the aggregation of spherical particles

```

#include <iostream>
#include <stdio.h>
#include <stdlib.h>
#include <math.h>
#include <time.h>

int main (void)
{
    int i,j,k,l,m;
    FILE *fb;
    float q,y,yfit,xsi,xsi1,dim,dim1,s0,s01,sommedelta,delta,bestsomme;
    char col1[200],col2[200],col3[200],col5[200],col4[200];

    fb=fopen("sofq.txt","w");

    xsi=26.0;
    dim=2.8;
    s0=14.0;

    fprintf(fb,"%s %f\n","xsi=",xsi);
    fprintf(fb,"%s %f\n","dim=",dim);
    fprintf(fb,"%s %f\n","s0=",s0);

    for(m=0;m=200;m++){
        fscanf(fd,"%s%s",col3,col4);
        sscanf(col3,"%f",&q);

        y=1.0+s0/(pow(1.0+q*q*xsi*xsi,0.5*(dim-1.0)))*(sin((dim-
1.0)*atan(q*xsi)))/((dim-1.0)*q*xsi);
        fprintf(fb,"%f %f\n",q,y);
        if(q>=1.47){break;}}
}

```

A.3 Modified hamburger model

```

#include <iostream>
#include <math.h>
#include <fstream>
#include <vector>
#include <cstdio>
#include <windows.h>
using namespace std;

const double PI = 3.141592654;

int main(){

    //files
    ifstream q_file,para_file;
    ofstream output;
    //arrays
    vector<double>
    grc,rrc,q,i_q1,i_q2,i_q3,i_q4,alfa,glc,llc,glc,lla,gllds,llsds,i_q5;

    //variables
    double
    tmp,Ra,Rc,dRsds,dRc,dRa,d_ros,d_roc,solvent1,solvent5,solvent2,solvent3,solven
t4,Lsds,dLsds,d_sds,epsilon,Lc,dLc,La,dLa,Lc2,La2;
    int i,j,k,l,m,n,inc=0;
    char stmp[256],sortie[30];
    para_file.open("parameters.txt");
    if(para_file.is_open())
    {
        while (! para_file.eof())

        para_file >> Rc >> dRc >> Lc >> dLc >> La >> dLa >> Lsds >> dLsds >> d_roc
>> d_ros >> d_sds >> solvent1 >> solvent2 >> solvent3 >> solvent4;

        para_file.close();
    }
    else cout << "Unable to open file";

    q_file.open ("serieq-moyenne2.txt");

    /* read from file in a loop
    this routine skips empty lines (it is safe to have a new line at the
eof)
    */
    if (q_file.is_open()) //checks if there is an error opening the file
    {
        while (! q_file.eof() )
        {
            // read in a tmp c-string; length of line can be modified
            q_file.getline(stmp,256);

            if (q_file.gcount()>0)

```

```

    {
        //checks if the line is not empty, and read the double on the
line
        sscanf(stmp, "%lf", &tmp);
        q.push_back(tmp);
    }
}

//when reached eof (end of file), close the file
q_file.close();
}
else
{
    //if unable to open file, return error
    cout << "An error has occurred: unable to open the file serieq.txt";
    return 1; // exit with error
}

double r_inc=Rc-2.0*dRc,rinc=dRc/2.0;
for(i=0;i<=8;i++){
    grc.push_back(1/(dRc*pow(2.0*PI,0.5))*exp(-0.5*pow((Rc-
r_inc)/(dRc,2.0))/0.9545);
    rrc.push_back(r_inc);
    r_inc+=rinc;}
double sommeprobar=0.0,sommeprobalc=0.0,sommeprobala=0.0;
for(i=0;i<=8;i++)
    sommeprobar+=grc[i];

for(i=1;i<=249;i++)
    alfa.push_back(PI/2.0/250.0*(double)i);

k=0;
l=0;
m=0;
n=0;
double
grc,qlc,qla,gra,sommealfa1,somme1,sommealfa2,somme5,sommealfa5,somme2,sommealf
a3,somme3,sommealfa4,somme4,qlsds,pe,bessel;

double lc_inc=Lc-2.0*dLc,lcinc=dLc/2.0;
glc.clear();
llc.clear();
for(i=0;i<=8;i++){
    glc.push_back(1/(dLc*pow(2.0*PI,0.5))*exp(-0.5*pow((Lc-
lc_inc)/(dLc,2.0))/0.9545);
    llc.push_back(lc_inc);
    lc_inc+=lcinc;}
    sommeprobalc=0.0;
    for(i=0;i<=8;i++)
        sommeprobalc+=glc[i];

double la_inc=La-2.0*dLa,lainc=dLa/2.0,Rsds,qrsds;
gla.clear();
lla.clear();

```

```

    for (i=0; i<=8; i++) {
        gla.push_back(1/(dLa*pow(2.0*PI, 0.5))*exp(-0.5*pow((La-
la_inc)/(dLa), 2.0))/0.9545);
        lla.push_back(la_inc);
        la_inc+=linc;
        sommeprobala=0.0;
        for (i=0; i<=8; i++)
            sommeprobala+=gla[i];

        for (i=0; i<q.size(); i++) {
            somme1=0.0;
            somme2=0.0;
            somme4=0.0;
            somme3=0.0;

            while (k<=(rrc.size()-1)) { //R
                Rc=rrc[k];
                while (l<=(llc.size()-1)) { //Lc
                    Lc=llc[l];
                    while (m<=(lla.size()-1)) { //La
                        La=lla[m];

                        sommealfa1=0.0;
                        sommealfa2=0.0;
                        sommealfa3=0.0;
                        sommealfa4=0.0;

                        for (j=0; j<alfa.size(); j++) {
                            qrc=q[i]*Rc*sin(alfa[j]);
                            qlc=q[i]*Lc*cos(alfa[j])/2.0;
                            qla=q[i]*(La+Lc)*cos(alfa[j])/2.0;
                            qlsds=q[i]*(La+Lc+Lsds)*cos(alfa[j])/2.0;

                            bessel=2.0*j1(qrc)/qrc*Rc*Rc*(Lc+La+Lsds)*PI*sin(qlsds)/qlsds;
                            pe=2.0*j1(qrc)/qrc*Rc*Rc*(Lc+La)*PI*sin(qla)/qla*(d_ros-d_sds)
+2.0*j1(qrc)/qrc*Rc*Rc*Lc*PI*sin(qlc)/qlc*(d_roc-d_ros);
                            sommealfa1+=pow(bessel*(d_sds-
solvent1)+pe, 2.0)/250.0*PI/2.0*sin(alfa[j]);
                            sommealfa2+=pow(bessel*(d_sds-
solvent2)+pe, 2.0)/250.0*PI/2.0*sin(alfa[j]);
                            sommealfa3+=pow(bessel*(d_sds-
solvent3)+pe, 2.0)/250.0*PI/2.0*sin(alfa[j]);
                            sommealfa4+=pow(bessel*(d_sds-
solvent4)+pe, 2.0)/250.0*PI/2.0*sin(alfa[j]);
                        }

                        somme1+=grc[k]/sommeprobar*(glc[l]/sommeprobalc+gla[m]/sommeprobala)*sommealfa
1;

                        somme2+=grc[k]/sommeprobar*(glc[l]/sommeprobalc+gla[m]/sommeprobala)*sommealfa
2;

                        somme3+=grc[k]/sommeprobar*(glc[l]/sommeprobalc+gla[m]/sommeprobala)*sommealfa
3;

                        somme4+=grc[k]/sommeprobar*(glc[l]/sommeprobalc+gla[m]/sommeprobala)*sommealfa

```

```
4;  
    m++;}m=0;  
    l++;}l=0;  
    k++;}k=0;  
    i_q1.push_back(somme1);  
    i_q2.push_back(somme2);  
    i_q3.push_back(somme3);  
    i_q4.push_back(somme4);  
    }  
  
    double facteur=i_q1[33]/0.081;  
    output.open("output.txt");  
    for (i=0;i<q.size();i++)  
    output << q[i] << "\t" << i_q1[i]/facteur/1e3 << endl;  
  
    for (i=0;i<q.size();i++)  
    output << q[i] << "\t" << i_q2[i]/facteur/1e2 << endl;  
  
    for (i=0;i<q.size();i++)  
    output << q[i] << "\t" << i_q3[i]/facteur/1e1 << endl;  
  
    for (i=0;i<q.size();i++)  
    output << q[i] << "\t" << i_q4[i]/facteur/1e0 << endl;  
  
    return 0;  
}
```

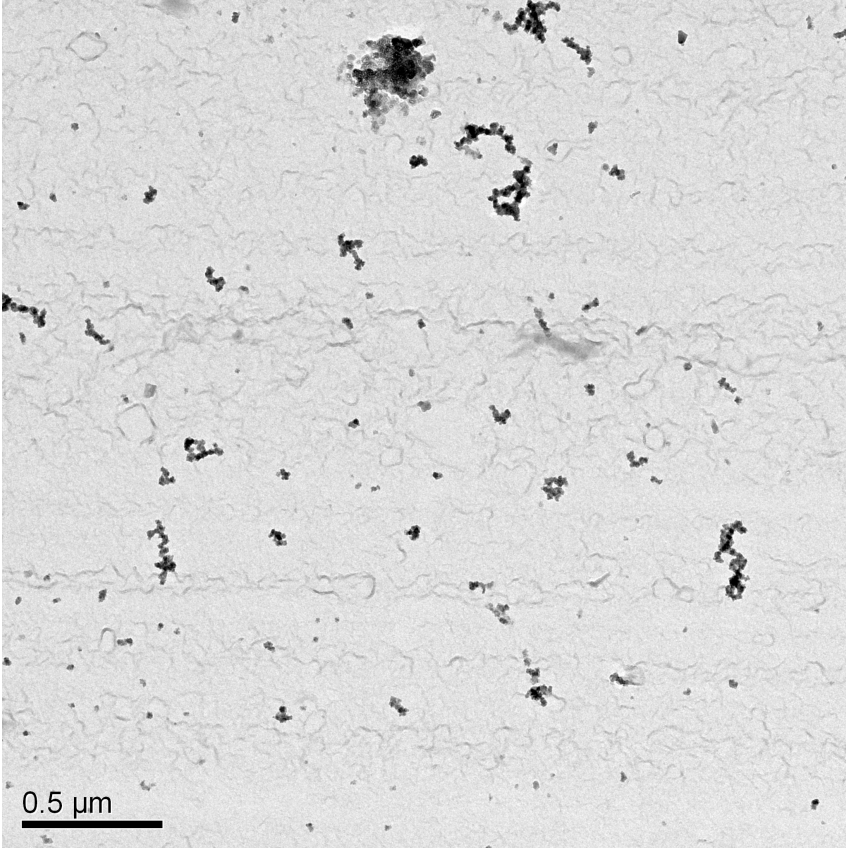
Appendix B

Additional experimental information

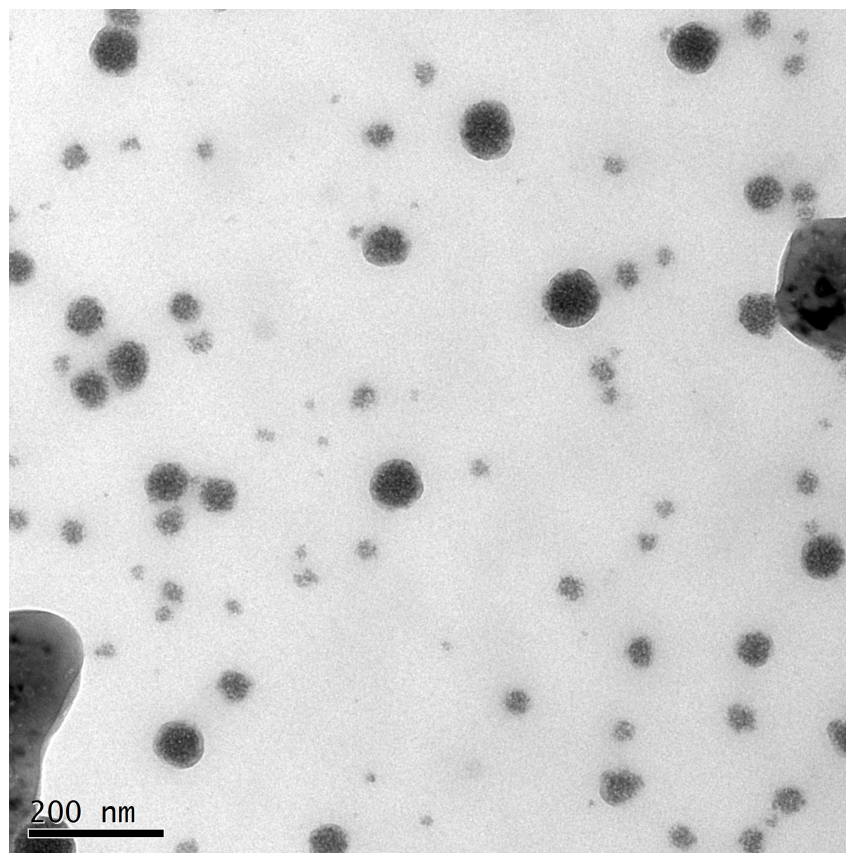
B.1 TEM pictures of calcium phosphate complexes

These samples were prepared by mixing 20 mM of Ca^{2+} with 12 mM of PO_4^{3-} in the buffer solution. For samples with Fetuin-A, the concentration of the protein was adjusted in each ionic solution.

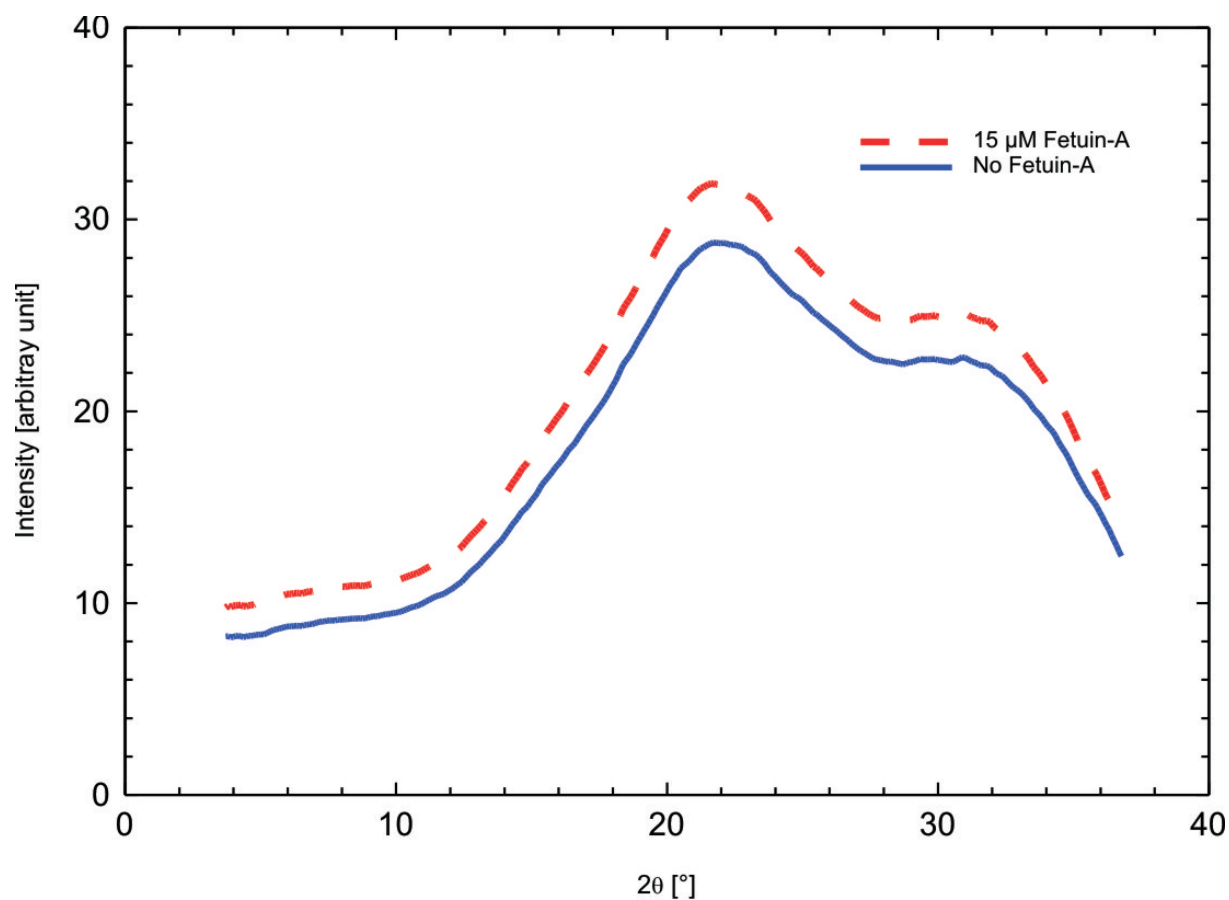
B.1.1 Without addition of Fetuin-A



B.1.2 With 30 μM of Fetuin-A



B.2 WAXS signal of calcium phosphate complexes

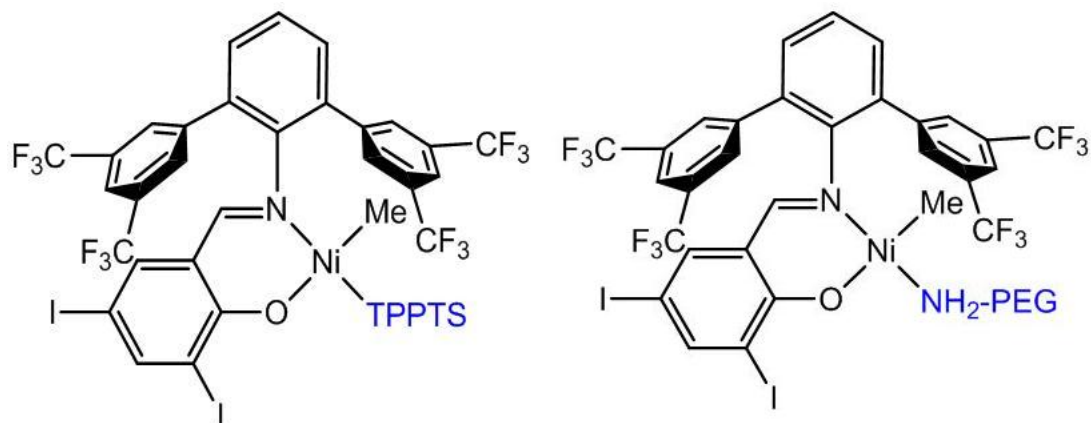


The previous figure presents WAXS signal of the calcium-phosphate complexes without (blue full line) and in presence of 15 μM of Fetuin-A (red bold line). Due to the absence of crystalline peak, the systems have been assumed as amorphous.

B.3 Synthesis of the polyethylene nanoparticles

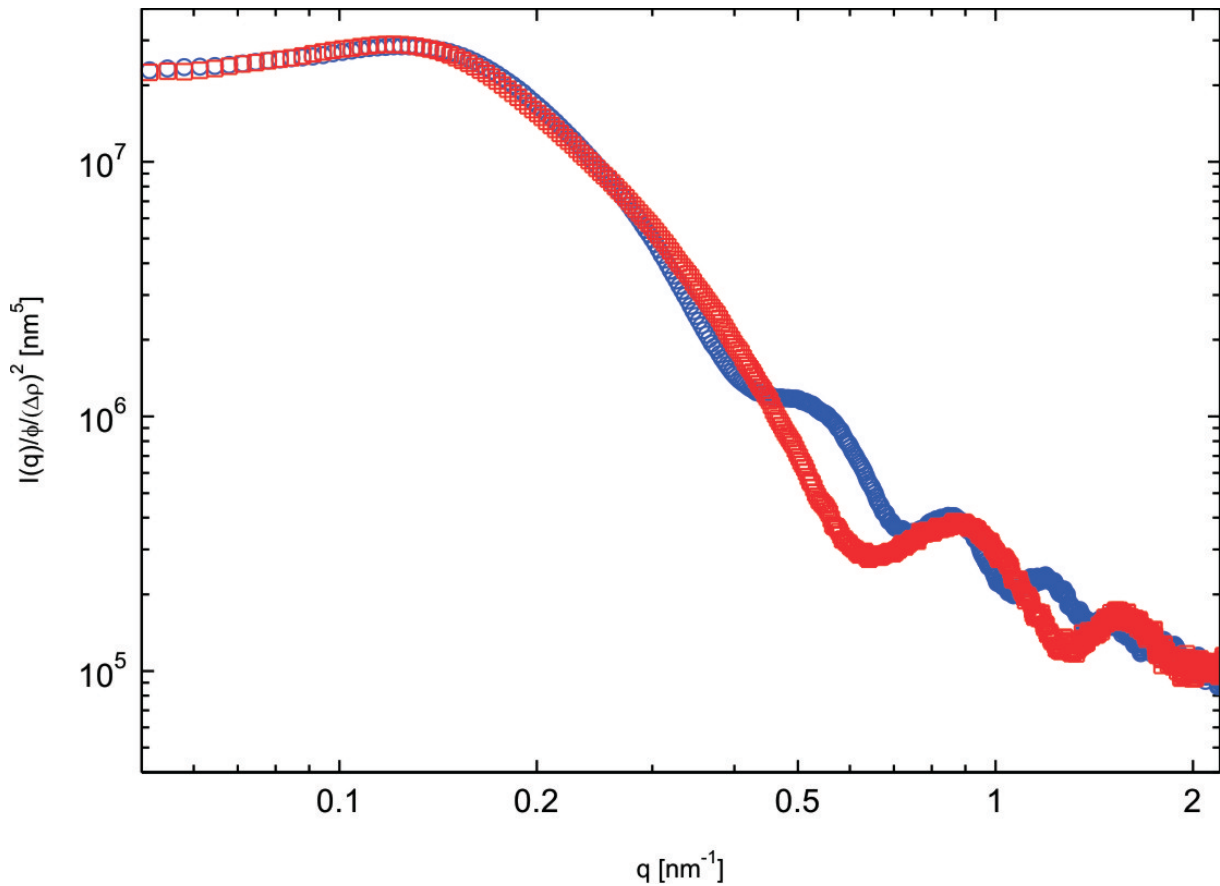
The synthesis of the nanoparticles were realized in Konstanz, Germany, by Dr. Qiong Tong.

Dispersion synthesis was carried out in a 300 mL stainless steel mechanically stirred (1000 rpm) pressure reactor equipped with a heating/cooling jacket supplied by a thermostat controlled by a thermocouple dipping into the polymerization mixture. To a mixture of 750 mg of SDS (Fluka, 98%) and 10 μmol of the Ni(II)-complex in a 250 mL Schlenk flask was added 100 mL of distilled and degassed water at room temperature. The resulting homogenous solution was then cannula-transferred to the argon flushed reactor cooled at 12°C. The reactor was pressurized to a constant ethylene pressure of 40 bar while the temperature was adjusted at 15°C. After 30 min reaction time, ethylene feeding was interrupted, the reactor was carefully depressurized, and the obtained dispersion was filtrated through a plug of glass wool.



The left molecule is the catalyst used for the synthesis of PL39. The right molecule is the catalyst used for the synthesis of PL78.

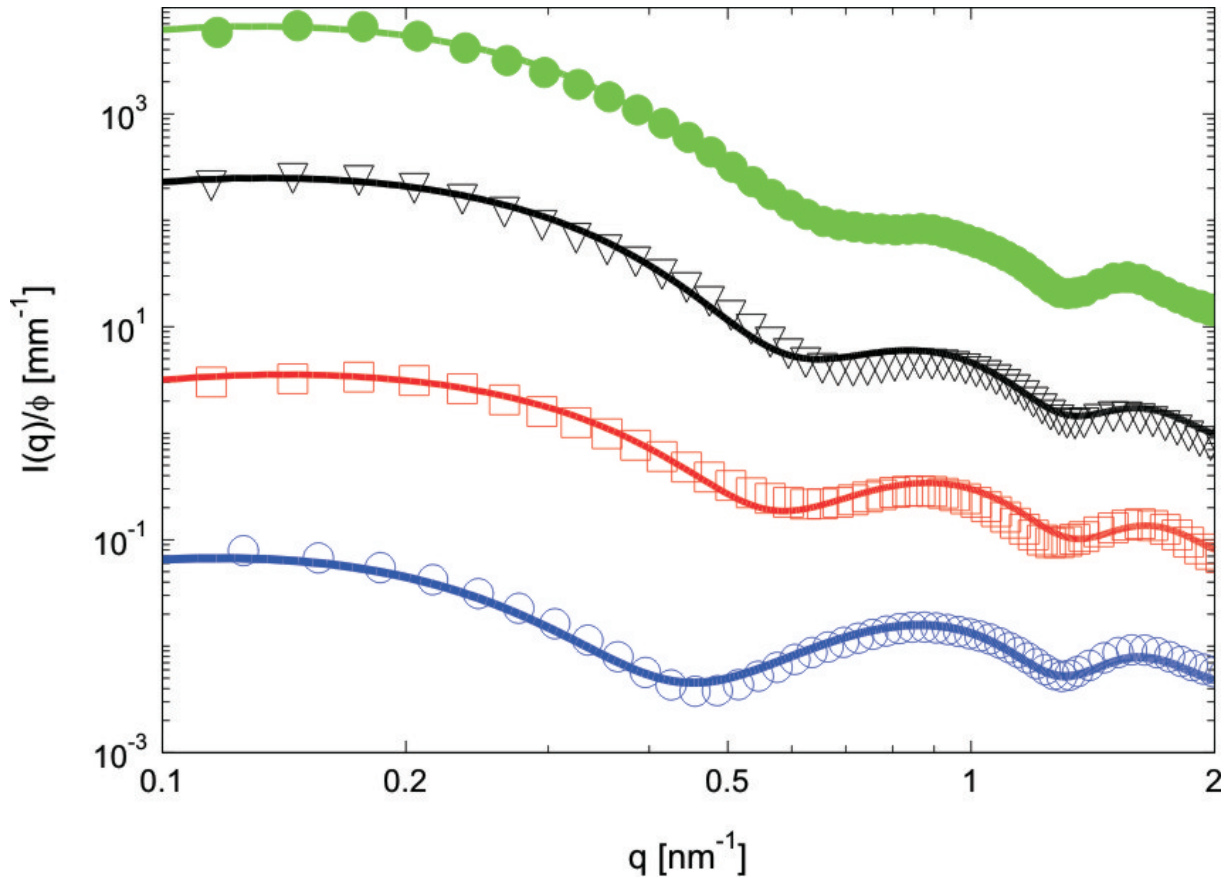
B.4 Influence of the annealing process on $\frac{N}{V}$



Normalized scattered intensities of the PE systems before (blue) and after (red) the heating procedure bathing in the highest glucose solutions. All intensities are normalized by the volume fraction of the sample: respectively 6.26 vol% and 6.96 vol% for the original and annealed particles. The volume fraction of the added D⁺-glucose are 14.25 vol% and 14.29 vol% respectively. The equality of the scattered intensities at low scattering vectors demonstrate that the number of particles per volume is constant before and after the annealing process.

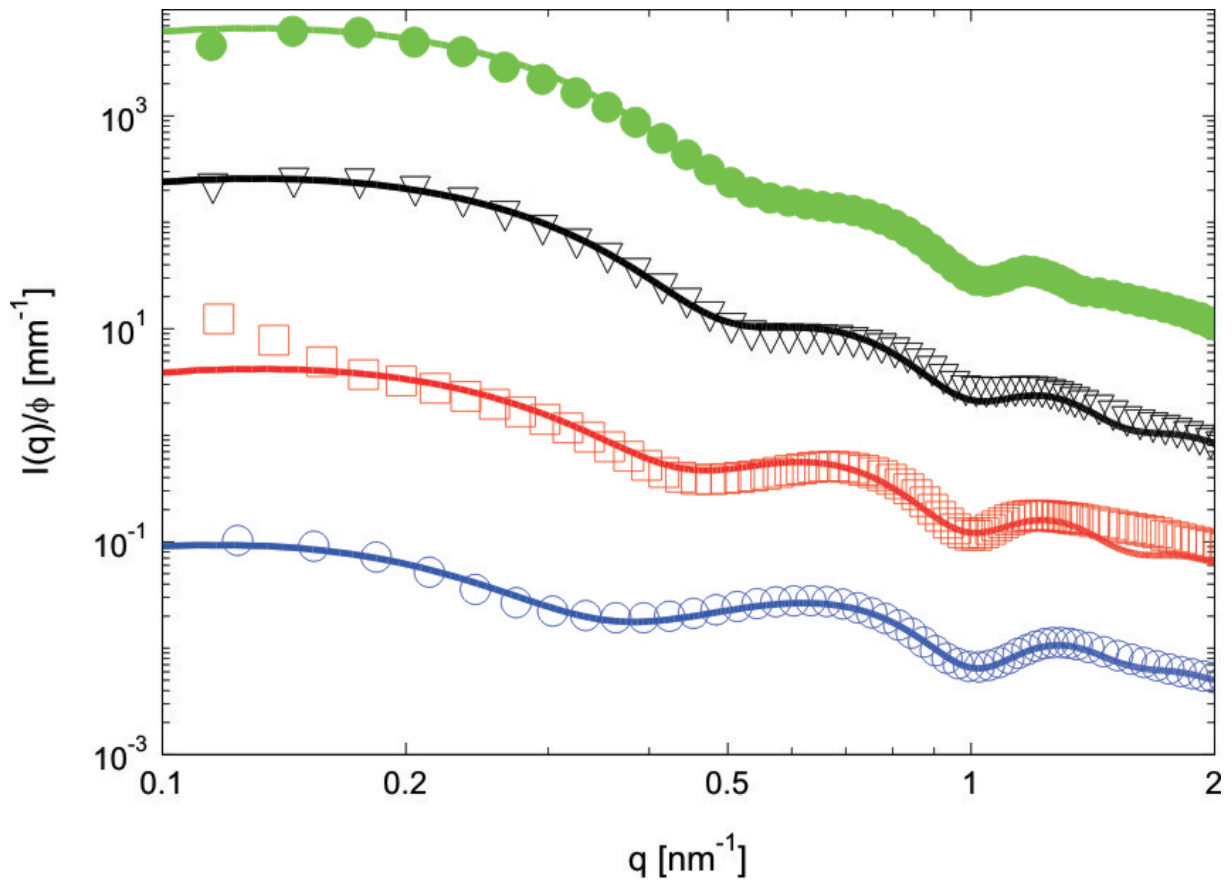
B.5 Contrast series of PL78

B.5.1 Original system - PL78



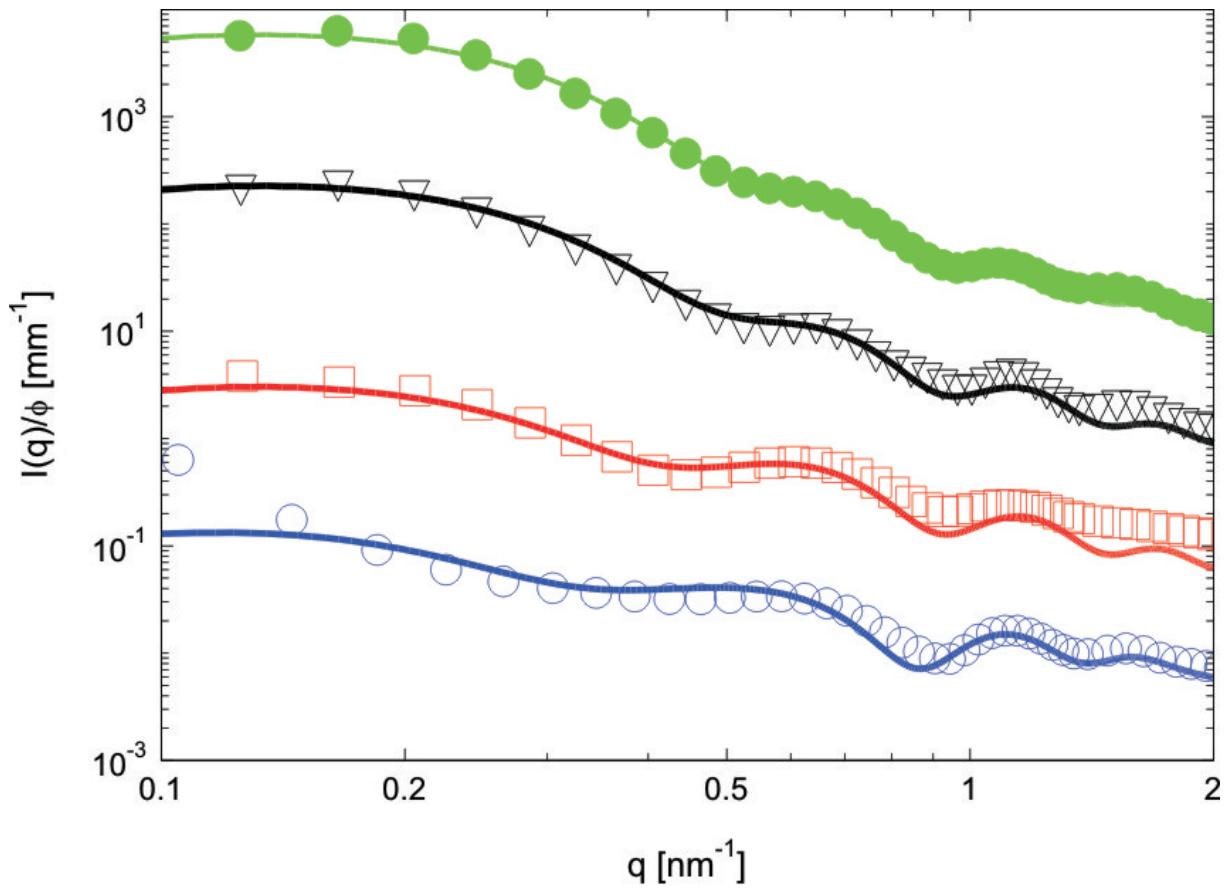
Experimental contrast variation SAXS data of the original PL78 system and their respective theoretical intensities according to equations 5.2 and 5.3 page 42. The volume percentages of the systems are from bottom to top: 2.1 vol%, 1.9 vol%, 1.8 vol% and 1.7 vol% and their respective volume percentages of added glucose are: 0.0 vol%, 4.4 vol%, 9.9 vol% and 15.0 vol%. The mean crystalline thickness measures here 6.5 nm.

B.5.2 System annealed at 90°C



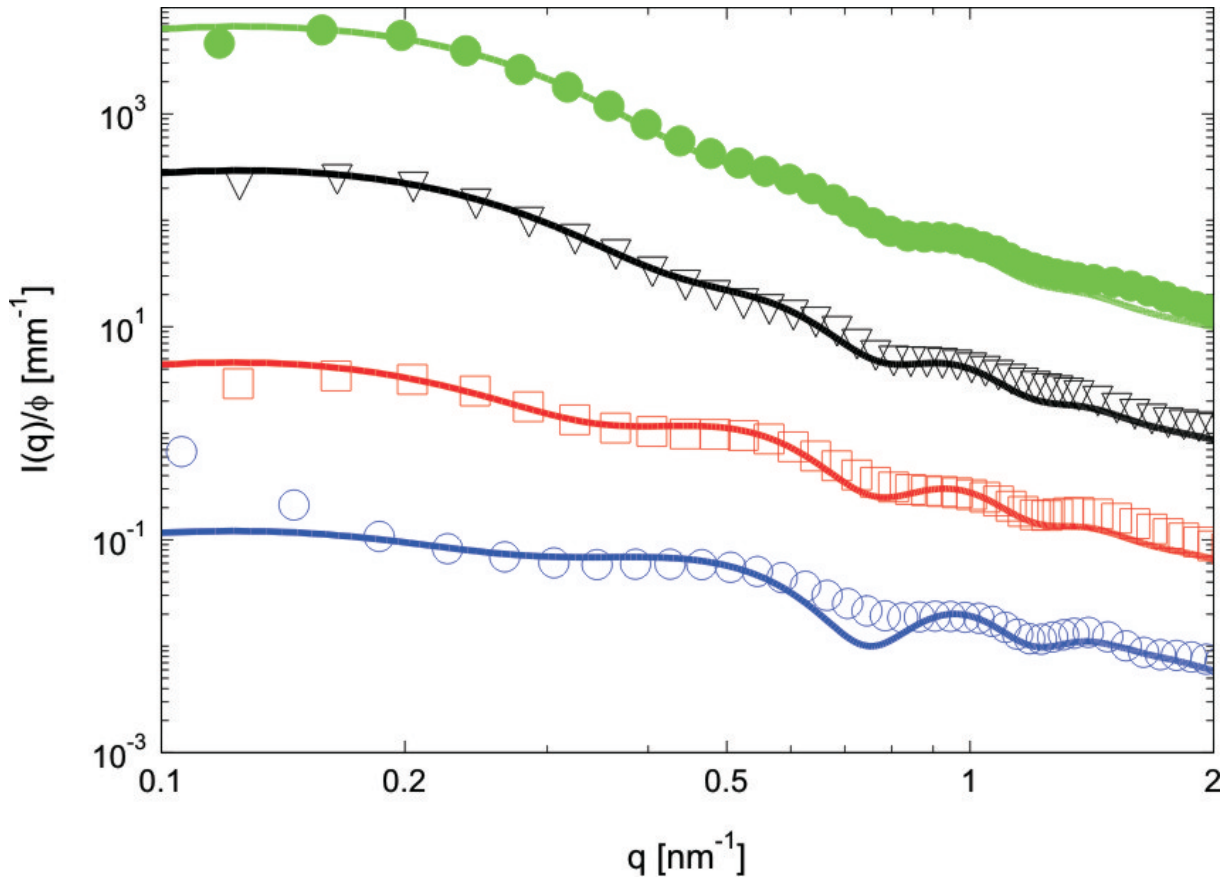
Experimental contrast variation SAXS data of the PL78 system annealed at 90°C and their respective theoretical intensities according to equations 5.2 and 5.3 page 42. The volume percentages of the systems are from bottom to top: 1.6 vol%, 1.5 vol%, 2.0 vol% and 1.9 vol% and their respective volume percentages of added glucose are: 0.0 vol%, 4.4 vol%, 9.9 vol% and 14.9 vol%. The mean crystalline thickness measures here 8.5 nm.

B.5.3 System annealed at 105°C



Experimental contrast variation SAXS data of the PL78 system annealed at 105°C and their respective theoretical intensities according to equations 5.2 and 5.3 page 42. The volume percentages of the systems are from bottom to top: 2.4 vol%, 2.2 vol%, 2.1 vol% and 2.0 vol% and their respective volume percentages of added glucose are: 0.0 vol%, 4.4 vol%, 9.9 vol% and 15.1 vol%. The mean crystalline thickness measures here 10.2 nm.

B.5.4 System annealed at 115°C



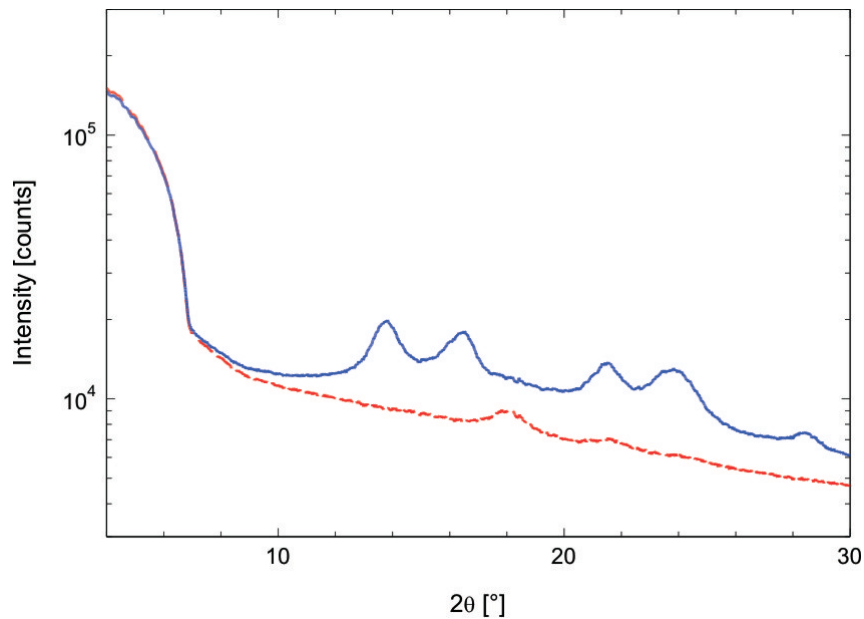
Experimental contrast variation SAXS data of the PL78 system annealed at 115°C and their respective theoretical intensities according to equations 5.2 and 5.3 page 42. The volume percentages of the systems are from bottom to top: 2.6 vol%, 2.4 vol%, 2.3 vol% and 2.1 vol% and their respective volume percentages of added glucose are: 0.0 vol%, 4.4 vol%, 9.9 vol% and 14.9 vol%. The mean crystalline thickness measures here 11.8 nm.

B.6 Synthesis of sPB

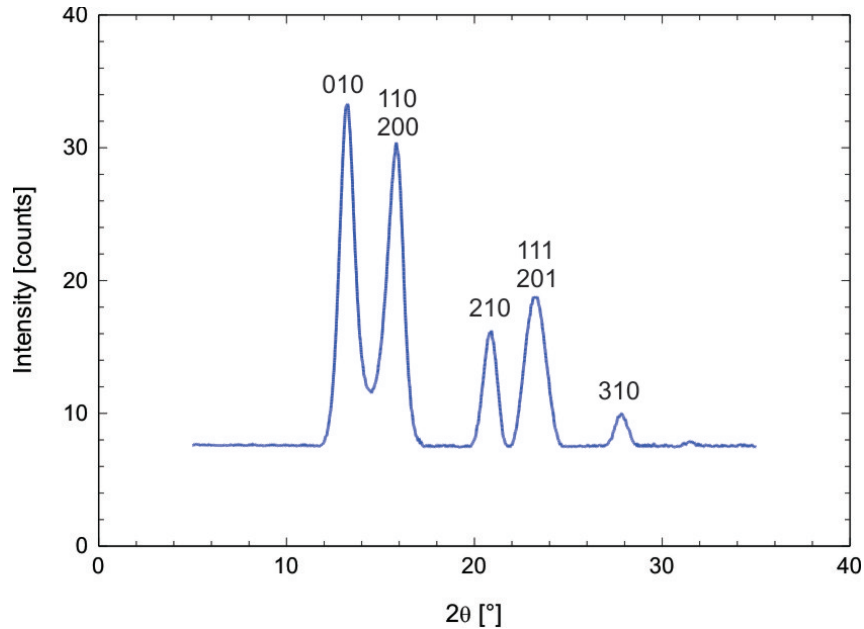
The synthesis of the nanoparticles were realized in Konstanz, Germany, by Dr. Brigitte Korthals.

A toluene solution (5 ml) of cobalt(II) 2-ethylhexanoate (1.60 mmol) was introduced under argon to a mechanically stirred 10 ml pressure glass reactor equipped with a heating/cooling jacket controlled by a temperature sensor dipping into the reaction mixture. After evaporating of toluene in vacuum, 32.5 g of butadiene were condensed at -5°C . An ethanol solution (15 ml) of sodium borohydride (3.55 mmol) was added, affording a solution of the precatalyst $[\text{Co}(\text{C}_8\text{H}_{13})(\text{C}_4\text{H}_6)]$. An aqueous solution of surfactant (46.5 g SDS/ 20 g pentanol and 400 g H_2O) was then transferred to the reactor by means of a pump under stirring (1000 rpm) and the temperature was set to 20°C , affording a transparent butadiene/precatalyst microemulsion. A toluene solution of carbon disulfide (1.6 mmol, $[\text{CS}_2] / [\text{Co}] = 1$) was pumped into the reactor, which was then rapidly heated to the desired temperature ($T = 40^{\circ}\text{C}$). After 3h the reaction was stopped by cooling and releasing residual gas pressure, affording a light brown transparent latex.

B.7 X-ray diffraction of BK280



X-ray diffraction of the polybutadiene system BK280 (blue full line) and of the glass substrate (red bold line).



X-ray diffraction of the polybutadiene system BK280 alone. This data were obtained by subtracting the signal of the glass and of the amorphous part. The hkl peak of the crystalline syndiotactic 1,2-polybutadiene (P_{acm} , $a=10.98$ Å, $b=6.60$ Å and $c=5.14$ Å) are reported when visible.

B.8 DLS of BK280

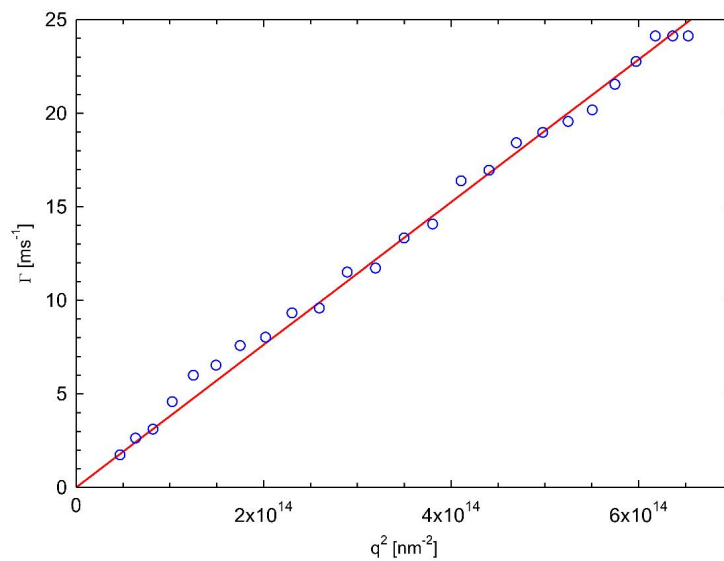
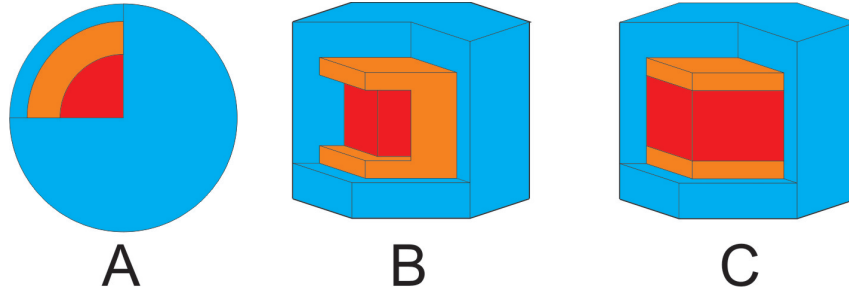


Figure B.1: DLS data of the polybutadiene system. The diffusion coefficient was determined to 3.81×10^{-23} m²/s leading to an hydrodynamic radius of 6.4 nm. The system was diluted in water at a concentration of 0.00013 wt%.

B.9 Models investigated for the SAXS-CV of BK280



Four different structural morphologies were investigated in order to model the SAXS contrast variation data of the polybutadiene system. A core bi-shell system (A), an hexagonal crystalline platelet surrounded by an amorphous layer of PB surrounded by SDS surfactant (B), an hexagonal crystalline platelet sandwiched between two amorphous layers of PB surrounded by SDS surfactant (C) and the model described in figure 5.1 page 43. For the latter model as well as model (B) and (C), the following theoretical equations describe the modeling of circular platelets. The difference in intensity between circular and hexagonal platelets of the same dimension are not significant. Since the C⁺⁺ program leading to the theoretical SAXS intensities of circular platelets is running faster than the one for hexagonal platelets, then only circular platelets have been used for the study of the polybutadiene and the polyethylene nanoparticles.

For case (A), the theoretical SAXS intensities $I_A(q)$ could be calculated according to:

$$I_A(q) = \frac{N}{V} \times F_A^2(q) \quad (\text{B.1})$$

with:

$$F_A(q) = 4\pi \left\{ \begin{array}{l} R_{sds}^3 \frac{\sin\{q(R_{sds})\} - \{q(R_{sds})\} \cos\{q(R_{sds})\}}{\{q(R_{sds})\}^3} (\rho_{sds} - \rho_{sol}) + \\ R_a^3 \frac{\sin\{q(R_a)\} - \{q(R_a)\} \cos\{q(R_a)\}}{\{q(R_a)\}^3} (\rho_{amo} - \rho_{sds}) + \\ R_c^3 \frac{\sin\{q(R_c)\} - \{q(R_c)\} \cos\{q(R_c)\}}{\{q(R_c)\}^3} (\rho_{amo} - \rho_{sds}) \end{array} \right\} \quad (\text{B.2})$$

where R_c is the radius of the crystalline core, $R_a = R_c + h_a$ (h_a , thickness of the amorphous layer) and $R_{sds} = R_a + h_{sds}$ (h_{sds} , thickness of the sds layer). ρ_{cry} , ρ_{amo} , ρ_{sds} and ρ_{sol} denote respectively the electron densities of the crystalline, amorphous, sds and solvent phases.

For case (B), the theoretical SAXS intensities $I_B(q)$ could be calculated according to:

$$I_B(q) = \frac{N}{V} \int_0^{\pi/2} [F_B(q, \alpha)]^2 \sin(\alpha) d\alpha \quad (\text{B.3})$$

$$F_B(q, \alpha) = 2\pi \left\{ \begin{array}{l} R_{sds}^2 \frac{2J_1(qR_{sds} \sin(\alpha))}{qR_{sds} \sin(\alpha)} \frac{\sin(qL_{sds} \cos(\alpha)/2)}{q \cos(\alpha)/2} (\rho_{sds} - \rho_{sol}) + \\ R_a^2 \frac{2J_1(qR_a \sin(\alpha))}{qR_a \sin(\alpha)} \frac{\sin(qL_a \cos(\alpha)/2)}{q \cos(\alpha)/2} (\rho_{amo} - \rho_{sds}) + \\ R_c^2 \frac{2J_1(qR_c \sin(\alpha))}{qR_c \sin(\alpha)} \frac{\sin(qL_c \cos(\alpha)/2)}{q \cos(\alpha)/2} (\rho_{amo} - \rho_{sds}) \end{array} \right\} \quad (\text{B.4})$$

where R_c , R_a , R_{sds} , ρ_{cry} , ρ_{amo} , ρ_{sds} and ρ_{sol} are defined as in model (A) and L_c is the thickness of the crystalline phase, $L_a = L_c + h_a$ (h_a , thickness of one amorphous layer) and $L_{sds} = L_a + h_{sds}$ (h_{sds} , thickness of one sds layer).

For case (C), the theoretical SAXS intensities $I_C(q)$ could be calculated according to:

$$I_C(q) = \frac{N}{V} \int_0^{\pi/2} [F_C(q, \alpha)]^2 \sin(\alpha) d\alpha \quad (\text{B.5})$$

$$F_C(q, \alpha) = 2\pi \left\{ \begin{array}{l} R_{sds}^2 \frac{2J_1(qR_{sds} \sin(\alpha))}{qR_{sds} \sin(\alpha)} \frac{\sin(qL_{sds} \cos(\alpha)/2)}{q \cos(\alpha)/2} (\rho_{sds} - \rho_{sol}) + \\ R_a^2 \frac{2J_1(qR_a \sin(\alpha))}{qR_a \sin(\alpha)} \frac{\sin(qL_a \cos(\alpha)/2)}{q \cos(\alpha)/2} (\rho_{amo} - \rho_{sds}) + \\ R_c^2 \frac{2J_1(qR_c \sin(\alpha))}{qR_c \sin(\alpha)} \frac{\sin(qL_c \cos(\alpha)/2)}{q \cos(\alpha)/2} (\rho_{amo} - \rho_{sds}) \end{array} \right\} \quad (\text{B.6})$$

where R_c , R_a , R_{sds} , ρ_{cry} , ρ_{amo} , ρ_{sds} , ρ_{sol} , L_c , L_a and L_{sds} are defined as in model (B).

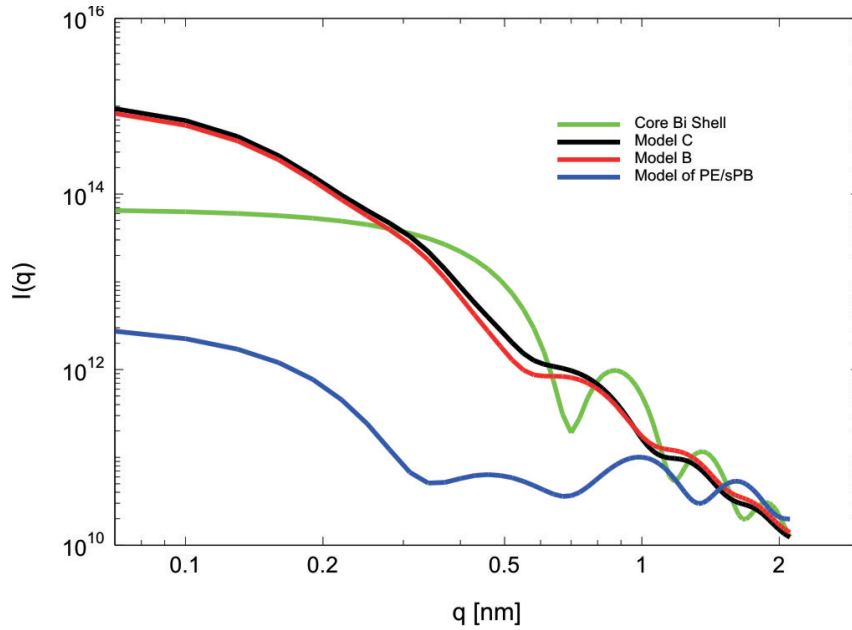


Figure B.2: Theoretical SAXS signal of the different structural models. The intensities resulting from models B and C do not lead to any drastical change of the SAXS intensities while the model used in this study as well as the core-bishell model do lead to a stronger change in intensities at small q -values. For the model used in this study, "model PE/sPB", the parameters used are: $R = 12.0 \pm 2.0$ nm, $L_c = 6.5 \pm 0.4$ nm, $L_a = 3.1 \pm 0.8$ nm and $L_{sds} = 2.0$ nm. For model B: $R = 12.0 \pm 2.0$ nm, $R_a = R - 2.0$ nm (R_a denotes the radius of the amorphous phase alone), $R_c = R_a - \frac{1}{2}L_a$ (R_c denotes the radius of the crystalline phase alone) $L_c = 6.5 \pm 0.4$ nm, $L_a = 3.1 \pm 0.8$ nm and $L_{sds} = 2.0$ nm. For model C: $R = 12.0 \pm 2.0$ nm, $R_a = R - 2.0$ nm (R_p denotes the radius of the polymer phase alone), $L_c = 6.5 \pm 0.4$ nm, $L_a = 3.1 \pm 0.8$ nm and $L_{sds} = 2.0$ nm. For the core bi-shell model: $R_c = 6.5 \pm 0.4$ nm, $h_a = 3.1 \pm 0.8$ nm and $h_{sds} = 2.0$ nm. For all models in this appendix, the electron densities have the following values: $333.57 \text{ e.u. nm}^{-3}$, 339 e.u. nm^{-3} , 302 e.u. nm^{-3} and 397 e.u. nm^{-3} respectively for the solvent, crystalline, amorphous and sds phase.

List of Figures

2.1	Basic principle of the diffraction phenomenon. An incident ray, produced by an X-ray source X, strikes a sample S. A detector D records an ensemble of intensities scattered at different angles θ	10
2.2	Determination of the phase difference between two scattering centers A and B in a particle. \vec{S} and \vec{S}_0 represent the unit vectors in the direction of scattered and incident beam respectively. θ is the scattering angle and \vec{q} the scattering vector.	11
2.3	Schematic representation of the contrast variation. Different electron densities of the solvent help to detect substructures of the system. This method permits then to study the total structure and the different phases present in the analyzed particles in detail. $\Delta\rho$ defines the electron contrast of the studied system relative to the medium.	16
3.1	Model of the three domains of Fetuin-A. D1 and D2 remain of the Cystatin Superfamily while D3 has a structural homolgy with an insertion domain. Picture taken from reference [63].	19
3.2	Hypothetical model of a calciprotein particle (CPP) consisting of aggregated calcium-phosphate-Fetuin complexes. Figure taken from reference [64].	19
3.3	Radiological analysis of 9-months-old mice. The mouse in the right is genetically deficient in Fetuin-A production while the one on the left is a wild type mouse. The lack of Fetuin-A is characterized by a strong calcification in extracelular space. Picture taken from reference [72].	20
3.4	Schematical representation of syndiotactic 1,2-poly(1,3-butadiene). We note a regular alternation of the CH-CH ₂ bond behind and before the plane of the acyl chain.	21
3.5	Schematical representation of sharp- and tight-folded chains of crystalline polymers.	22
3.6	Schematic growth of a nascent PE nanocrystal. The faces 100 disappear as they grow faster than the 110 (left), resulting to a lozenge shape (right). The letter G refers to the growth along the face.	23

3.7	Thermodynamic scheme of polymer crystals proposed in literature [34]. n defines the number of structure unit per crystalline chain, see text for further explanations. This scheme is still under debate especially the pathway from point 2 to 3.	24
4.1	Time-resolved turbidimetry measurements indicating that the inhibition mixes were stable down to a concentration of $7 \mu\text{M}$ Fetuin-A. The stability of primary CPPs correlated with the Fetuin-A concentration. Figure taken from reference [17].	27
4.2	Extraction of the data from the measured SAXS scattering intensities according to equation 4.1: After subtraction of the signal due to the capillary (green plus), the intensity of the buffer (black triangle) is subtracted depending on the volume fraction of the sample (blue circle). This results to the red squares.	29
4.3	Influence of the weight fraction of calcium and phosphate ions onto the size of the primary CPPs. The ration of Ca/P is constant and equals to 10/6. The concentration of calcium ions in the mix are $3.6 \mu\text{M}$ (black triangles), $5.0 \mu\text{M}$ (red squares) and $10 \mu\text{M}$ (blue circles).	30
4.4	Evolution of the SAXS intensities with time in the absence of Fetuin-A at the very early stage. The growth in intensity is characteristic of the nucleation phase, <i>id est</i> , the formation of the first precursor particles. The time point of measurement is reported in the legend.	31
4.5	Time-evolution of the intensities collected at $q=0.25 \text{ nm}^{-1}$ for the earliest SAXS intensities collected. The formation of the primary particles follows a kinetic of first order. The kinetic constant k is directly proportionnal to the slope and is decreasing with the amount of Fetuin-A. Data collected for the system without added protein (blue) is compared to the systems including $1 \mu\text{M}$ (red), $5 \mu\text{M}$ (black) and $15 \mu\text{M}$ (green) of Fetuin-A.	32
4.6	Influence of Fetuin-A onto the size of the CPPs. The DLS setup was thermostated at 37°C and 1.8 mL of calcium solution (with the appropriate concentration of Fetuin-A) was inserted in a glass cell. A solution of phosphate ions was as well thermostated at 37°C and 0.2 mL of this solution were inserted in the cell. The solution was then mixed by hand and the DLS measurements started ca. 30 seconds after the mixing process. The final concentration of calcium and phosphate ions was respectively 10 mM and 6 mM. The system without added protein (dark blue) is compared to the ones with $1 \mu\text{M}$ (red), $5 \mu\text{M}$ (black), $15 \mu\text{M}$ (green) and $30 \mu\text{M}$ (light blue) of Fetuin-A.	33

4.7	DLS measurements of CPPs obtained by mixing 10 mM of Ca^{2+} with 6 mM of PO_4^{3-} . The influence of the addition of 4 μM of Fetuin-A (red) is well highlighted compared to the system without added protein (blue).	34
4.8	TEM micrograph of a sample obtained by mixing 20 mM of Ca^{2+} with 12 mM of HPO_4^{2-} without addition of Fetuin-A (left) and in presence of 15 μM of the glycoprotein (right).	35
4.9	Evolution of the SAXS intensities with time in the absence of Fetuin-A. Later SAXS intensities did not show any evolution of the shape or the intensity. This underlines the very fast kinetic of early calcification leading to the first equilibrium phase of calcium phosphate particles. Time point of measurements are: 0.035 s (blue), 0.255 s (red) and 1.355 s (green) after the mixing process.	36
4.10	Evolution of the SAXS intensities with time in the absence (top) and in presence of 15 μM (bottom) of Fetuin-A. Later SAXS intensities did not show any evolution of the shape or the intensity. This demonstrates the very fast kinetic of early calcification leading to the first equilibrium phase of calcium phosphate particles. Time point of measurements are: 0.035 s (blue circles), 0.255 s (red squares), 0.695 s (black triangles) and 6.415 s (blue squares) after the mixing process.	37
4.11	Experimental data of measured samples and their respective fits 0.89 second after the mixing process. The points represent the experimental data. For the sake of clarity, only one out of two points is reproduced. The dashed lines exhibit the theoretical fits of polydisperse homogenous non interacting spheres, including the thermal fluctuations and the full lines reflect the complete fit when the structure factor is needed. The graphic shows the different concentrations studied: 0 μM , 1 μM , 5 μM and 15 μM of Fetuin-A from bottom to top.	38
4.12	Evolution of the structure factor $S(q)$ obtained from the modelling of the SAXS data recorded 0.89 s after the mixing process. The up-turn at small q-values characterizes the aggregation of the nanoparticles. Mixes contain 0 μM (blue), 1 μM (red), 5 μM (black) and 15 μM (green) of Fetuin-A.	38
4.13	Time-evolution of the radius of the primary spherical particles of calcium phosphate as a function of the concentration of the protein. The primary spherical particles grow with a very fast kinetic within 1 s for all samples studied. The dashed lines are guide lines for the evolution of the radius of the primary spherical particles. Data involving a concentration of 1 μM of Fetuin-A are not reproduced for the sake of clarity and is intermediate to the one of 0 and 5 μM	39

4.14	Time-evolution of the number of primary spherical particles per aggregate ($S(0)+1$). The main effect of Fetuin-A is seen here: inhibition of the aggregation. The dashed lines are guide lines for the evolution of the parameters. Mixes contain 0 μM (blue), 1 μM (red), 5 μM (black) and 15 μM (green) of Fetuin-A.	39
4.15	Binding of the D1 domain of Fetuin-A onto the surface of hydroxyapatite. The positive charges of Ca^{2+} are marked in blue and the negative phosphate charges are represented in red. Figure taken from reference [63].	40
5.1	Hamburger model used in this study. Two additional sheets of SDS have to be taken into account to model the structure. L_t , $L=L_c+L_a$ and L_c represent the thicknesses of the whole particle, of the polymer and of the crystalline phase respectively, while R is the radius of the disk.	43
5.2	Cryo-TEM image of the nanoparticle of polybutadiene. The concentration was 0.03 wt%. The scale bar of the main micrograph represents 50 nm while the ones in the insets represent 10 nm.	44
5.3	Normalized scattering intensities of the polybutadiene nanoparticles. For the sake of clarity, the four lowermost scattered intensities were divided by factor of 10^1 , 10^2 , 10^3 and 10^4 . From bottom to top, the concentration of glucose (and of the sample) in solution was 0.0 (1.19), 3.2 (1.23), 6.5 (1.24), 9.8 (1.24) and 17.3 (1.32) vol%.	45
5.4	Plot of the temperature as a function of the reciprocal of the crystalline thickness of syndiotactic polybutadiene systems. The red squares are obtained from reference [119] and the blue circle represents this study. The bold red and blue lines are guide-lines for the recrystallization and crystallization lines respectively.	46
6.1	Typical cryo-TEM micrographs of the original PL39 system (top) and of the annealed PL39 sample (bottom). Insets in each micrograph presents a single particle in which the direction of the main axis is orthogonal and parallel to the direction of the electron beam. The annealing process was carried at 125°C for 20 minutes. For both micrographs, the weight percentage studied is 0.3 wt%.	49

6.2	Normalized scattered intensities of the PL39 PE system before (top) and after (bottom) the annealing procedure. All intensities are normalized by the volume fraction of the sample. The volume fraction of the contrast agent varies from 0 (blue points), 0.04 (red points), 0.10 (black points) up to 0.14 (green points), while the volume fraction of the nanoparticles decrease: 2.5, 2.4, 2.3, 2.2 vol% for the original system (top) and 2.6, 2.5, 2.3 and 2.2 vol% for the annealed sample (bottom) respectively. The three lowermost intensities are divided by factors of 10, 10^2 and 10^3 for sake of clarity. The vertical gray dashed lines show the q-value below which the structure factor is needed. For the sake of clarity, only one out of 5 points is shown. The dashed lines represents the result of the modeling of the SAXS data assuming a dispersion of non-interacting polydisperse platelets. The solid lines represent the scattering intensity calculated for a dispersion of interacting polydisperse platelets.	51
6.3	2D-model of the unlooping process expected by some authors [106,120–122]. (a): The full unlooping process of one single crystalline nanoparticle lead to a doubling of the crystalline thickness of the same particle. (b): The stack of two crystalline particles lead to one particle with a doubled crystalline thickness.	53
6.4	Cryo-TEM micrographs of PL78 sample (original and different annealed temperatures). The black bar represents 50 nm.	54
6.5	Two-dimensional schematical representation of partial unlooping of PE chains within a nanoparticle. A partial unlooping leads to a very small decrease of the radius R of the platelet, probably a decrease too small to be detected by SAXS experiments.	54
6.6	Experimental data and corresponding fits of the original sample PL78 dispersed in pure water (blue circles). The volume fractions of the systems are: 2.1 vol%, 1.6 vol%, 2.4 vol% and 2.6 vol% respectively for the original system (bottom) and the ones annealed at 90°C (red squares), 105°C (black triangles) and 115°C (green circles).	55
6.7	Experimental data of the reciprocal of the crystalline thickness depending on the annealing temperature. The data with triangular and square symbols have been obtained from micron crystals originally crystallized at $T=85^\circ\text{C}$ and $T=95^\circ\text{C}$ respectively [123]. The blue circles represent the data of this study (nanocrystals freely suspended).	56

6.8	Experimental thermodynamic scheme obtained by the help of data in reference [124] (blue circles) and from the present study (red squares). The blue, red and black lines represent respectively the crystallization, recrystallization and melting lines of the thermodynamic scheme proposed in literature [29,94]. The bold green line is a guide line for the post-thickened experimental data points [123].	57
7.1	Schematic representation of the USAXS/SAXS/WAXS equipment at the ERSF in Grenoble, France. Picture taken from http://www.esrf.eu/UsersAndScience/Experiments/SoftMatter/ID02/BeamlineLayout on July, the 1 st 2009.	59
7.2	Determination of the density of a calcium phosphate system in buffer solution. From the slope, ρ is determined to 1.67 ± 0.05 g/cm ³	60
8.1	Hypothetical model of the influence of Fetuin-A (red) onto the formation of calcium phosphate complexes (orange). Black and white images on the right present TEM micrographs of calcium-phosphate particles formed without (bottom) and in presence of 15 μ M of Fetuin-A (top).	62
8.2	Schematical resume of the experiments realized onto the PE nanoparticles annealed at different temperatures. T is the temperature and n is the number of monomer units in the crystalline thickness.	63
9.1	Vorgeschlagenes Modell des Einflusses von Fetuin-A (rot) auf die Bildung von Calciumphosphat-Teilchen (orange). Die Bilder auf der rechten Seite zeigen TEM-Aufnahmen der Calciumphosphat-Komplexen, die ohne (unten) und mit 15 μ M Fetuin-A (oben) gebildet wurden.	65
9.2	Schematische Zusammenfassung der Experimente mit PE-Nanopartikeln und verschiedenen Tempertemperaturen.	66
B.1	DLS data of the polybutadiene system. The diffusion coefficient was determined to 3.81×10^{-23} m ² /s leading to an hydrodynamic radius of 6.4 nm. The system was diluted in water at a concentration of 0.00013 wt%.	88

B.2 Theoretical SAXS signal of the different structural models. The intensities resulting from models B and C do not lead to any drastical change of the SAXS intensities while the model used in this study as well as the core-bishell model do lead to a stronger change in intensities at small q-values. For the model used in this study, "model PE/sPB", the parameters used are: $R = 12.0 \pm 2.0$ nm, $L_c = 6.5 \pm 0.4$ nm, $L_a = 3.1 \pm 0.8$ nm and $L_{sds} = 2.0$ nm. For model B: $R = 12.0 \pm 2.0$ nm, $R_a = R-2.0$ nm (R_a denotes the radius of the amorphous phase alone), $R_c = R_a - \frac{1}{2}L_a$ (R_c denotes the radius of the crystalline phase alone) $L_c = 6.5 \pm 0.4$ nm, $L_a = 3.1 \pm 0.8$ nm and $L_{sds} = 2.0$ nm. For model C: $R = 12.0 \pm 2.0$ nm, $R_a = R-2.0$ nm (R_p denotes the radius of the polymer phase alone), $L_c = 6.5 \pm 0.4$ nm, $L_a = 3.1 \pm 0.8$ nm and $L_{sds} = 2.0$ nm. For the core bi-shell model: $R_c = 6.5 \pm 0.4$ nm, $h_a = 3.1 \pm 0.8$ nm and $h_{sds} = 2.0$ nm. For all models in this appendix, the electron densities have the following values: 333.57 e.u.nm⁻³, 339 e.u.nm⁻³, 302 e.u.nm⁻³ and 397 e.u.nm⁻³ respectively for the solvent, crystalline, amorphous and sds phase. 91

Acknowledgements

First of all, I would like to express my deepest gratitude to Prof. Dr. M. Ballauff for giving me the interesting subjects that I have been investigating. I would like to thank him for being very helpful for the publications and this thesis.

I am very grateful to Prof. Dr. W. Jahnen-Dechent and Prof. Dr. S. Mecking for their helpful discussions and for kindly providing samples during our collaborations.

Many thanks are given to Dr. Sabine Rosenfeldt for her critical readings of my works and especially this thesis. I give my acknowledgement to Dr. Alexander Heiss for all valuable discussions about the calcification project and to Priv.-Doz. Dr. Ludger Harnau for his outstanding contribution to the simulation work on interparticle interactions of the polyethylene nanoparticles. Dr. Markus Drechsler is acknowledged for his great investigations by electron microscopies on the different samples that I studied.

I am very grateful to Dr. Jérôme Crassous for his daily good mood and for our valuable discussions at any time. I would like to thank him as well for the very interesting project that we have been investigating together.

I am grateful to all my colleagues who have constructed a very friendly atmosphere for working. I give my acknowledgements especially to Adriana and Sergio Mihut for their help during the study of the polyethylene nanoparticles and for giving me some piece of advice for the programming of the fitting programs respectively. I would like to thank, Dr. Katja Henzler for realizing the SAXS experiments of the first polyethylene sample at the ESRF, Grenoble, France. A very big thanks is given to Dr. Theyencheri Narayanan for providing beam time at the Synchrotron source for all studied systems. Qiong Tong is greatly thanked for the synthesis of the PE nanoparticles and for all important discussions for a better understanding of these objects. I treasure my friendship with my colleagues Frank Polzer, Christian Schneider, Michael Zeiser, Dr. Yan Lu, Dr. Alexander Wittemann, Miriam Siebenbürger and Dr. Sreenath Bolisetty.

I thank Elisabeth Dünfelder for her bureaucratic work with a lot of patience and kindness and Karlheinz Lautenbach for his availability and technical support.

My special thanks goes to my family. My parents have encouraged me and shown their appreciations for my every progress in these works. I am very grateful too to my brothers for kindly giving me the opportunity to use unix servers for simulating SAXS theoretical intensities and for their encouragements.

Financial support by the Deutsche Forschungsgemeinschaft, SFB 481, Bayreuth, and by the Marie Curie Research Training Network (POLYAMPHI) are gratefully acknowledged.

Bibliography

- [1] Fajun Zhang, Maximilian W. A. Skoda, Robert M. J. Jacob, Richard A. Martin, Christopher M. Martin, and Frank Schreiber. Protein interactions studied by saxs: Effect of ionic strength and protein concentration for bsa in aqueous solutions. *Journal of Physical Chemistry B*, 111 (1):251–259, 2007.
- [2] D. Pontoni, T. Narayanan, and A. R. Rennie. Tr-saxs study of nucleation and growth of silica colloids. *Langmuir*, 18:56–59, 2002.
- [3] G. MacLennan and C. A. Beevers. The crystal structure of dicalcium phosphate, CaHPO_4 . *Acta Cryst*, 8:579–583, 1955.
- [4] C. A. Beevers. The crystal structure of dicalcium phosphate dihydrate, $\text{CaHPO}_4 \cdot 2\text{H}_2\text{O}$. *Acta Cryst*, 11:273–277, 1958.
- [5] K. Sudarsanan and R. A. Young. Structure of strontium hydroxide phosphate, $\text{Sr}_5(\text{PO}_4)_3\text{OH}$. *Acta Cryst*, 28:3668–3670, 1972.
- [6] J. D. Termine and A. S. Posner. Calcium phosphate formation in vitro. *Archives of Biochemistry and Biophysics*, 140:307–317, 1970.
- [7] J. L. Meyer and E. D. Eanes. A thermodynamic analysis of the amorphous to crystalline calcium phosphate transformation. *Calcified Tissue Research*, 25:59–68, 1978.
- [8] Hans E. Lundager-Madsen, Isabel Lopez-Valero, Victoria Lopez-Acevedo, and Roland Boistelle. The formation product of amorphous tricalcium phosphate at 37°C . *Journal of Crystal Growth*, 75:429–434, 1986.
- [9] F. Betts, N. C. Blumenthal, and A. S. Posner. Bone mineralization. *Journal of Crystal Growth*, 53:63–73, 1981.
- [10] M. U. Nysten, E. D. Eanes, and J. D. Termine. Molecular and ultrastructural studies of non-crystalline calcium phosphates. *Calcified Tissue Research*, 2:95, 1972.
- [11] Lj. Brecevic and H. Fiedler-Milhofer. Precipitation of calcium phosphates from electrolyte solutions. *Calcified Tissue Research*, 10:82–90, 1972.

-
- [12] J. Bolze, B. Peng, N. Dingenouts, P. Panine, T. Narayanan, and M. Ballauff. Formation and growth of amorphous colloidal CaCO_3 precursor particles as detected by tr-saxs. *Langmuir*, 18:8364–8369, 2002.
- [13] J. Bolze, D. Pontoni, M. Ballauff, T. Narayanan, and H. Cölfen. Time-resolved saxs study of the effect of a double hydrophilic block-copolymer on the formation of CaCO_3 from supersaturated salt solution. *Journal of Colloid and Interface Science*, 277:84–94, 2004.
- [14] Willi Jahnen-Dechent, Andreas Trindl, Jasmina Godovac-Zimmermann, and Werner Müllner-Esterl. Posttranslational processing of human fetuin (human fetuin) - evidence for the production of a phosphorylated single-chain form by hepatoma cells. *European Journal of Biochemistry*, 226:59–69, 1994.
- [15] Willi Jahnen-Dechent, C. Schiffrin, A. Heiss, and J. Grötzinger. Systemic inhibition of spontaneous calcification by the serum protein fetuin. *Zeitschrift für Kardiologie*, 90:47–56, 2001.
- [16] A. Heiss, W. Jahnen-Dechent, H. Endo, and D. Schwahn. Structural dynamics of a colloidal protein-mineral complex bestowing on calcium phosphate a high solubility in biological fluids. *Biointerphases*, 2(1):16–20, 2007.
- [17] Alexander Heiss, Thomas Eckert, Anke Aretz, Walter Richtering, Wim van Dorp, Cora Schiffrin, and Willi Jahnen-Dechent. Hierarchical role of fetuin-a and acidic serum proteins in the formation and stabilization of calcium phosphate particles. *Journal of Biological Chemistry*, 283(21):14815–14825, 2008.
- [18] J.-P. Lin, C.-Y. Chang, C.-H. Wu, and S.-M. Shih. Thermal degradation kinetics of polybutadiene rubber. *Polymer Degradation and Stability*, 53:295, 1996.
- [19] P. T. Williams and S. Besler. Pyrolysis-thermogravimetric analysis of tyres and tyre components. *Fuel*, 74:1277, 1995.
- [20] B. Korthals, M. C. Morant-Minana, M. Schmid, and S. Mecking. Functionalization of polymer nanoparticles by thiol-ene addition. *Macromolecules*, 43:8071, 2010.
- [21] T. Yamamoto. Molecular dynamic of reversible and irreversible melting in chain-folded crystals of short polyethylene-like polymer. *Macromolecules*, 43:9384–9393, 2010.
- [22] Andrzej Pawlak and Andrzej Galeski. Cavitation during tensile drawing of annealed high density polyethylene. *Polymer*, 51:5771–5779, 2010.
- [23] A. Galeski, Z. Bartczak, T. Kazmierczak, and M. Slouf. Morphology of undeformed and deformed polyethylene lamellar crystals. *Polymer*, 51:5780–5787, 2010.

-
- [24] Courtney P. Ennis and Ralf I. Kaiser. Mechanistical studies on the electron-induced degradation of polymers: polyethylene, polytetrafluoroethylene, and polystyrene. *Physical Chemistry Chemical Physics*, 12:14884–14901, 2010.
- [25] S. C. Moyses. Low temperature annealing in low density polyethylene. saxs and dsc studies. *Polymer Journal*, 32:486–491, 2000.
- [26] Si₂verine Humbert, Olivier Lame, Jean-Marc Chenal, Cyrille Rochas, and Gi₂rard Vigier. Small strain behavior of polyethylene: In situ saxs measurements. *Journal of Polymer Science, Part B: Polymer Physics*, 48:1535–1542, 2010.
- [27] M. Kakiage, M Sekiya, T. Yamanobe, T. Komoto, S. Sasaki, S. Murakami, and H. Uehara. In situ saxs analysis of extended-chain crystallization during melt-drawing of ultra-high molecular weight polyethylene. *Polymer*, 48:7385–7392, 2007.
- [28] N. Stribeck, A. Almendarez Camarillo, U. Ni₂chel, P. Bi₂secke, and R. K. Bayer. Early oriented isothermal crystallization of polyethylene studied by high-time-resolution saxs/waxs. *Analytical and Bioanalytical Chemistry*, 387:649–661, 2007.
- [29] G: Strobl. A thermodynamic scheme treating polymer crystallization and melt. *European Physical Journal E*, 18:295–309, 2005.
- [30] R. Soula, C. Novat, A. Tomov, R. Spitz, J. Claverie, X. Drujon, J. Malinge, and T. Saudemont. Catalytic polymerization of ethylene in emulsion. *Macromolecules*, 34:2022–2026, 2001.
- [31] Florian M. Bauers and Stefan Mecking. High molecular mass polyethylene aqueous latexes by catalytic polymerization. *Angewandte Chemie International Edition*, 40(16):3020–3022, 2001.
- [32] Florian M. Bauers and Stefan Mecking. Wi₂ssrige latices aus hochmolekularem polyethylen durch katalytische polymerisation. *Angewandte Chemie*, 113(16):3112–3115, 2001.
- [33] C. H. M. Weber, A. Chiche, G. Krausch, S. Rosenfeldt, M. Ballauff, L. Harnau, I. Gi₂ttker-Schnetmann, Q. Tong, and S. Mecking. Single lamella nanoparticles of polyethylene. *Nano Letters*, 7 (7):2024–2029, 2007.
- [34] G. Strobl. Colloquium: Laws controlling crystallization and melting in bulk polymers. *Reviews of modern physics*, 81:1287–1300, 2009.
- [35] P. Debye and A. M. Bueche. Scattering by an inhomogeneous solid. *Journal of Applied Physics*, 20:518–525, 1949.

-
- [36] Andre Guinier. *Small-Angle Scattering X-rays*. John Wiley & Sons, 1955.
- [37] G. Fournet. Theoretical and experimental study of the diffusion of x-rays by dense aggregates of particles. *Bulletin de la Soci  t   ti  t   Francaise de Mineralogie et de Cristallographie*, 74:37–17, 1951.
- [38] H. E. Stanley. *Introduction to phase transitions and critical phenomena*. Clarendon Press, 1971.
- [39] B. B. Mandelbrot. *The Fractal Geometry of Nature*. Freeman, 1983.
- [40] H. C. Andersen and D. Chandler. Optimized cluster expansions for classical fluids. i. general theory and variational formulation of the mean spherical model and hard sphere percus-yevick equations. *Journal of Chemical Physics*, 57:1918, 1972.
- [41] D. Chandler and H. C. Andersen. Optimized cluster expansions for classical fluids. ii. theory of molecular liquids. *Journal of Chemical Physics*, 57:1930, 1972.
- [42] D. Chandler. Derivation of an integral equation for pair correlation functions in molecular fluids. *Journal of Chemical Physics*, 59:2742, 1973.
- [43] L. J. Lowden and D. Chandler. Solution of a new intergral equation for pair correlation functions in molecular liquids. *Journal of Chemical Physics*, 59:6587, 1973.
- [44] L. J. Lowden and D. Chandler. Theory of intermolecular pair correlations for molecular liquids. applications to the liquids carbon tetrachloride, carbon disulfide, carbon diselenide and benzene. *Journal of Chemical Physics*, 61:5228, 1974.
- [45] K. S. Schweizer and J. G. Curro. Integral-equation theory of the structure of polymer melts. *Physical Review Letters*, 58:246, 1987.
- [46] A. Yethiraj, B. J. Sung, and F. Lado. Integral equation theory for two-dimensional polymer melts. *Journal of Chemical Physics*, 122:94910, 2005.
- [47] J. L. Kirschvink and J. W. Hagadorn. *Biom mineralization*. Wiley-VCH, Weinheim, 2000.
- [48] Mats S.-A. Johnsson and George H. Nancollas. The role of brushite and octacalcium phosphate in apatite formation. *Critical Reviews in Oral Biology and Medicine*, 3:61–82, 1992.
- [49] A. G. Walton, W. J. Bodin, H. Furedi, and A. Schwartz. Nucleation of calcium phosphate from solution. *Canadian Journal of Chemistry*, 45:2695, 1967.

-
- [50] F. C. M. Driessens, M. G. Boltong, E. A. P. de Maeyer, R. Wenz, B. Nies, and J. A. Planell. The ca/p range of nanoapatitic calcium phosphate cements. *Biomaterials*, 23:4011–4017, 2002.
- [51] Jorgen Christoffersen, Margaret R. Christoffersen, Wiktor Kibalczyk, and Flemming A. Andersen. A contribution to the understanding of the formation of calcium phosphates. *Journal of Crystal Growth*, 94:767–777, 1989.
- [52] H. El Briak-BenAbdeslam, C. Mochales, M. Paul Ginebra, J. Nurit, J. A. Planell, and P. Boudeville. Dry mechanochemical synthesis of hydroxyapatites from dicalcium phosphate dihydrate and calcium oxide: a kinetic study. *Journal of Biomedical Materials Research Part A*, 67:927, 2003.
- [53] H. T. Blumenthal, A. I. Lansing, and P. A. Wheeler. Calcification of the media of the human aorta and its relationship to intimal arteriosclerosis, aging and disease. *American Journal of Cardiology*, 20:665–687, 1944.
- [54] P. J. Fitzgerald, T. A. Ports, and P. G. Yock. Contribution of localized calcium deposits to dissection after angioplasty: an observational study using intravascular ultrasound. *Circulation*, 86:64, 1992.
- [55] S. Jono, M. D. McKee, C. E. Murry, A. Shioi, Y. Nishizawa, K. Mori, H. Morii, and C. M. Giachelli. Phosphate regulation of vascular smooth muscle cell calcification. *Circulation Research*, 87:10, 2000.
- [56] M. Matsumoto, S. Saito, and I. Ohmine. Molecular dynamics simulation of the ice nucleation and growth process leading to water freezing. *Nature*, 416:409, 2002.
- [57] Chia-Yi Yang, Wan Y. Shih, and Wei-Heng Shih. Monte carlo simulations of the nucleation and growth process of colloidal particles. *Physical Review E*, 64:021403 1–9, 2001.
- [58] Z. L. Zhu, H. Y. Yu, Q. Zeng, and H. W. Heide. Characterization and biocompatibility of fluoridated biphasic calcium phosphate ceramics. *Applied Surface Science*, 255:552–554, 2008.
- [59] Carl Holt. A core-shell model of calcium phosphate nanoclusters stabilized by beta-casein phosphopeptides, derived from sedimentation equilibrium and saxs/sans measurements. *European Journal of Biochemistry*, 252:73–78, 1998.
- [60] D. Enlow, A. Rawal, M. Kanapathipillai, K. Schmidt-Rohr, S. Mallapragada, C. T. Lo, P. Thiyagarajan, and M. Akinc. Synthesis and characterization of self-assembled block copolymer templated calcium phosphate nanocomposite gels. *Journal of Materials Chemistry*, 17:1570–1578, 2007.

-
- [61] Yanbao Li, Tjandra Wiliana, and Kam C. Tam. Synthesis of amorphous calcium phosphate using various types of cyclodextrins. *Materials Research Bulletin*, 42:820–827, 2007.
- [62] C. Combes and C. Reyes-Gasga. Adsorption of proteins and calcium phosphate materials bioactivity. *Biomaterials*, 23:2817, 2002.
- [63] Alexander Heiss. *Zur molekularen Topologie der Bindung natürlicher und rekombinanter Varianten von Fetuin-A an Hydroxylapatit*. PhD thesis, Fakultät für Mathematik, Informatik und Naturwissenschaften der Rheinisch-Westfälischen Technischen Hochschule Aachen, 2002.
- [64] Alexander Heiss, Alexander DuChesne, Bernd Denecke, Joachim Grützinger, Kazuhiko Yamamoto, Thomas Rnning, and Willi-Jahnen-Dechent. Structural basis of calcification inhibition by ahsg fetuin-a. *The Journal of Biological Chemistry*, 278:13333–13341, 2003.
- [65] J. F. Heremans. *Les globulines sériques du système Gamma. Leur nature et leur pathologie*. Brussels, 1960.
- [66] K. Schmid and W. Bieri. Preparation and properties of the human plasma α_2 -glycoproteins. *Biochimica et Biophysica Acta*, 47:440–453, 1961.
- [67] H. E. Schultze, K. Heide, and H. Haupt. Characterization of a low molecular weight α_2 -mucoid from human serum. *Naturwissenschaften*, 49:15–17, 1962.
- [68] K. O. Pedersen. Fetuin, a new globulin isolated from serum. *Nature*, 154:575–575, 1944.
- [69] E. Olivier, E. Soury, P. Ruminy, A. Husson, F. Parmentier, M. Daveau, and J.P. Salier. Fetuin-b, a second member of the fetuin family in mammals. *Biochemical Journal*, 350:589–597, 2000.
- [70] Thorsten Schinke, Christiane Amendt, Andreas Trindl, Oliver Pischke, Werner Müller-Esterl, and Willi Jahnen-Dechent. The serum protein ahsg inhibits apatite formation in vitro and in mineralizing calvaria cells. *The Journal of Biological Chemistry*, 271:20789–20796, 1996.
- [71] Christoph Binkert, Michael Demetrious, Balram Sukhu, Melanie Szweras, Howard C. Tenenbaum, and James W. Dennis. Regulation of osteogenesis by fetuin. *The Journal of Biological Chemistry*, 274:28514–28520, 1999.

-
- [72] Cori $\frac{1}{2}$ Schi $\frac{1}{2}$ fer, Alexander Heiss, Anke Schwarz, Ralf Westenfeld, Markus Ketteler, Ji $\frac{1}{2}$ rgen Floege, Werner Mi $\frac{1}{2}$ ller-Esterl, Thorsten Schinke, and Willi Jahn-Dechent. The serum protein ahsg is a systemically acting inhibitor of ectopic calcification. *Journal of Clinical Investigation*, 112:357–366, 2003.
- [73] M. J. He. *Polymer Physics*. Fundan University Press, 1988.
- [74] Y. Obata, C. Tosaki, and M. Ikeyama. Bulk properties of syndiotactic 1,2-polybutadiene. i. thermal and viscoelastic properties. *Polymer Journal*, 7:207, 1975.
- [75] T. Sasaki, H. Sunago, and T. Hoshikawa. Multiple melting behavior of syndiotactic 1,2-polybutadiene. *Polymer Engineering and Science*, 43:629, 2003.
- [76] F. Bertini, M. Canetti, and G. Ricci. Crystallization and melting behavior of 1,2-syndiotactic polybutadiene. *Journal of Applied Polymer Science*, 92:1680, 2004.
- [77] J. L. Cai, Y. Han, Z. R. Yuan, R. S. Cheng, Z. L. Wang, and L. S. Jiang. Crystallization behaviors of syndiotactic and atactic 1,2-polybutadiene blends. *Polymer International*, 53:1127, 2004.
- [78] M. Q. Ren, Q. Y. Chen, J. B. Song, H. F. Zhang, X. Sun, and Z. S. Mo. Crystallization kinetics and melting behavior of syndiotactic 1,2-polybutadiene. *Journal of Polymer Science, Part B: Polymer Physics*, 43:553, 2005.
- [79] R. Napolitano, B. Pirozzi, and S. Esposito. Structural studies on syndiotactic 1,2-poly(1,3(butadiene) by x-ray measurements and molecular mechanics calculations. *Macromolecular Chemical Physics*, 207:503, 2006.
- [80] J. E. Mark. *Polymer Data Handbook*. Oxford University, 1999.
- [81] Y. Takeuchi. New themoplastic resin 1,2-polybutadiene: fundamental properties and phot degradable characteristics. *Japan Plastic Age*, 10:12, 1972.
- [82] G. Natta. Syndiotactic polymers. *Makromolekulare Chemie*, 16:213, 1955.
- [83] G. Natta and P. Corradini. The structure of crystalline 1,2-polybutadiene and of other syndyotactic polymers. *Journal of Polymer Science*, 20:251, 1956.
- [84] G. Ricci, M. Battistella, and L. Porri. Chemoselectivity and stereospecificity of chromium(ii) catalysts for 1,3-diene polymerization. *Macromolecules*, 34:5766, 2001.
- [85] Y. Obata, C. Homma, C. Tosaki, and N. Suhiraishi. Bulk properties of syndiotactic 1,2-polybutadiene. ii. mechanical properties of uniaxially and biaxially stretched films in relation to molecular orientation. *Polymer Journal*, 7:217, 1975.

-
- [86] Y. Obata, C. Homma, and C. Tosaki. Bulk properties of syndiotactic 1,2-polybutadiene. iii. melting and crystallization properties. *Polymer Journal*, 7:312, 1975.
- [87] V. Monteil, P. Wehrmann, and S. Mecking. A general route to very small polymer particles with controlled microstructures. *Journal of American Chemical Society*, 127:14568, 2005.
- [88] Jr. P. H. Till. The growth of single crystals of linear polyethylene. *Journal of Polymer Science*, 24(106):301–306, 1957.
- [89] E. W. Fisher. Stufen- und spiralförmiges Kristallwachstum bei Hochpolymeren. *Zeitung für Naturforschung*, 12A:753–754, 1957.
- [90] A. Keller. A note on single crystals in polymers: Evidence for a folded chain configuration. *Philosophical Magazine*, 2:1171–1175, 1957.
- [91] J. D. Hoffman, R. L. Miller, H. Marand, and D. B. Roitman. The relationship of c_∞ to the lateral surface free energy σ : estimation of c_∞ for the melt from rate of crystallization data. *Polymer*, 33:2643, 1992.
- [92] J. D. Hoffman, R. L. Miller, H. Marand, and D. B. Roitman. Relationship between the lateral surface free energy σ and the chain structure of melt-crystallized polymers. *Macromolecules*, 25:2221, 1992.
- [93] J. D. Hoffman and R. L. Miller. Kinetics of crystallization from the melt and chain folding in polyethylene fractions revisited: Theory and experiment. *Polymer*, 38:3151–3212, 1997.
- [94] P. J. Barham and A. Keller. High-strength polyethylene fibres from solution and gel spinning. *Journal of Materials Science*, 20:2281–2302, 1985.
- [95] J. Martinez-Garcia, P. J. Barham, and A. Keller. Studies on polyethylene crystallized at unusually high supercoolings: fold length, habit, growth rate, epitaxy. *Journal of Polymer Science : Polymer Physics Edition*, 22:1085–1096, 1984.
- [96] D. C. Bassett and A. Keller. On the habits of polyethylene crystals. *Philosophical Magazine*, 7:1553–1584, 1962.
- [97] S. J. Organ and A. Keller. Solution crystallization of polyethylene at high temperatures. *Journal of Material Science*, 20:1571–1585, 1985.
- [98] Akihiko Toda. Growth mode and curved lateral habits of polyethylene single crystals. *Faraday Discussions*, 95:129–144, 1993.

-
- [99] G. Ungar, E. G. R. Putra, D. S. M. de Silva M. A. Shcherbina, and A. J. Waddon. The effect of self-poisoning on crystal morphology and growth rates. *Advances in polymer science*, 180:45–87, 2005.
- [100] B. Wunderlich. *Crystal melting*. Macromolecular physics: Academic Press, 1973.
- [101] Joachim Loos and Mingwen Tian. Annealing behaviour of solution grown polyethylene single crystals. *Polymer*, 47:5574–5581, 2006.
- [102] Andrew Keller and Stephen Z. D. Cheng. The role of metastability in polymer phase transition. *Polymer*, 39(19):4461–4487, 1998.
- [103] A. H. Windle. The annealing of solution-crystallized polyethylene mats: an x-ray diffraction study. *Journal of Material Science*, 10:1959–1970, 1975.
- [104] David M. Sadler and Stephen J. Spells. Neutron scattering of annealed solution-grown crystals of polyethylene. *Macromolecules*, 22:3941–3948, 1989.
- [105] Stephen J. Spells and David M. Sadler. Mixed-crystal infrared spectroscopy of annealed solution-grown crystals of polyethylene. *Macromolecules*, 22:3948–3954, 1989.
- [106] S. Rastogi, A. B. Speoelstra, J. G. P. Goosens, and P. J. Lemstra. Chain mobility in polymer systems: On the borderline between solid and melt. 1. lamella doubling during annealing of polyethylene. *Macromolecules*, 30:7880–7889, 1997.
- [107] Mingwen Tian and Joachim Loos. Investigations of morphological changes during annealing of polyethylene single crystals. *Journal of Polymer Science: Part B: Polymer Physics*, 39:763–770, 2001.
- [108] Katharina Landfester, Franca Tiarks, Hans-Peter Hentze, and Markus Antonietti. Polyaddition in miniemulsions: a new route to polymer dispersions. *Macromolecular Chemistry and Physics*, 201:1–5, 2000.
- [109] Donald R. Weyenberg, Donald E. Findlay, J. Jr. Cekada, and Alvin E. Bey. Anionic emulsion polymerization of siloxanes. *Journal of Polymer Science, Polymer Symposia*, 27:27–34, 1969.
- [110] G. Strobl. From the melt via mesomorphic and granular crystalline layers to lamellar crystallites: A major route followed in polymer crystallization? *European Physical Journal E*, 3:165–183, 2000.
- [111] Gerg Strobl. Crystallization and melting of bulk polymers: New observations, conclusions and a thermodynamic scheme. *Progress in Polymer Science*, 31:398–442, 2006.

-
- [112] B. Heck, T. Hugel, M Iijima, E. Sadiku, and G. Strobl. Steps in the transition of an entangled polymer melt to the partially crystalline state. *New Journal of Physics*, 1:17.1–17.29, 1999.
- [113] Paul A. Price and Joo Eun Lim. The inhibition of calcium phosphate precipitation by fetuin is accompanied by the formation of a fetuin-mineral complex. *The Journal of Biological Chemistry*, 278:22144–22152, 2003.
- [114] Diego Pontoni, Joerg Bolze, Nico Dingenouts, Theyencheri Narayanan, and Matthias Ballauff. Crystallization of calcium carbonate observed in-situ by combined saxs/waxs. *Journal of Physical Chemistry B*, 107:5123–5125, 2003.
- [115] Sergey V. Dorozhkin and Matthias Epple. Biological and medical significance of calcium phosphates. *Angewandte Chemie*, 41:3130–3146, 2002.
- [116] Roy E. Wuthier, Gregory S. Rice, James E. B. Wallace Jr., Robert L. Weaver, and Racquel Z. LeGeros. In vitro precipitation of calcium phosphate under intracellular conditions: Formation of brushite from an amorphous precursor in the absence of atp. *Calcified Tissue International*, 37:401–410, 1985.
- [117] R. Boistelle, F. Abbona, and H. E. Lundager Madsen. On the transformation of struvite into newberyite in aqueous system. *Physical Chemistry of Minerals*, 9:216–222, 1983.
- [118] F. Abbona, H. E. Lundager Madsen, and R. Boistelle. The initial phase of calcium and magnesium phosphates precipitated from solutions of high to medium concentrations. *Journal of Crystal Growth*, 74:581–590, 1986.
- [119] J. Zhang, S. Jiang, X. Yuan, and X. Zhang. Studies on crystalline structure of syndiotactic 1,2-polybutadiene. *Acta Polymerica Sinica*, 8:1030, 2010.
- [120] L. Wang, X. Gao, Z. Sun, and J. Feng. Anomalous diffusion of chains in semicrystalline ethylene polymers. *Journal of Chemical Physics*, 130:184709(1)–184709(6), 2009.
- [121] S. Rastogi, Y. Yao, D. R. Lippits, G. W. H. Hi $\frac{1}{2}$ hne, R. Graf, H. W. Spiess, and P. J. Lemstra. Segmental mobility in the non-crystalline regions of semicrystalline polymers and its implications on melting. *Macromolecular Rapid Communication*, 30:826–839, 2009.
- [122] Y.-Q. Xue, T. A. Tervoort, S. Rastogi, and P. J. Lemstra. Welding behavior of semicrystalline polymers. 2. effect of cocrystallization on autoadhesion. *Macromolecules*, 33:7084–7087, 2000.

-
- [123] I. G. Voigt-Martin. A quantitative electron-microscopic study of a linear polyethylene fraction crystallized at different temperatures. *Journal of Polymer Science: Polymer Physics Edition*, 19:1769–1790, 1981.
- [124] P. J. Barham, R. A. Chivers, A. Keller, J. Martinez-Salazar, and S. J. Organ. The supercooling dependence of the initial fold length of polyethylene crystallized from the melt: unification of melt and solution crystallization. *Journal of Materials Science*, 20:1625–1630, 1985.
- [125] B. Wunderlich and G. Czornyj. A study of equilibrium melting of polyethylene. *Macromolecules*, 10:906–913, 1977.
- [126] H. Stabinger and O. Kratky. A new technique for the measurement of the absolute intensity of x-ray small angle scattering. the moving slit method. *Makromolekular Chemie*, 179:1655, 1978.
- [127] Nico Dingenouts and Matthias Ballauff. Structural investigation of latexes by small angle x-ray scattering: Measurement and evaluation of data. *Acta Polymerica*, 49:178–183, 1998.
- [128] P. Bi $\frac{1}{2}$ secke. The high-flux beamline at the esrf. *Review of Scientific Instruments*, 63:438, 1992.
- [129] Peter Boesecke. Reduction of two-dimensional small- and wide angle x-ray scattering data. *Journal of Applied Crystallography*, 40:423–427, 2007.

Publications

- C. N. Rochette; S. Rosenfeldt; A. Heiss; T. Narayanan; M. Ballauff; W. Jahnen-Dechent:
A shielding topology stabilizes the early stage protein-mineral complex of Fetuin-A and calcium-phosphate
ChemBioChem, 10(4), 735-740, 2009.
- C. N. Rochette; S. Rosenfeldt; K. Henzler; F. Polzer; M. Ballauff; Q. Tong; S. Mecking; M. Drechsler; T. Narayanan; L. Harnau:
Annealing of single lamella nanoparticles of polyethylene
Macromolecules, 44(12), 4845-4851, 2011.

Curriculum Vitae

Private:

Name: Christophe Nicolas Rochette
Address: 5 rue de Savoie
33600 Pessac
FRANCE
Marital status: Single

Schools:

1984-1988: Ecole primaire de la Glacière, Mérignac, France
1988-1990: Ecole primaire de Cap de Bos, Pessac, France
1990-1994: Collège Ladonne, Pessac, France
1994-1995: Lycée Pape Clément, Pessac, France
1995-1998: Lycée Sainte Marie Grand Lebrun, Bordeaux, France

Scientific studies:

1998-2000: Institute of Technology, Physical Measurements, Talence, France
2000: Research assistant: "Studies of the pollutant effect of aluminium ions on sunflowers", TAMK, Tampere, Finland - Supervisor: Prof. Dr. Marjukka Dyer
2000-2004: Master of Chemistry, University of Bordeaux 1, Talence, France
2003: Research assistant: "Membrane structure and interactions of antibiotic peptides from Australian tree frogs", School of Chemistry, University of Melbourne, Victoria, Australia - Thesis supervisor: Prof. Dr. Frances Separovic
2004: Research assistant: "Study of the confinement of anionic peptides onto cationic amphiphiles", European Institute of Chemistry and Biology, University of Bordeaux 1, France - Thesis supervisor: Prof. Dr. Reiko Oda

PhD:

Since November 2005: "Structural Analysis of Nanoparticles by Small Angle X-ray Scattering", Bayreuth Center for Colloids and Interface Science, University of Bayreuth, Germany - Thesis supervisor: Prof. Dr. Matthias Ballauff

Erklärung

Hiermit erkläre ich, dass die Arbeit selbständig verfasst und keine anderen als die von mir angegebenen Quellen und Hilfsmittel benutzt habe.

Ferner erkläre ich, dass die anderweitig mit oder ohne Erfolg nicht versucht habe, diese Dissertation einzureichen. Ich habe keine gleichartige Doktorprüfung an einer anderer Hochschule endgültig nicht bestanden.

Bayreuth,

Christophe N. Rochette